UNIVERSITÄT
DES
SAARLANDES

# TWO-PHOTON IMAGING OF THE CORNEA USING FEMTOSECOND LASER MICROSCOPES AND TOMOGRAPHS

DISSERTATION

zur Erlangung des Grades des
Doktors der Ingenieurwissenschaften
der Naturwissenschaftlich-Technischen Fakultät
der Universität des Saarlandes

von

**ANA BATISTA**

Saarbrücken

2018

**Tag des Kolloquiums:** 08/04/2019

**Dekan/in**: Prof. Dr. rer. nat. Guido Kickelbick

**Berichterstatter/in:** Prof. Dr. rer. nat. Karsten König

Prof. Dr. med. Berthold Seitz

**Vorsitzende/r:** Prof. Dr. rer. nat. Helmut Seidel

**Akad. Mitarbeiter/in:** Dr. Christian Spengler

# TABLE OF CONTENTS

# ACKNOWLEDGMENTS

I would like to express my sincere appreciation for the support, motivation, and guidance of my supervisor Prof. Karsten König, without which the completion of this Doctoral research would not have been possible. I would also like to thank all my coworkers at the Department of Biophotonics and Laser technology of Saarland University, particularly Dr. Aisada König and Dr. Hans Georg Breunig, for their assistance, collaboration, advice, and insightful comments. A special thank you also to Andrea Kaiser for her constant assistance and promptness, notably in the transportation of samples, essential for the elaboration of this study.

I am grateful to Prof. Berthold Seitz, Dr. Tobias Hager, and Dr. Elias Flockerzi from the Department of Ophthalmology of Saarland University, who provided me with knowledge and required biological material.

I would also like to thank everyone at JenLab GmbH for providing the necessary equipment for corneal imaging and for aid in the development of the fast Fourier Transform algorithm for image analysis.

I am also thankful to Prof. Miguel Morgado from the University of Coimbra for his support and advice during this Doctoral research.

Finally, I would like to express my gratitude to my family and friends for their continuous and everlasting support throughout my entire life. I am especially grateful to my boyfriend and partner in life Pedro for always being there for me, for pushing me to always excel myself, for giving me strength, for helping, encouraging, and advising me, for everything that you are and everything you do for me.

**Thank you** all · **Vielen Dank** an alle · **Muito obrigado** a todos

# ABSTRACT

The cornea plays a crucial role on visual acuity. Diseases affecting this tissue are the second major cause of blindness worldwide. In clinical practice, it is commonly examined using methods that focus on the morphological analysis while the structural organization of the stroma and the cell's metabolism are disregarded. Two-photon imaging (TPI) can provide these data.

In this study, I demonstrate the advantages of TPI as a new imaging modality for the examination of the cornea. Two systems optimized for corneal imaging were used: a custom-built two-photon laser scanning microscope and a commercial multiphoton tomograph. Both systems were equipped with ultra-short near-infrared Ti:sapphire lasers.

I show that TPI can provide a more complete assessment of the corneal state than the current clinical devices. Moreover, the potential of TPI for the following three clinical applications is shown: 1) it allows a better evaluation of human corneas in cornea banks which could improve sample selection prior to transplantation, 2) it enables the discrimination between non-pathological and diseased corneas based on the combined analysis of the tissue morphology, metabolism, and structural organization, and 3) it provides a faster evaluation of the outcome of corneal collagen crosslinking.

The results indicate that, the multimodal analysis of function and morphology using a novel medical device based on TPI can lead to an improved corneal examination, thus improving diagnosis and care.

# KURZZUSAMMENFASSUNG

Die Cornea spielt für die Sehschärfe eine entscheidende Rolle. Krankheiten, die dieses Gewebe befallen sind weltweit die zweitwichtigste Ursache für Blindheit. In der klinischen Praxis wird die Cornea gewöhnlich nur morphologisch untersucht, wobei strukturelle Zusammensetzung des Stromas und Zellmetabolismus nicht erfasst werden. Diese Informationen liefert die Zweiphotonen-Bildgebung (TPI).

In der vorliegenden Arbeit zeige ich die Vorteile der TPI als neues bildgebendes Verfahren zur Cornea-Untersuchung. Dazu wurden zwei für die Korneabildgebung optimierte Systeme eingesetzt: Ein speziell angefertigtes Zwei-Photonen-Laserscanningmikroskop and ein kommerzieller Multiphotonen-Tomograph. Beide Systeme waren mit ultrakurzen-nahinfraroten Ti:Saphir-Lasern ausgestattet.

Ich zeige, dass TPI eine vollständigere Beurteilung des Corneazustandes ermöglicht als herkömmliche klinische Geräte. Außerdem wird das TPI-Potential für drei klinische Anwendungen dargestellt: TPI ermöglicht 1) eine verbesserte Beurteilung humaner Spender-Corneae, was die Auswahl vor eine Transplantation verbessern könnte, 2) die Unterscheidung von gesunden und pathologischen Corneae basierend auf einer kombinierten Analyse von Morphologie, Metabolismus und strukturellem Aufbau, 3) eine schnellere Beurteilung des Effectes von Kollagen-Crosslinkings.

Die Ergebnisse zeigen, dass eine multimodale Auswertung von Funktion und Morphologie zu einer verbesserten Cornea-Untersuchung und dadurch verbesserter Diagnose und Behandlung führen kann.

# LIST OF FIGURES

# LIST OF TABLES

# LIST OF ABBREVIATIONS

| | |
|---|---|
| **1PE** | One-photon excitation |
| **2D** | Two-dimensional |
| **2PE** | Two-photon excitation |
| **3D** | Three-dimensional |
| **5D** | Five-dimensional |
| **ADC** | Analog-to-digital converter |
| **AF** | Autofluorescence |
| **ACXL** | Accelated corneal collagen crosslinking |
| **AK** | *Acanthamoeba* keratitis |
| **AS-OCT** | Anterior segment optical coherence tomography |
| **ATP** | Adenosine trisphosphate |
| **BL** | Bowman's layer |
| **CFD** | Constant fraction discriminator |
| **CM** | Confocal microscopy |
| **CXL** | Corneal collagen crosslinking |
| **DM** | Descemet's membrane |
| **ECD** | Endothelial cell density |
| **EMC** | Extracellular matrix components |
| **FAD** | Oxidized flavin adenine dinucleotide |
| **FADH2** | Reduced flavin adenine dinucleotide |
| **FD-OCT** | Frequency-domain optical coherence tomography |
| **FFT** | Fast Fourier Transform |
| **Flavins** | FMN and FAD |
| **FLIM** | Fluorescence lifetime imaging |
| **FMN** | Reduced favin mononucleotide |
| **FMNH2** | Oxidized flavin mononucleotide |
| **fs** | Femtosecond |
| **FWHM** | Full width at half maximum |
| **GLCM** | Gray-level co-occurrence matrix |
| **GVD** | Group velocity dispersion |
| **IRF** | Instrument response function |
| **KC** | Keratoconus |
| **LSCM** | Laser scanning confocal microscopy |
| **LTS** | Long-term storage |
| **MTS** | Medium-term storage |
| **NA** | Numerical aperture |
| **NAD(P)H** | NADH and NADPH |

| | |
|---|---|
| **NAD+** | Oxidized nicotinamide adenine dinucleotide |
| **NADH** | Reduced nicotinamide adenine dinucleotide |
| **NADP+** | Oxidized nicotinamide adenine dinucleotide phosphate |
| **NADPH** | Reduced nicotinamide adenine dinucleotide phosphate |
| **NP** | Non-pathological |
| **OCT** | Optical coherence tomography |
| **OMI** | Optical metabolic imaging |
| **PMT** | Photomultiplier tube |
| **PP** | Peak prominence |
| **PSF** | Point spread function |
| **QPM** | Quasi-phase matching |
| **ROI** | Regions of interest |
| **ROS** | Reactive oxygen species |
| **SCS** | Stromal corneal scars |
| **SD** | Standard deviation |
| **SHG** | Second-harmonic generation |
| **SLBM** | Slit-lamp biomicroscope |
| **SM** | Specular microscopy |
| **SNR** | Signal-to-noise ratio |
| **SSCM** | Slit scanning confocal microscopy |
| **STS** | Short-term storage |
| **TAC** | Time-to-amplitude converter |
| **TCSPC** | Time-correlated single photon counting |
| **TD-OCT** | Time-domain optical coherence tomography |
| **THG** | Third-harmonic generation |
| **TPEF** | Two-photon excitation fluorescence |
| **TPI** | Two-photon imaging |
| **TSCM** | Tandem scanning confocal microscopy |
| **UV** | Ultraviolet |
| **UVA** | Ultraviolet A |

# 1 INTRODUCTION

In daily clinical practice, slit-lamp biomicroscopy, confocal microscopy, and anterior segment optical coherence tomography are the corneal imaging methods of choice. These imaging modalities provide important information on the human cornea and have greatly contributed to our understanding of its anatomy and physiology in health and disease. Nevertheless, using these imaging modalities, clinicians are mostly limited to the morphological analysis of the cellular layers. So far, both the structural organization of the stroma and functional analysis of the cornea have been disregarded.

In this study, a novel imaging device for corneal imaging based on two-photon excitation is introduced and its advantages are demonstrated. It makes it possible to obtain information on the cornea that is not accessible with current clinical devices. New applications and protocols are explored to demonstrate the potential for improved assessment of donor corneal buttons, diagnosis of corneal diseases, and follow-up to medical procedures. The data shows that two-photon imaging (TPI) could become a major assess in corneal diagnosis and care.

## 1.1 MOTIVATION AND GOALS

Diseases affecting the human cornea are, according to the World Health Organization, the second major cause of blindness worldwide, with cataracts being the first [1]. The cornea is the first structure of the eye to interact with light. It plays a crucial role in visual acuity as it is the structure that most contributes to light refraction. Disturbances to the cornea can induce visual impairment and eventually lead to blindness. Moreover, due to this tissue high innervation, cornea diseases can cause great discomfort to the patients and

be extremely painful. The most successful and cost-effective way to prevent blindness is by monitoring the cornea and early diagnosing pathologies. Therefore, efficient methods to detect corneal pathologies and stop disease progression in their initial stages are essential.

Over the past decades, the introduction and development of novel imaging modalities, such as confocal microscopy and anterior segment optical coherence tomography, have greatly enhanced our understanding of corneal pathophysiology and improved the ability of clinicians to diagnose and treat corneal diseases. This has led to an overall improvement of patient prognosis. Nevertheless, the mechanisms leading to several corneal diseases are still not fully understood and pathological conditions are often late diagnosed, when treatment options are already limited or they are even misdiagnosed.

In many cases, corneal transplantation is the only way to restore the patients' eyesight. Indeed, the transplant of the cornea is the most common type of transplant worldwide [2, 3]. Although in most developed countries, the supply of donated corneas is satisfactory, worldwide only one donated cornea exists for every seventy needed [2]. The number of donated corneas excluded from transplantation due to tissue unsuitability such as low endothelial cell count, largely contributes to the small number of donor corneas available [4, 5]. Moreover, despite having higher success rates than other organ transplants, the rejection rate of corneal grafts is, according to most studies, still between 5% and 7% [3]. However, higher rejection rates have also been reported [3, 6, 7]. Among the risk factors for corneal graft failure are storage methods and duration [3]. Better methodologies to evaluate and monitor human corneal donor buttons could improve sample selection prior to transplantation and further increase the success rate of corneal transplants. In addition, they could lead to an improvement of corneal storage conditions with the potential to increase the overall number of samples suitable for transplantation.

Overall, patients could also benefit from an improved follow-up to several medical procedures, including corneal collagen crosslinking. The success of this procedure is to the most part evaluated only several weeks post-treatment using visual acuity tests.

The introduction of TPI for clinical imaging of the cornea could provide complementary information on the tissue that would lead to advances on its clinical evaluation. Like

current clinical devices, TPI provides tissue morphological information. Moreover, it also enables the simultaneous assessment of corneal function. The metabolic activity of cells is monitored based on fluorescence lifetime imaging (FLIM). Using second-harmonic generation (SHG), the analysis of the structural organization of collagen in the corneal stroma is also possible.

The benefits of TPI as a diagnostic tool have been largely demonstrated in the field of dermatology. A certificated medical device was first introduced in 2002 for imaging of the human skin *in vivo* [8] and was shown to be an efficient tool to diagnose pathologies like atopic dermatitis [9, 10], skin melanoma [11, 12], and carcinomas [13–15]. In the field of ophthalmology, the application of TPI is still limited to research purposes and no two-photon based clinical device exists. Nevertheless, the advantages of methodologies such as FLIM based on one-photon excitation have already been demonstrated. A clinical one-photon excitation instrument for human retina imaging is currently in use and has already been shown to aid in the differential diagnosis of several retinal pathologies [16–19].

In this work, I demonstrate the potential of TPI as a new clinical tool for corneal assessment. Two systems with TPI capabilities were optimized for corneal imaging and used to explore three of the main clinical applications of this imaging modality (i) the evaluation of donor corneal buttons from eye banks, (ii) the examination and monitoring of human corneas with the potential for diagnosis, and (iii) the follow-up after corneal collagen crosslinking. The results presented here show that TPI provides novel information and can lead to substantial improvements in corneal diagnosis, patient follow-up, and sample monitoring prior to transplantation.

## 1.2 Dissertation outline

The present dissertation is divided into nine chapters. In ***Chapter 1,*** an introduction to the research topic is presented, its importance depicted, and the goals formulated.

***Chapters 2***, ***3***, and ***4*** provide the necessary theoretical background:

***Chapter 2*** – A good understanding of the corneal tissue is essential to interpret our results. Therefore, the corneal anatomy as well as its mechanisms of nourishment and innervation are presented.

***Chapter 3*** – In this chapter, the principle of operation of current clinical devices and the advances in corneal evaluation achieved by each device are discussed. Additionally, their limitations are identified demonstrating the need for additional clinical instruments based on TPI to improve corneal examination.

***Chapter 4*** – A discussion on the theoretical principles of TPI is presented. The typical instrumentation used for TPI and the advantages of this imaging modality over other methodologies is described. Finally, the mechanisms that enable TPI to provide information on the cell's metabolism and on the organization of collagen within the stroma are discussed.

***Chapter 5*** contains a revision of the relevant literature. Efforts made to date to improve corneal analysis using the tissue's endogenous fluorescence and/or the second-harmonic signals of collagen fibers are described. Moreover, the contribution of this doctoral work to this field is discussed.

The material and methods are presented in ***Chapter 6***. I describe the instrumental setups of both imaging systems, the image analysis methods and their validation, as well as the preparation of porcine and human corneal samples.

Obtained results are presented in ***Chapter 7***. I report on:

- The safety of the acquisition parameters of the TPI instruments and their ability to image different endogenous fluorophores (*Section 7.1*).
- The characterization of porcine corneas based on their morphology, metabolism, and structural organization of collagen fibers in the stroma (*Section 7.2*).
- The advantages of TPI for the evaluation of donor corneal tissue prior to transplantation (*Section 7.3*).
- The potential of TPI as a corneal diagnostic tool (*Section 7.4*).
- The advantages of TPI in the evaluation and follow-up of corneal collagen crosslinking (*Section 7.5*).

In ***Chapters 8*** and ***9*** I discuss the results obtained during this doctoral work and draw the final conclusions, respectively. I conclude that TPI can provide a more complete analysis of the cornea than current clinical methodologies. Moreover, I demonstrate the feasibility of this imaging modality to evaluate human corneas prior to transplantation, to examine samples diagnosed with different pathologies, and to assess the outcome of corneal collagen crosslinking much sooner than that achieved using current clinical devices.

# 2 THE CORNEA

The cornea is the outermost structure of the eye (Figure 2.1.1). It is a transparent and avascular tissue contiguous with the conjunctiva and the sclera. Anteriorly, it is enclosed by the tear film and posteriorly by the aqueous humor (Figure ) [20–23]. The cornea is responsible for light transmission and refraction. Its transparency, that results from the tissue regular organization, is mandatory for effective light transmission [20–22]. Due to the cornea overall curvature, thickness, and changes in refractive index, it accounts for approximately 66% (43 to 48 diopters) of the total refractive power of the eye [20–22]. The remaining one-third of light refraction is achieved by the crystalline lens. Thus, a proper corneal function is essential to preserve visual acuity. Being an avascular tissue, the interaction with adjacent layers is important for tissue nourishment and maintenance. By preventing the entrance of foreign organisms into the eye, the cornea also acts as a biodefense system [22]. In this chapter, the anatomy of the porcine and human corneas as well as its nourishment and innervation are discussed.

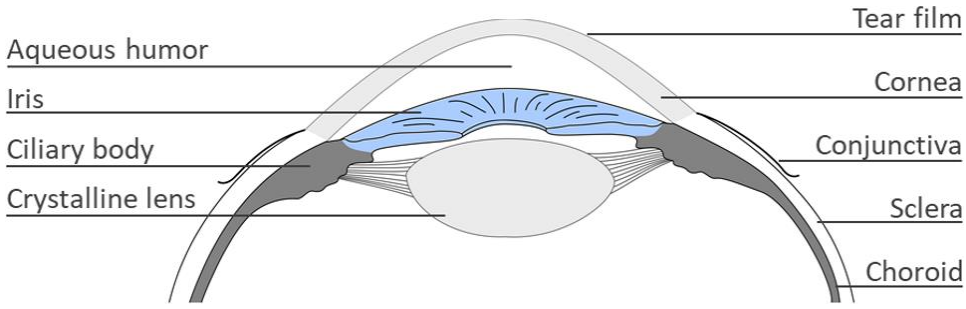


Figure 2.1.1 Sagittal representation of the anterior segment of the eye.

## 2.1 CORNEA ANATOMY

The human cornea is an oval structure measuring 11 to 12 $mm$ and 9 to 11 $mm$ along its horizontal and vertical axes, respectively. Its thickness increases gradually towards the periphery. Values range from 500 $\mu m$ centrally to 700 $\mu m$ peripherally [20, 22]. In pigs, the horizontal and vertical diameters of the cornea are approximately 14 $mm$ and 12 $mm$, respectively [24]. Thicknesses ranging from 660 to 715 $\mu m$ have been reported i*n vivo* [25], whereas *ex vivo* values as high as 1000 $\mu m$ have been measured [24, 26]. Anatomically, the cornea is composed of five main layers (Figure 2.1.2): the epithelium, Bowman's layer (BL), stroma, Descemet's membrane (DM), and endothelium [20, 22]. In pigs, the BL is absent [24]. The characteristics of each layer are discussed in this section.

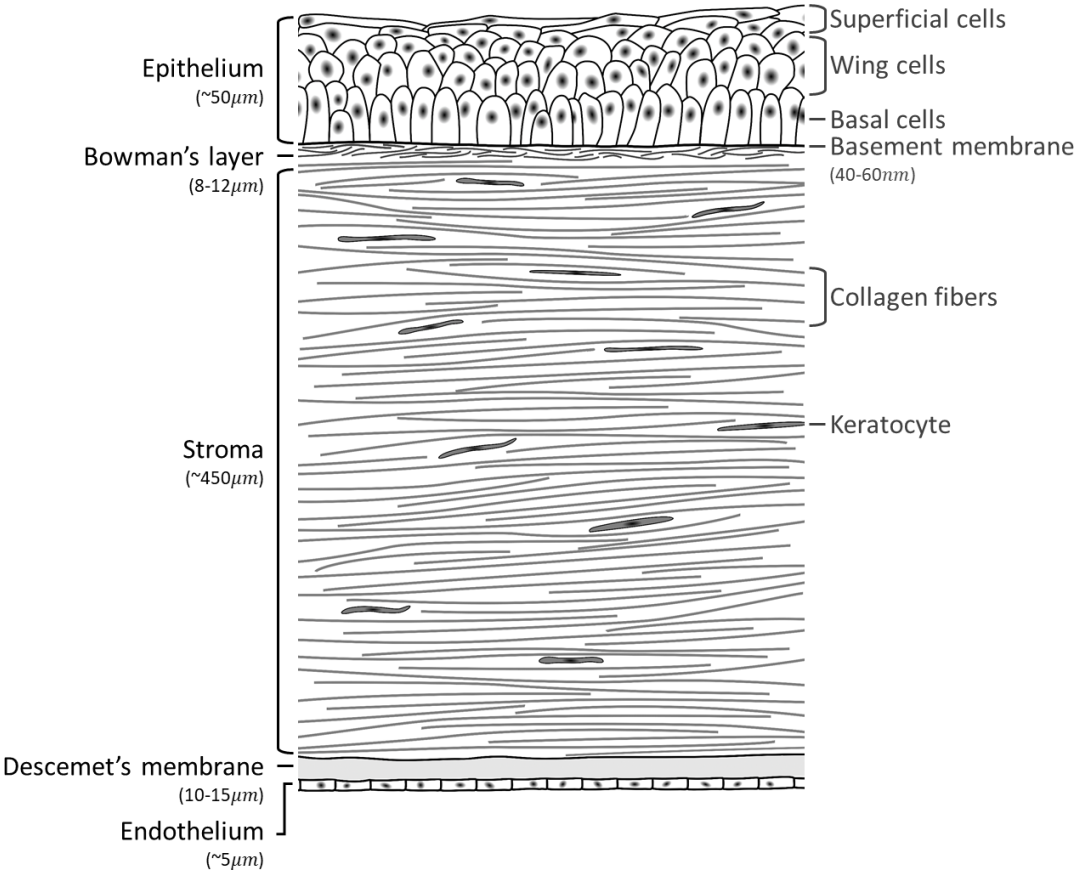


Figure 2.1.2 Cross-sectional representation of the human cornea.

### 2.1.1 Epithelium

The epithelium is the outermost layer of the cornea (Figure 2.1.2). It is contiguous with the conjunctiva epithelium at the limbal region (Figure 2.1.3) and provides protection against external pathogens [22]. The epithelial layer represents about 10% of the total corneal thickness, measuring approximately 50 $\mu m$ in humans [20, 22, 23] and 80 $\mu m$ in pigs [24]. This layer is composed of non-keratinized, stratified squamous cells known to regenerate rapidly [20–23]. According to their level of differentiation, the epithelial cells can be further classified as superficial, wing, and basal cells (Figure 2.1.2) [20, 22].

Superficial cells compose the exterior layers of the epithelium (Figure 2.1.2). These cells are fully differentiated and do not proliferate [20, 22]. With time, they lose their attachments to other cells and are sloughed from the tissue. Simultaneously, new cells move upwards to replace older ones. In this way, an intact epithelial surface is always maintained [20, 22]. Structurally, superficial cells are flat polygons, with flat nuclei and a small number of organelles. At the surface they have numerous protrusions (*microvilli* and *microplicae*) to increase their surface area and create a stable connection with the tear film, a thin (~7 $\mu m$ thick) layer that covers the cornea [20, 22]. A strong and stable connection between superficial cells and tear film is important to maintain a smooth cornea surface and in this way minimize light scattering [20]. To control the uptake of tear film fluid and components, superficial cells are joint laterally by tight junctions. Thus, no substances can penetrate the cornea through the intracellular spaces [20, 22].

The middle layers of the epithelium are composed of cells in an intermediate phase of differentiation – wing cells (Figure 2.1.2) [20, 22]. Structurally, they are polyhedrons shaped like wings. Posteriorly, they are concave to match the shape of basal cells [20]. Small molecules can pass freely between adjacent wing cells due to gap junctions in between them [20, 22].

The last layer of the epithelium is composed of basal cells (Figure 2.1.2). These columnar cells have rounded apical surfaces and are attached, via hemidesmosomes, to the basement membrane (Figure 2.1.2), a 40 to 60 $nm$ thick layer composed of collagen and laminin secreted by the basal cells [20, 22]. Gap junctions in their cellular membranes

promote the passage of small molecules between adjacent cells. These are the only cells in the cornea epithelium with mitotic activity [20, 22]. They differentiate progressively into wing and superficial cells [20, 22]. The complete differentiation process takes from 7 to 14 days [22] which is faster than that of any other epithelial tissue [20] and enables a quickly regeneration after injury [20–23].

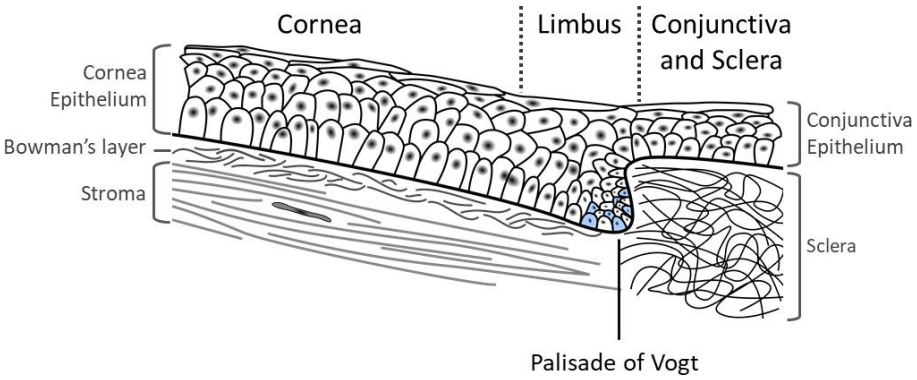


Figure 2.1.3 Cross-sectional representation of the junction between the cornea, conjunctiva, and sclera at the limbus. Stem cells in the palisade of Vogt are shown in blue.

The renewal of basal cells is accomplished by the limbus (Figure 2.1.3). This is a rim around the cornea and consists of a transition zone between the cornea and the conjunctiva/sclera [20, 22, 23]. In the limbus, tissue folds which house and protect stem cells, known as palisades of Vogt, can be found [20, 23]. Stem cell differentiation and centripetal migration are the basis of basal cell replacement and epithelial regeneration [20, 22].

### 2.1.2 Bowman's layer

The BL is an acellular membrane located posteriorly to the epithelium in the human cornea (Figure 2.1.2). This 8 to 12 $\mu m$ thick layer is formed by randomly organized collagen fibers (types I, III, V, and VI) with diameters between 20 and 30 $nm$ [20, 22, 23]. The BL is a highly resistant tissue. However, when injured it does not regenerate. It is normally replaced by epithelial cells or stromal scar tissue [20–22]. Nevertheless, no complications have arisen in patients without it. Thus, the physiological function of this layer is not yet fully determined [20, 22]. The transition between this layer and the stroma

occurs gradually through an increase in the organization of the collagen fibers. A posterior surface cannot be clearly defined [20].

### 2.1.3 Stroma

The stroma is the largest layer of the cornea. It accounts for about 90% of its total thickness [20, 22, 23]. The structural characteristics of this layer largely contribute to the corneal strength, transparency, and shape stability [22]. Anatomically, it is composed of keratocytes, collagen fibers, and other extracellular matrix components (EMC) [20, 22].

Keratocytes occupy 2 to 3% of the stroma total volume (Figure 2.1.4) [20, 22, 23]. These cells are distributed in a corkscrew like pattern, with higher density in the anterior than the posterior stroma [20, 27]. Anatomically, keratocytes are flat cells with widths between 11 and 13 $\mu m$ and lengths between 22 and 30 $\mu m$ [27]. They possess long branching processes which are connected via gap junctions to neighboring cells, forming a continuous network [20, 22]. Keratocytes are responsible for the synthesis of collagen and other EMC [20]. As such, they have important roles in stroma maintenance and wound healing [20, 22]. These cells are usually in a quiescent state. However, in case of injury they are activated and migrate to the affected area where they can produce healing factors, such as enzymes and cytokines [22]. They may also differentiate into myofibroblasts. The latter are more opaque than the former and produce high quantities of disorganized collagen, leading to scar formation and cornea opacification [22].

The major component of the stroma is collagen, mostly type I and in smaller amounts types III, V and VI [22]. Collagen molecules are organized into fibrils which are further organized into highly regular collagen fibers, with uniform diameters between 25 and 35 $nm$ [22]. Collagen fibers are further assembled into collagen lamellae (Figure 2.1.4) [20, 22]. There are between 200 and 300 lamellae in the stroma laying parallel and interweaved to each other (Figure 2.1.4) [20, 22]. At the periphery, where the stroma is contiguous with the sclera (Figure 2.1.3), the collagen lamellae become disorganized and the tissue loses its transparency [22]. The organization of the collagen lamellae also changes with corneal depth. In the anterior one-third of the stroma the collagen lamellae

are between 0.5 and 30 $\mu m$ wide and 0.2 to 1.2 $\mu m$ thick. In the posterior two-thirds of the stroma, the lamellae become thicker (100 to 200 $\mu m$ wide and 1 to 2.5 $\mu m$ thick), less interweaved, and more regular [20].

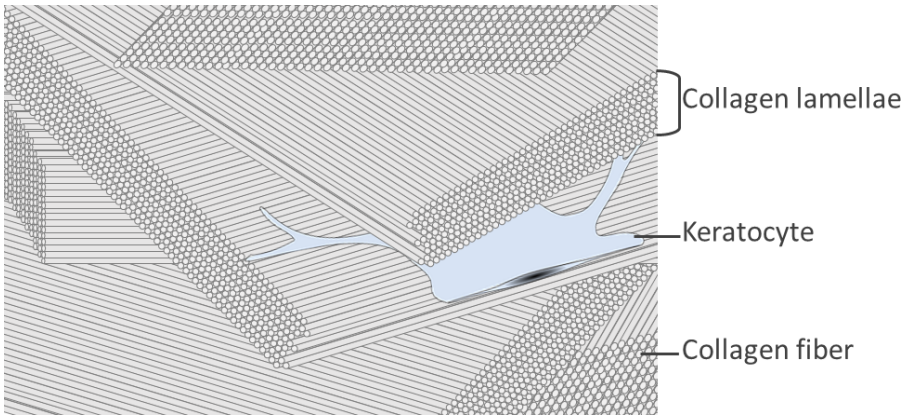


Figure 2.1.4 Representation of the cornea stroma organization. Adapted from [20].

Between collagen fibers, lamellae, and keratocytes lay other EMC, which include hydrophilic and negatively charged molecules [20, 22]. These molecules attract and bind water, thereby maintaining corneal hydration [20]. The water content guaranties the regular spacing between stromal components [20–23].

To maintain corneal transparency, the spacing between collagen fibers and lamellae must be smaller than half the wavelength of visible light [28]. Typically, the distance between adjacent fibers is below 50 $nm$ [22]. This regular arrangement results in destructive interference of scattered light, greatly reducing scattering and increasing transmission [20, 22, 23].

### 2.1.4 Descemet's membrane

The DM is a highly resistant membrane devoid of cellular components and formed mainly by collagen types IV and VIII, laminin, and fibronectin [20–23]. Structurally, it can be divided into two parts [20, 22, 23]. The anterior banded layer (about 3 $\mu m$ thick) is formed during the embryonic development and it may play a role in the adherence and stabilization between the stroma and the DM [20, 23]. The posterior nonbanded layer is formed by deposition of collagen type VIII, secreted by endothelial cells. For this reason, the DM is also considered as the basement membrane of the endothelial cells. The

continuous deposition of collagen throughout life thickens the DM. In adults, DM is about 8 to 10 $\mu m$ thick [20, 22, 23]. The DM in pigs is about 30 $\mu m$ thick [24].

Recently, a pre-DM layer has been proposed – the Dua's layer, which is described as a strong and acellular layer composed of 5 to 8 thin collagen lamellae [29]. However, some controversy surrounding the Dua's layer exists. It has been argued that this structure is still part of the corneal stroma [30].

### 2.1.5 Endothelium

The endothelium is formed by a single layer of polyhedral cells [20, 22, 23]. These are mostly hexagonal and form a mosaic pattern in the posterior surface of the cornea. Structurally, these cells are about 5 $\mu m$ thick and 20 $\mu m$ wide [20, 22]. They are rich in cellular organelles, particularly mitochondria, which reflects their high metabolic activity [20]. Gap junctions in between these cells promote intracellular exchanges [20]. Endothelial cells are responsible for the uptake of nutrients from the adjacent aqueous humor. Along their membranes, they have sodium-potassium pumps and water channels (aquaporins) to regulate the water content in the cornea [20, 22, 23].

Endothelial cells do not regenerate. In case of endothelial cell loss, which is known to occur during aging [20], the remaining cells migrate and expand to fill the empty spaces between them [20–23]. A minimal endothelial cell density is required to cover the posterior surface of the cornea and maintain proper endothelial function (from 400 to 700 $cells/mm^2$) [20].

## 2.2 Corneal nourishment

The human cornea is devoid of blood vessels. Although essential to maintain its transparency, the lack of a vascular system forces the metabolically active cells to find different suppliers of oxygen and nutrients [20, 22]. The interaction with the tear film and the aqueous humor is essential for that. The diffusion of nutrients from the aqueous

humor and the capillary networks in the limbus provides nourishment to the cornea. The oxygenation occurs mainly by diffusion from the air through the tear film, at a rate of 3.5 to 4.0 $\mu l/cm^2$ per hour [22, 23], and in minor amounts from the palpebral conjunctiva vessels [23, 31]. During sleep when the eye lids are closed, the palpebral conjunctiva vessels are the only source of oxygen [23, 31]. Therefore, the concentration of oxygen is highly reduced which leads to a switch from aerobic to anaerobic respiration [22]. Different pathologies may also alter the metabolic activity of corneal cells.

## 2.3 Corneal innervation

The cornea is one of the most highly innervated tissues of the human body. The density of nerves endings in this tissue is about 300 to 400 times higher than in the skin [22]. Based on *in vivo* confocal microscopy images of the human cornea, it has been reported that total number of free nerve endings ranges between 315 000 and 630 000 [32]. Most of these are sensory nerves [32]. Therefore, this tissue is highly sensitive to pain, and even superficial epithelial abrasions can be extremely painful [20, 22]. Besides the sensory nerves, this tissue also comprises of sympathetic nerves, which regulate the metabolism and proliferation of epithelial cells and promote wound healing [20].

The nerve bundles, originating mainly from the ophthalmic branch of the trigeminal nerve, enter the cornea radially and peripherally through the mid-stroma [20, 22, 32]. Within the stroma, and after a short distance (1 to 3 $mm$), the nerves lose their myelin sheaths, a feature essential for corneal transparency [20, 32]. The nerve bundles then change direction and move towards the surface. After penetrating the BL, they branch out and form a nerve network parallel to the corneal surface immediately beneath the epithelial layer (subbasal nerve plexus) [20, 32]. As the nerves pass the BL, the Schwann cells sheath is lost [20]. From the subbasal nerve plexus the nerves move upwards within the epithelial layer where they terminate as free nerve endings [20, 32]. The corneal endothelium and DM are devoid of nerve endings [20].

# 3 Current Devices used for Corneal Monitoring and Diagnosis

The introduction and continuous improvement of corneal imaging methodologies has greatly improved and continues to improve our knowledge about this tissue. They enhance our understanding of the healthy cornea, our ability to diagnose corneal diseases and other anomalies, and help us learn the mechanisms of different pathologies. As such, the probability of a positive prognosis for corneal-diseases is now exceedingly higher than ever before. In this chapter, the major imaging techniques used in clinical practice are described.

## 3.1 Slit-lamp biomicroscopy

The first microscope specifically designed to image the human eye *in vivo* was the slit-lamp biomicroscope (SLBM; Figure 3.1.1A). It was developed in 1911 by Allvar Gullstrand [33–36], who was later awarded the Noble Prize in Physiology and Medicine. The ability to visualize the human eye greatly improved our knowledge about this organ [33]. Even today, due to its versatility, SLBMs are still one of the most widely used instruments in ophthalmological clinics [35, 36].

The SLBM consists of an adjustable binocular microscope and an illumination source. These are mounted on a specially designed stage to allow movement of the microscope and positioning of the patient [33, 34]. The light source intensity, height, width, angle, and color can be changed for better visualizations of different eye structures [34, 36]. Different illumination techniques can also be used to detect different eye anomalies [33]. The light reflected from the sample can be split using dichroic mirrors to enable the collection of

image and/or video signals [33, 35]. The attachment of other accessories to, for instance, measure the intraocular eye pressure is also possible [34, 35].

In clinics, SLBMs are mainly used to image the anterior segment of the eye, which includes the cornea, conjunctiva, sclera, iris, and eyelids. Typical slit-lamp biomicroscopy images of the healthy eye acquired with the SLBM BD-900 (Haag-Streit AG, Koeniz, Switzerland) using white light illumination are shown in Figure 3.1.1B. The SLBM provides a general overview of the eye's health and can be used to diagnose pathologies, such as conjunctivitis, cornea vascularization, or scar formation [35, 36]. The main drawback of slit-lamp biomicroscopy is its limited resolution [34, 35].

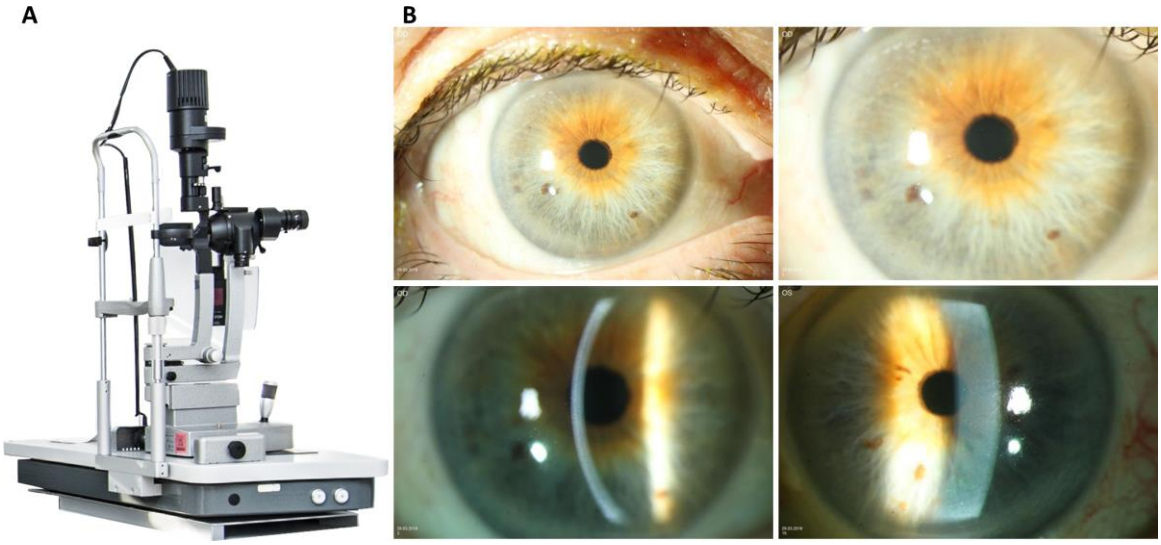


Figure 3.1.1 Slit-lamp biomicroscope BD-900 (Haag-Streit AG, Koeniz, Switzerland) (A) and typical slit-lamp biomicroscopy images of the healthy eye obtained using white light illumination (B). Images courtesy of the Department of Ophthalmology, Saarland University, Medical Center, Homburg/Saar, Germany.

## 3.2 Specular Microscopy

In 1968, David Maurice introduced specular microscopy (SM) [37]. SM is an epi-illumination imaging modality, where specular reflected photons, *i.e.,* photons reflected with the same angle as the incident light are used to create an image (Figure 3.2.1). In SM, the cornea is illuminated using visible light through a slit. The specular reflected photons are then collected by the objective to produce an image at the focal plane (Figure 3.2.1). As the light travels through the tissue, with every change in refractive index, a part of the

light is reflected and collected to form the image. The signal intensity is intrinsically correlated with the difference in refractive index between two interfaces [38, 39]. As such, the final image is a composite between the different refractive index interfaces that occur at different depths.

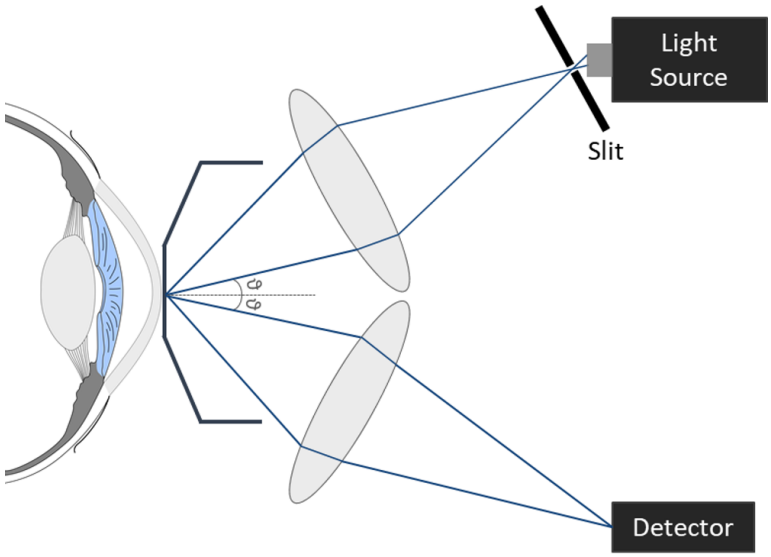


Figure 3.2.1 Schematic representation of the optical setup of specular microscopy.

Four major zones have been described in corneal SM images [38]. They result from light reflection at the four interfaces between objective lens (combined with the coupling fluid), epithelium, stroma, endothelium, and aqueous humor [38, 39]. Wide illumination slits can be used to have large field-of-views of each zone. However, that also results in an increased overlap between consecutive zones and an overall decrease in image resolution. Therefore, narrower illumination slits are usually preferred [38, 39].

The change in refractive index of most interest for corneal SM occurs at the interface cornea/aqueous humor, where it drops from 1.376 to 1.336. This generates a reflection of about 0.02% of the light irradiance and the formation of an image of the endothelial cell layer [38]. Typical images of the corneal endothelial layer obtained using the SM Tomey EM-3000 (Tomey GmbH, Nuernberg, Germany) are shown in Figure 3.2.2.

Over the years, several modifications have been performed to the original concept of the specular microscope such as the coupling of a camera to record the endothelial cells *in vivo*, the increase of magnification, the improvement of the contact interface, the

development of non-contact based systems, and the introduction of software for semiautomatic or even automatic calculation of endothelial cell densities (ECDs) [39–43].

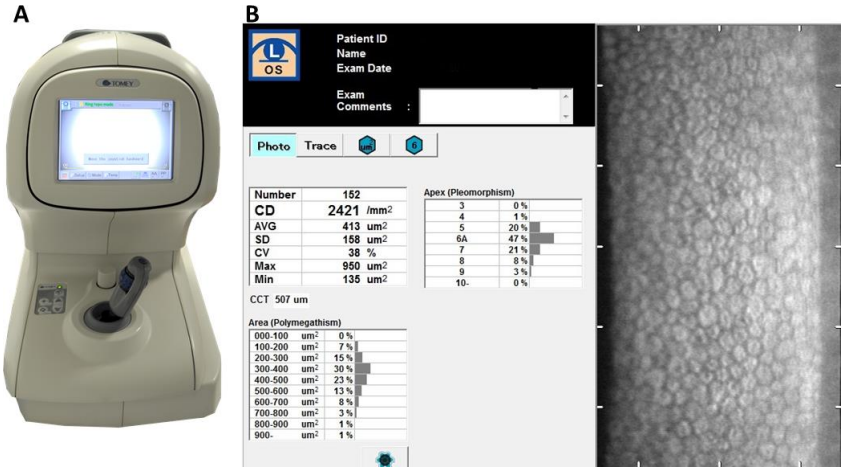


Figure 3.2.2 Specular microscope SM-3000 (Tomey GmbH, Nuernberg, Germany) (A) and images of the healthy corneal endothelium covering an area of 250 × 540 $\mu m^2$ obtained using this instrument (B). Images courtesy of the Department of Ophthalmology, Saarland University, Medical Center, Homburg/Saar, Germany.

Nowadays, SM is used in clinical practice to image and record noninvasively the corneal endothelial layer. It is used to monitor changes to the density of endothelial cells with age, to evaluate donor corneas in the cornea banks, and in the diagnosis of pathologies where the endothelial layer is greatly affected such as Fuchs' dystrophy [39].

## 3.3 Confocal Microscopy

Confocal microscopy (CM) was first described by Marvin Minsky in 1955 [44]. Minsky's concept was based on targeting the illumination and detection of backscattered signals on a single focal point. This was accomplished by pinholes in the illumination and detection pathways (Figure 3.3.1) [44–47]. By blocking the out-of-focus light, axial resolution is greatly improved when compared to conventional light microscopes. Furthermore, it enables imaging samples at multiple depths [45, 46].

Only the signal from a single point of the specimen is detected at a given time. Thus, a scanning method is required to create an image. In Minsky's original design, the tissue was scanned by moving the microscope stage [44]. Thus, image acquisition was slow. In

1968, the first tandem scanning confocal microscope (TSCM) was developed [48]. In TSCMs, the illumination and imaging of the sample is performed through modified rotating Nipkow disks. These disks contain several pinholes, with diameters around 20 $\mu m$, organized in Archimedean spirals. As such, signals from multiple focal points are collected simultaneously reducing image acquisition time [45, 48]. Typically, TSCMs employ 24x objectives with numerical aperture (NA) of 0.6 which confers them an axial resolution of about 9 $\mu m$. Laterally, its resolution is between 0.5 and 1 $\mu m$ [45, 49, 50]. One of the drawbacks of these devices is the low transmittance of the light achieved through the Nipkow disks (between 0.25 and 1%) which hinders the feasibility to image structures with low contrast [49]. Nowadays, commercial TSCMs systems are no longer manufactured [50].

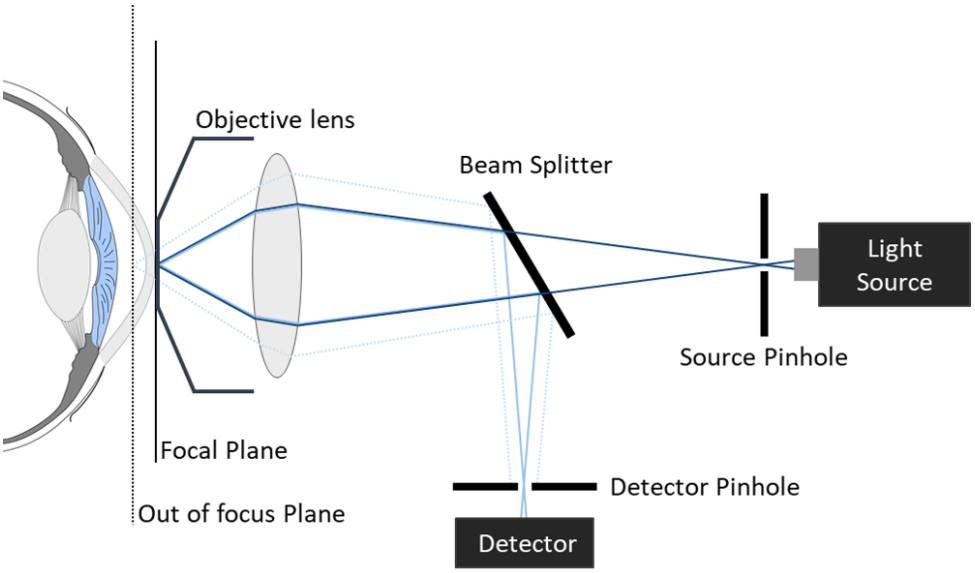


Figure 3.3.1 Schematic representation of the optical setup of confocal microscopy.

Current commercially available confocal microscopes use one of two main scanning methods: slit scanning and laser beam scanning [51]. The slit scanning confocal microscope (SSCM) was introduced in 1994 by Masters and Thaer [52]. With this method, the tissue is illuminated and imaged using oscillating double-sided mirrors. The reflected light is then collected by a CCD camera. The thickness of the optical section can be changed by modifying the size of the slits [46, 52]. SSCM has several advantages over TSCM, such as the possibility of longer exposition times, the detection of structures with low reflection like wing cells, and a higher signal-to-noise ratio (SNR) [45, 46]. However,

due to the use of slits rather than pinholes, SSCM has a much lower axial resolution than a TSCM (up to 27 $\mu m$) [45, 49–51].

In laser scanning confocal microscopes (LSCMs) such as the Heidelberg Retinal Tomograph 3 with Rostock Cornea Module (HRT3-RCM, Heidelberg Engineering GmbH, Heidelberg, Germany) shown in Figure 3.3.2A, a 670 $nm$ laser is used to raster scan the field-of-view using scanning mirrors [45, 47]. The photons reflected from the sample are detected in a descanned geometry using a photodetector [45, 47]. This system employs a 63x 0.95 NA water immersion objective and image acquisition rates can vary between 1 and 30 frames per second [51]. Images acquired using the HRT3-RCM have high SNR and high resolution due to the high NA objective lens. The system's resolution is ~1 $\mu m$ laterally and ~4 $\mu m$ axially [45, 50, 51].

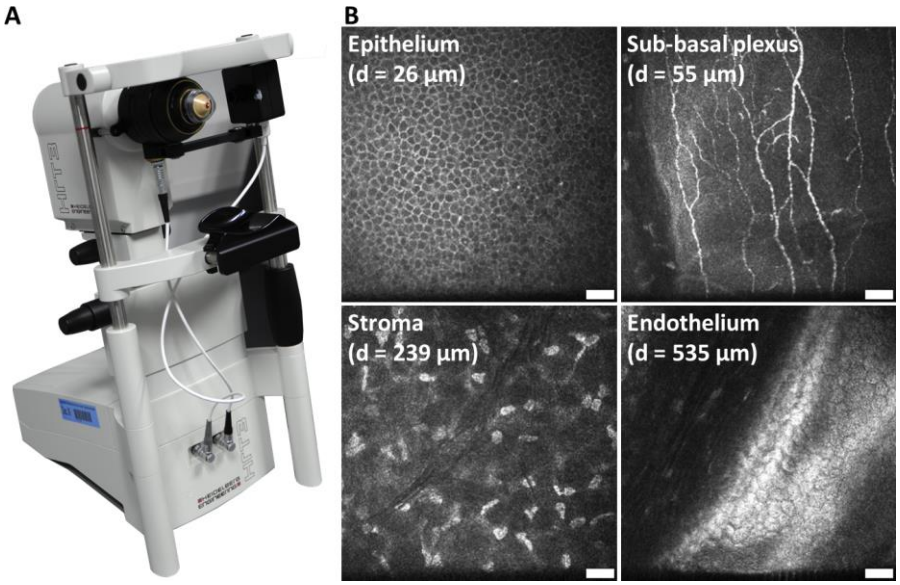


Figure 3.3.2 Heidelberg Retinal Tomograph 3 with Rostock Cornea Module (HRT3-RCM, Heidelberg Engineering GmbH, Heidelberg, Germany) (A) and confocal microscopy images of different layers of the healthy human cornea (B). Scale bars = 30 $\mu m$. Images courtesy of the Department of Ophthalmology, Saarland University, Medical Center, Homburg/Saar, Germany.

CM was introduced to ophthalmology in 1986 with the imaging of the human cornea *ex vivo* [53] and the retina *in vivo* [54] using TSCMs. The first *in vivo* imaging of the human cornea was performed in 1990 [55]. From then on, the usage of CM in clinical practice has highly increased over the years due to its ability to discriminate between all corneal layers [45]. CM allows the discrimination of different cell types in the epithelium, the detection of corneal nerves in the subbasal nerve plexus, the evaluation of keratocytes in the stroma, and the analysis of the corneal endothelium (Figure 3.3.2). As such, CM has

become an important instrument for the diagnosis of different pathologies as well as for tissue monitoring pre- and post-surgery [45, 47, 56]. Nevertheless, CM still has some limitations. It only provides morphological information and cannot image stromal collagen.

## 3.4 Anterior segment optical coherence tomography

The anterior segment optical coherence tomography (AS-OCT) is one of the most recent modalities introduced to image the human cornea [57]. AS-OCT is a modified version of the optical coherence tomography (OCT) developed by Huang, Fujimoto, and colleagues in 1991 [58–60].

OCT is a non-contact imaging modality based on interferometry to measure the delay of reflected light. The illumination light is split into two beams using a beam splitter: the sample and the reference beams. After recombination, their interference pattern is descanned and detected using a photodetector to generate an axial scan (A-scan) of the tissue (Figure 3.4.1). A transverse scan of the tissue using scanning mirrors is required to obtain cross-sectional (B-scan) and three-dimensional images [60].

OCT can be divided into two main types: time- and frequency-domain. Time-domain OCT (TD-OCT) was the original OCT design. In TD-OCT, the acquisition of A-scans is accomplished by axially moving the reference mirror to match the delay of different depths within the sample [60]. In frequency-domain OCT (FD-OCT), the reference mirror is kept fixed and the interference signals from all layers of the sample are collected simultaneously using a spectral detector (Figure 3.4.1). A Fourier transform is then applied to generate the A-scans. With the introduction of FD-OCT, both acquisition time and SNR were improved [60].

The feasibility of OCT imaging of the human retina was demonstrated *in vivo* for the first time in 1993 [61]. One year later, Joseph Izatt attempted to image the anterior segment of the eye [62]. However, the OCT specifications, namely, the laser excitation wavelength, were not optimal for corneal imaging [63]. In 2001, the first measurements of the human

cornea by OCT were achieved, using a system specifically designed to image the anterior segment of the eye (AS-OCT) [57]. This system had faster scanning times, longer wavelength laser sources (1310 $nm$), and scanning protocols optimized for the corneal curvature [57]. These modifications yielded less image distortions. Moreover, excitation at 1310 $nm$ reduced the scattering in opaque tissues, enhanced light penetration depths and made imaging of the sclera and limbus possible [63, 64]. However, it hindered its optical resolution. Commercially available devices with an excitation wavelength of 1310 $nm$ yield images with axial resolutions between 10 and 25 $\mu m$ whereas in devices with lower excitation wavelengths, the axial resolution is between 3 and 5 $\mu m$ [60].

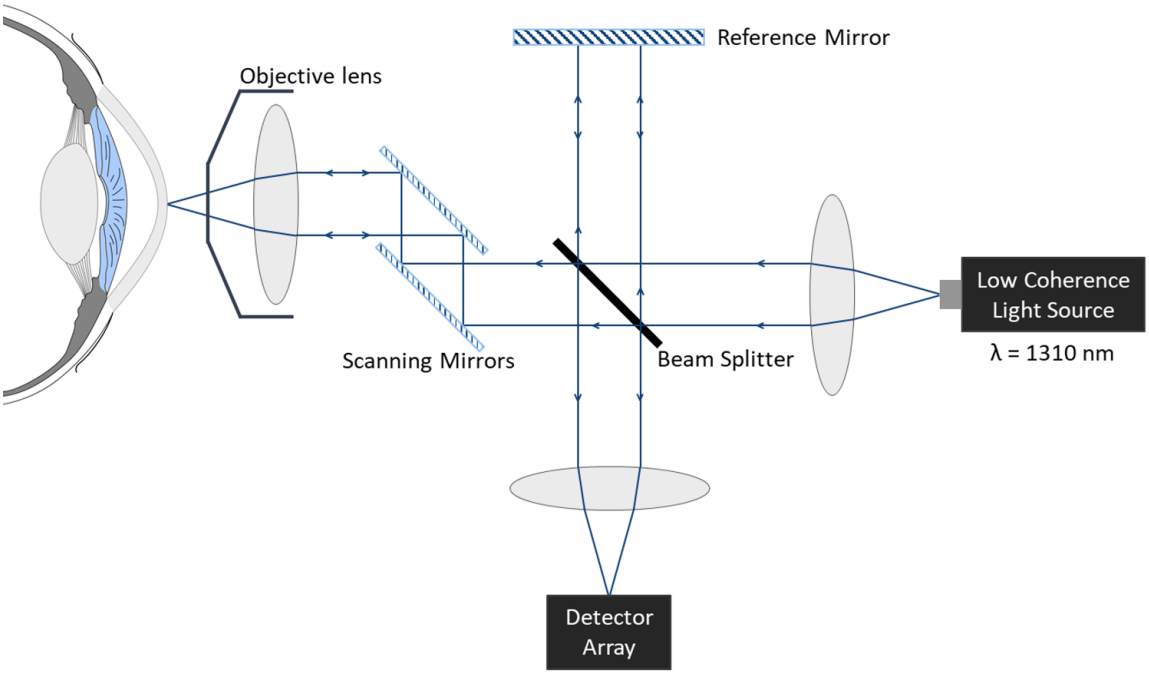


Figure 3.4.1 Schematic representation of the optical setup of frequency-domain anterior segment optical coherence tomography.

Figure 3.4.2 shows typical OCT images of the healthy cornea acquired using the OCT system CASIA 2 (Tomey GmbH, Nuernberg, Germany). This commercial FD-OCT system employs a 1310 $nm$ excitation source, has a scanning rate of 50 000 A-scans per second, and axial and transverse resolutions of 10 $\mu m$ and 30 $\mu m$, respectively.

In clinical practice, OCT is widely used for the evaluation of the retina. Its applications for corneal imaging are less extensive. AS-OCT provides clinicians with information on the corneal thickness and allows corneal layer discrimination (Figure 3.4.2) [63]. This is usually used to monitor patients after corneal surgery (including corneal transplants) [60, 64] and

it may be used to diagnose closed angle glaucoma, keratoconus, and corneal opacities [60, 63, 64]. Recently, AS-OCT was introduced to assess the clinical outcome of corneal collagen crosslinking [65–67]. The major drawback of these systems is their low transverse resolution. Typically, AS-OCT images acquired using commercial systems have transverse resolutions on the order of several tens of micrometers [68, 69]. Cross-sectional views of the cornea can also be obtained using high-frequency ultrasound. However, ultrasound images have a lower resolution than AS-OCT images (20 – 100 $\mu m$) [70].

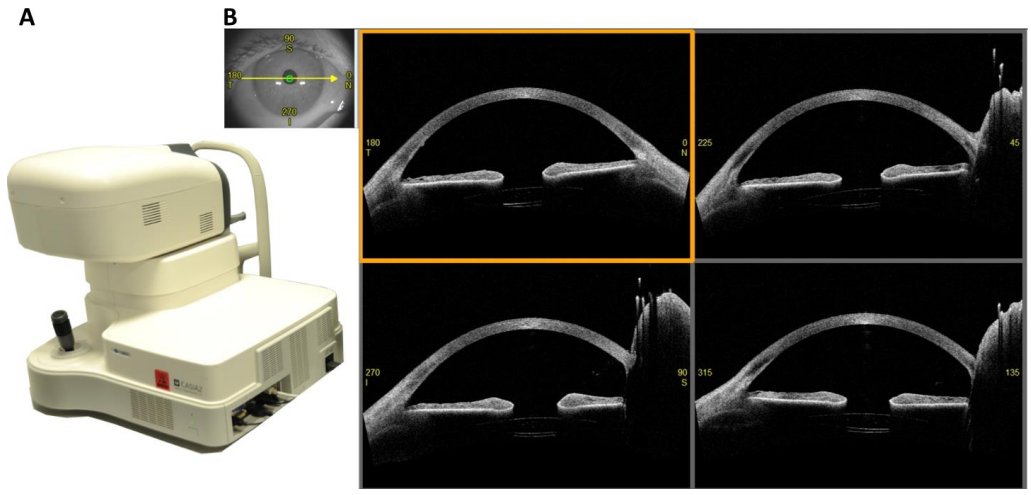


Figure 3.4.2 Anterior segment optical coherence tomograph CASIA 2 (Tomey GmbH, Nuernberg, Germany) (A) and images of the healthy human cornea recorded using this system (B). Images courtesy of the Department of Ophthalmology, Saarland University, Medical Center, Homburg/Saar, Germany.

## 3.5 Other diagnostic techniques

Complementary procedures such as corneal topographic, pachymetric and aesthesiometric measurements, and corneal staining are commonly used in clinical practice to aid the diagnosis of corneal pathologies.

Corneal topography gives clinician information on the corneal shape. Typically, a topographic map of the corneal surface is generated from the reflection of the corneal surface to a circular mire pattern known as the Placido disk [71]. It is commonly used to assess cornea irregular astigmatism and surface alterations in keratoconus [71].

Pachymetry is the measurement of corneal thickness. Since the thickness of the cornea can be influenced by several pathologies, pachymetric measurements are commonly used

in clinical practice and are highly important. They can be used to evaluate cornea thinning due to keratoconus and swelling due to loss of integrity of endothelial cell. Cornea thinning has also been described a risk factor for glaucoma development [72]. Both optical and ultrasound methods can be used to measure the thickness of the cornea [72]. Optical methods are based on techniques such as CM or AS-OCT. Ultrasound methods measure the time delay between the sound wave emission and its detection after reflection at the DM. The sound speed in the cornea is considered to be 1640 $m/s$ [73]. Ultrasound pachymeters are usually preferred in clinical practice as they are accessible, easy to use, fast, and precise. Using these devices, the corneal thickness may be obtained with an accuracy of about 5 $\mu m$ [72]. Nevertheless, these devices require the application of topical anesthesia, which can be avoided using non-contact methods such as AS-OCT [72].

Aesthesiometric measurements are performed to assess corneal sensitivity, which may be affected due to surgery, infection, or inflammation [72]. Corneal staining is typically used to assess the integrity of the tear film and epithelial cells [72]. Degeneration of the tear film and epithelial cell death increases the permeability of the cornea to external dyes. Fluorescein and rose Bengalis are the most commonly used dyes in corneal disease diagnosis. Along with the permeability to the dye, the location and pattern created by the dye stain within the cornea can also aid the diagnosis and the selection of treatment [72].

# 4 TWO-PHOTON IMAGING

Current clinical devices provide complementary and valuable information on the human cornea and have greatly improved our ability to monitor and diagnose corneal pathologies. Although, they can provide clinicians with information on corneal morphology, the status of the cell's metabolic activity is lacking. Furthermore, stroma analysis is limited to layer thickness and to morphology and density of keratocytes. No information is available on the structural arrangement of collagen fibers or keratocyte's metabolism.

A novel clinical two-photon imaging (TPI) device can provide information on intratissue and intracellular morphology and on cell's metabolism based on two-photon excitation fluorescence (TPEF) combined with fluorescence lifetime imaging (FLIM). Moreover, second-harmonic generation (SHG) signals from collagen can provide information on the stromal structural organization.

TPI allows to combine both structural and functional analysis. Therefore, it can overcome some of the limitations of current clinical methods. TPI can improve corneal-disease diagnosis, enhance our knowledge regarding mechanisms of disease progression, improve patient follow-up after medical procedures, and provide sample evaluation during storage.

This chapter presents the basic principles of TPEF, FLIM, and SHG. The advantages of TPI for tissue imaging and the mechanisms by which it can be used to assess the metabolism of corneal cells and the orientation of stroma collagen fibers based on endogenous sources of contrast are explored.

## 4.1 PRINCIPLES OF TWO-PHOTON IMAGING

Over the past years, the relevance of TPI in both biological and medical fields has highly increased. The basis of this imaging modality is the nearly simultaneous, nonlinear interaction of two photons with a given molecule. When this interaction occurs, the photons can be absorbed, leading to molecular excitation with subsequent relaxation via fluorescence emission (TPEF). Additionally, a polarization of the second-order in the electric field can be induced leading to SHG. Since TPEF and SHG rely on two distinct contrast mechanisms while using the same laser source, these imaging modalities can be easily combined into one single system to provide complementary information.

### 4.1.1 Fluorescence emission

Fluorescence is one of the processes by which molecules can relax from an excited electronic state ($S_1$) to the ground state ($S_0$) after excitation and is characterized by the spontaneous emission of photons (Figure 4.1.1). At room temperature, most molecules are in the ground state ($S_0$), since the corresponding thermal energy is not enough to populate excited electronic states. Therefore, the absorption of energy in the form of photons is necessary for fluorescence emission [74]. The absorbed energy ($E$) given by

$$E = h\nu \qquad (4.1)$$

where $h$ is the Planck's constant and $\nu$ is the frequency of the light, must be at least equal to the energy difference between the ground state and an excited electronic state ($E_{min}$) to induce molecular excitation (Figure 4.1.1). This can be accomplished through the absorption of a single photon with energy $E_1 \geq E_{min}$. This process is commonly referred to as one-photon excitation (1PE). Alternatively, two photons, in which the combined energy is at least equal to $E_{min}$, can be absorbed within very brief time gap (Figure 4.1.1) [75, 76].

The theoretical principle of two-photon excitation (2PE) was initially proposed by Maria Göppert-Mayer in 1931 [75]. However, it could not be confirmed at the time it was

formulated due to the inexistence of light sources with the necessary power density. Only 30 years later, after the introduction of lasers [77] it was possible to demonstrate two-photon molecular excitation. In 1961, Kaiser and Garrett showed for the first time two-photon excited fluorescence of $CaF_2$:$Eu^{2+}$ [78]. The first fluorescence microscope for imaging of biological samples based on 2PE was introduced in 1990 by Denk, Strickler, and Webb [79].

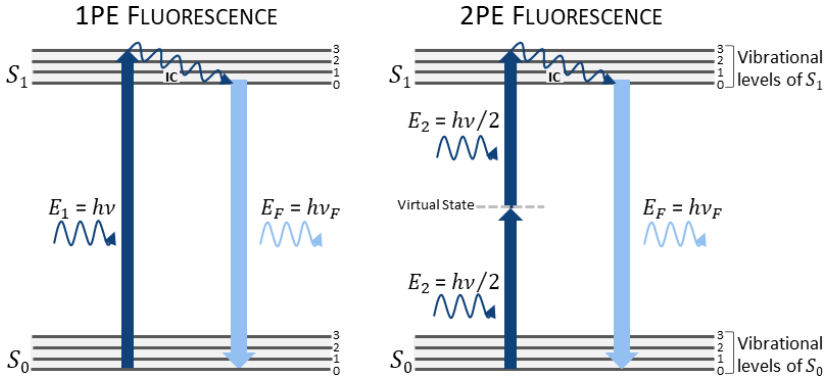


Figure 4.1.1 Jablonski diagrams of one-photon excitation (1PE) and two-photon excitation (2PE) fluorescence. In 1PE and 2PE, the absorption by the molecule of one photon or two photons, respectively, promotes its transition to a higher energy state ($S_1$). Following either excitation process, the molecule undergoes internal conversion (IC) followed by relaxation to the lowest energy level ($S_0$) by emitting a photon. $E$ – energy; $h$ – Planck's constant; $\nu$ – frequency.

Following excitation, the molecules rapidly undergo internal conversion, *i.e.* they relax to the ground vibrational level of the first electronic state ($S_1$). This process takes about 1 $ps$ [74, 76]. After internal conversion, the molecules relax to the ground state via the emission of photons (fluorescence) or via a competing nonradiative relaxation pathway. The probability of a molecule to relax to the ground state by emitting fluorescence is commonly referred to as the molecule's quantum yield. It can be computed as the ratio between the emitted and absorbed photons and it is independent of the excitation process (1PE or 2PE) [74, 76, 80].

Fluorescence emission of a given molecule is dependent on its efficiency to absorb light. This is given by its absorption cross-section and/or its molar attenuation coefficient which are dependent on the excitation wavelength. Since 2PE relies on longer excitation wavelengths for molecular excitation than 1PE, the absorption cross-section of a given molecule is dependent on the excitation type [80]. Nevertheless, for several molecules

the 2PE spectra of light absorption are similar to the 1PE absorption spectra with wavelengths doubled [74].

The absorption of light by the tissue may be computed using the Beer-Lambert law [74, 76]. As lights propagates through an absorbing medium it is attenuated. The intensity of light after propagation through a medium with thickness $l$, is dependent on the intensity of the incident light ($I_0$), the number of light-absorbing molecules, $n$, and on the molecular absorption cross-section ( $\delta$ ), as a function of the wavelength ( $\lambda$ ) [76, 81, 82]:

$$I = I_o e^{-\delta(\lambda) n l} \qquad (4.2)$$

Alternatively, light absorption by the medium may also be computed as a function of the molar attenuation coefficient, $\varepsilon(\lambda)$:

$$I = I_o e^{-\varepsilon(\lambda) m l} \qquad (4.3)$$

where $m$ is the molar concentration [74, 76, 81, 82]. From both equations, the relation between the molar attenuation coefficient and the molecular cross-section can be obtained and is of the order of $\delta(\lambda) \approx 3.825^{-21} \varepsilon(\lambda)$ [74, 76].

The fluorescence of a molecule can be characterized by its emission spectra and its lifetime. The molecule's emission spectrum provides information on the amount of emitted light as a function of the wavelength. Due to the nonradiant relaxation process of internal conversion, the energy of the emitted photons is lower than the total energy absorbed [74]. The fluorescence lifetime is the average time that a fluorophore spends in the excited state following excitation and it is obtained from the inverse of the sum of all relaxation pathways [74]. For the majority of fluorophores, both emission spectra and lifetimes are equal for 1PE and 2PE [74, 80, 83].

## Advantages of two-photon excitation for imaging

In fluorescence imaging, the use of 2PE for molecular excitation of fluorescent molecules has several advantages over 1PE. Due to longer excitation wavelengths, 1PE light absorption and scattering are reduced which leads to deeper tissue penetration [74, 79, 84]. Additionally, with 2PE, photobleaching and photodamage are confined to the focal

volume and therefore reduced when compared with 1PE [79, 80, 84]. Another advantage of 2PE is its inherent three-dimensional (3D) optical sectioning due to the nonlinear dependence on the excitation intensity. The rate of molecular excitation is, in the case of 1PE, linearly proportional to the intensity of the incident light. In contrast, 2PE has a quadratic dependence on the excitation intensity [74, 80, 84].

The light intensity distribution at the focal point of an objective with numerical aperture $NA = n \sin \alpha$ is given by:

$$I(u, \sigma) = \left| 2 \int^{1} J_0(\sigma\rho) e^{-\frac{i}{2}u\rho^2} \rho \, d\rho \right|^2 \qquad (4.4)$$

where $J_0$ is the 0$^{th}$-order Bessel function, $\rho$ is the radial coordinate in the pupil plane, and $u$ and $\sigma$ are the dimensionless axial and radial coordinates normalized to the wavelength $\lambda$ as:

$$u = \frac{8\pi}{\lambda} sin^2\left(\frac{\alpha}{2}\right) z \qquad (4.5)$$

$$\sigma = \frac{2\pi}{\lambda} \sin(\alpha)\, r = \frac{2\pi}{\lambda} \sin(\alpha) \sqrt{x^2 + y^2} \qquad (4.6)$$

In the case of 1PE, the point spread function (PSF) has a $I(u, \sigma)$ profile, whereas for 2PE the PSF is given by $I^2(u/2\,, \sigma/2)$. The axial PSFs for 1PE and 2PE are shown in Figure 4.1.2. As shown in the figure, the 2PE PSF is axially confined. Therefore, the excitation occurs only inside the limited focal volume where the photon density is highest, giving inherent optical sectioning to this imaging modality [74, 80, 84, 85]. In contrast, the axial 1PE PSF shows numerous intensity side lobes (Figure 4.1.2), which will give rise to excitation outside the focal plane. In this case, optical sectioning can be achieved, for instance, by using a pinhole to block the out-of-focus fluorescence [80, 85]. Nevertheless, using pinholes the number of photons that can be detected is less than that detectable with 2PE [84].

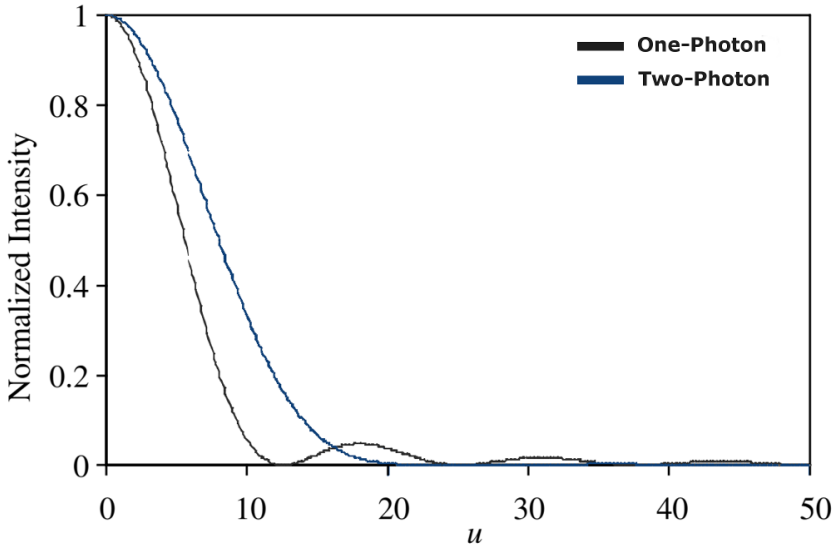


Figure 4.1.2 Comparison of the axial one-photon and two-photon point spread functions. $u$ is the dimensionless axial coordinate. From [80].

### 4.1.2 Second-Harmonic Generation

SHG is a coherent process in which two photons of the same energy (with angular frequency $\omega$), are converted into a single photon with exactly twice the energy (half the wavelength; $2\omega$), when they interact with a nonlinear material (Figure 4.1.3) [86–89]. SHG was first demonstrated in 1961 by Franken *et al.* [90]. The SHG by biological samples was demonstrated one decade later, in 1971, by Fine and Hansen [91]. This gave rise to the development of microscopes based on SHG. The first scanning SHG microscope was developed in the late 1970s [92]. However, it was limited to applications in material science. The first SHG imaging of biological samples was performed in 1986 by Freund and Deutsch [93].

SHG signals arise from the material electric polarization, *i.e.* the dipole moment per unit volume, due to its interaction with the optical radiation electric field [86, 94]. The electric polarization ($P$) is related to the electric field ($E$) by:

$$P = \varepsilon_0\chi^{(1)}E + \varepsilon_0\chi^{(2)}E^2 + \varepsilon_0\chi^{(3)}E^3 + (\dots) \qquad (4.7)$$

where $\varepsilon_0$ is the dielectric constant and $\chi^{(1)}, \chi^{(2)}$, and $\chi^{(3)}$ are the first-, second-, and third-order electric susceptibilities, respectively. The first term describes the linear interaction with the material (*e.g.* absorption), whereas the remaining terms describe

nonlinear interactions. The polarization of second-order in the electric field is the first-order nonlinear term and gives rise to SHG [86, 94–97]. This term is only present when $\chi^{(2)} \neq 0$. Due to the inversion symmetries, this is only valid in media with noncentrosymmetric organization [86, 94, 95]. The second-order nonlinear term gives rise to third-harmonic generation (THG).

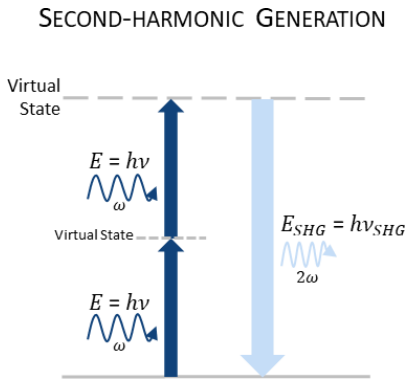


Figure 4.1.3 Energy-level diagram of second-harmonic generation. Two photons with energy $E$ (angular frequency $\omega$) are converted to a single photon with energy $2E$ ($2\omega$). $E$ – energy; $h$ – Planck's constant; $\nu$ – frequency; $\nu_{SHG} = 2\nu$.

The process of SHG can be understood from the correlation between the magnetic field and electric field of the optical wave (electromagnetic theory). From Maxwell's equations of a magnetic medium, without free charges and free currents, the coupled-wave differential equation that govern the SHG process can be derived as:

$$\frac{\partial E_2}{\partial z} = -\frac{i\omega d}{cn_2} E_1^2 e^{i\Delta kz} \quad (4.8)$$

$$\frac{\partial E_1}{\partial z} = -\frac{i\omega d}{cn_1} E_2 E_1^* e^{-i\Delta kz} \quad (4.9)$$

where $d = \frac{1}{2}\chi^{(2)}$ is the nonlinear coefficient and $\Delta k = 2k_1 - k_2$ is the phase mismatch [95–97]. The propagation constants $k_1$ and $k_2$ are given by:

$$k_j = \frac{\omega_j n_j}{c}, j = 1, 2 \quad (4.10)$$

where $n_j$ the refractive index of the medium at a frequency $\omega_j$ [95, 96].

Both electric fields, $E_1$ and $E_2$, vary as a function of the propagation distance ($z$). Therefore, both equations must be solved simultaneously to obtain the second-harmonic

field ($E_2(z)$). However, in the case of low energy conversion efficiencies, it may be assumed that the fundamental field is undepleted ($E_1$ is constant). In this approximation, and being the second-harmonic field $E_2(z)$ zero at $z = 0$, equation 4.8 can be integrated into [95, 96]:

$$E_2(z) = -\frac{i\omega d}{cn_2} E_1^2 e^{i\frac{\Delta kz}{2}} z\, sinc\left(\frac{\Delta kz}{2}\right) \qquad (4.11)$$

where $sinc\left(\frac{\Delta kz}{2}\right) = sin\left(\frac{\Delta kz}{2}\right)/\frac{\Delta kz}{2}$. From equation 4.11, the intensity of second harmonic, *i.e.* the optical power generated by unit of area, can be computed as:

$$I_2(z) = \frac{1}{2} c\varepsilon_0 n_2 |E_2(z)|^2 = \frac{2\omega^2 d^2}{\varepsilon_0 c^3 n_2 n_1^2} I_1^2 z^2 sinc^2\left(\frac{\Delta kz}{2}\right) \qquad (4.12)$$

As it can be perceived from equation 4.12, the second-harmonic intensity has a quadratic dependence on the fundamental intensity ($I_1$) and on the nonlinear coefficient ($d$).

The maximal second-harmonic intensity is achieved when $\Delta k = 0$. This is termed *phase matching condition*. Under phase matching, $I_2$ is also proportional to the square of the distance $z$, whereas without phase matching ($\Delta k \neq 0$):

$$I_2(z) \propto \frac{sin^2\left(\frac{\Delta kz}{2}\right)}{\Delta k^2} \qquad (4.13)$$

and the maximal intensity is achieved at a propagation distance of $\pi/|\Delta k|$. This distance is known as the coherence length ($L_c$) [95, 96]. The variation of the second-harmonic intensity with and without phase matching as a function of the coherence length is shown in Figure 4.1.4.

The phase matching condition implies that the refractive index at frequency $2\omega$ ($n_2$) is equal to the refractive index at frequency $\omega$ ($n_1$). However, since media are typically dispersive, $n_1$ is different than $n_2$. Nevertheless, phase matching might be achieved by using the birefringence properties of the material (birefringence phase matching), *i.e.* by using the refractive index dependence on the polarization direction [96]. Materials with birefringence have double refraction and exhibit ordinary and extraordinary waves, with correspondent ordinary and extraordinary refractive indexes ($n_o$ and $n_e$, respectively)

[95, 97]. Thus, phase matching might be achieved, for instance, between the ordinary wave propagating at angular frequency $\omega$ and the extraordinary wave propagating at angular frequency $2\omega$ [95–97]. However, this method can only be applied for materials that display birefringence and nonlinear coefficients that give maximal energy conversion cannot always be accessed [97]. Alternatively, phase matching can be obtained by creating a period dependence of the nonlinear coefficient $d$ on the propagation depth $z$, which can compensate the phase mismatch. This method is termed quasi-phase matching (QPM) [95, 96]. Under QPM conditions, the efficiency is lower than that achieved under perfect phase matching. Nevertheless, a higher energy conversion efficiencies can be obtained than those without phase matching [97].

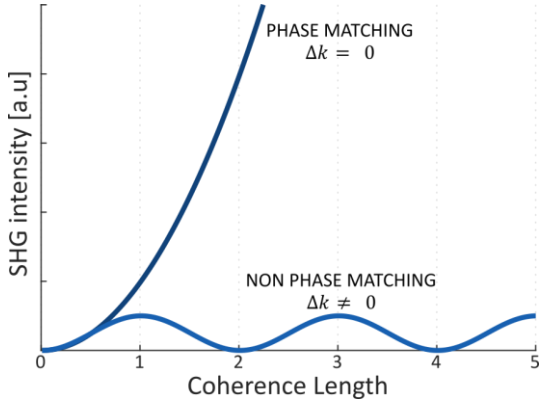


Figure 4.1.4 Second-harmonic intensity under phase matching ($\Delta k = 0$) and without phase matching ($\Delta k \neq 0$) as a function of the coherence length.

## 4.2 Optical setup

TPEF and SHG have comparable system requirements. The typical optical setup of TPI devices is shown in Figure 4.2.1. The light sources used to excite the target molecules for 1PE fluorescence are typically in the ultraviolet (UV) or visible range of the light spectrum. Therefore, to excite the same target molecules using 2PE, each photon must have half the energy (twice the wavelength) to maintain the same overall energy. As such, light sources in the near-infrared (NIR) or infrared range of the light spectrum are typically used for TPEF (Figure 4.2.1). Beside enabling deeper tissue penetration, with NIR light the excitation and emission spectra can be easily separated and the loss of fluorescence is negligible when blocking the excitation light [80]. For SHG imaging, due to the non-

resonant nature of the process, the selection of the fundamental laser wavelength is not as critical as for TPEF. Typically, NIR sources are also used [98, 99]. Moreover, NIR sources enable simultaneous SHG and TPEF imaging.

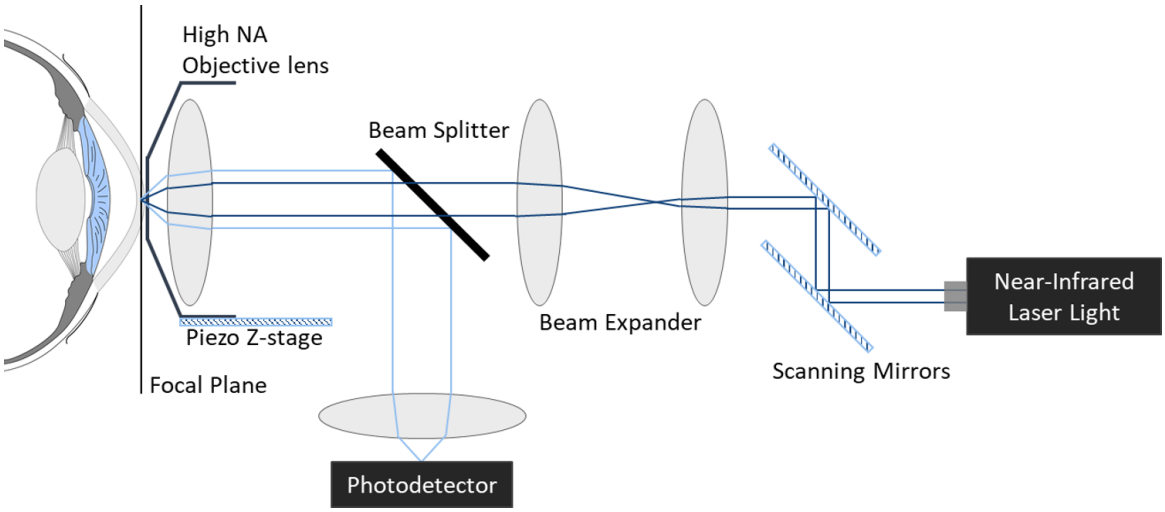


Figure 4.2.1 Schematic representation of the optical setup of two-photon imaging.

High spatial and temporal confinement of photons are required for TPI. The efficiency of two-photon absorption can be expressed as the number of photons absorbed ($n_a$) per fluorophore per pulse as:

$$n_a \approx \frac{\bar{P}^2 \delta_2}{\tau_p f_p^2} \left( \frac{NA^2 \pi}{hc\lambda} \right)^2 \qquad (4.14)$$

where $\bar{P}$ is the average power of the laser, $\delta_2$ is the two-photon cross-section of the fluorophore, $\tau_p$ is the pulse duration, $f_p$ is the repetition rate, $NA$ is the numerical aperture, $c$ is the speed of light, and $\lambda$ is the excitation wavelength [80, 85]. For SHG imaging, the intensity of second-harmonic signals from structural proteins per laser pulse is a factor of:

$$SHG \propto \left[ \frac{p}{a\tau_p} \right]^2 \tau_p \left( \chi^{(2)} \right)^2 a \qquad (4.15)$$

where $p$ is the laser pulse energy and $a$ is the focused spot area [100].

From equation 4.14, it can be perceived that for the same fluorophore and maintaining the excitation parameters constant, the two-photon absorption efficiency can be increased by increasing the objective's $NA$. Using a high NA objective lens (Figure 4.2.1),

a higher concentration of photons in space is accomplished [74, 80, 84]. Similarly, second-harmonic intensity is inversely proportional to the area of the focused beam (Equation 4.15). Considering that the minimal spot size ($s$) of a focused laser as function of the wavelength ($\lambda$) is, according to the diffraction formula of Ernst Abbe, given by:

$$s = \frac{\lambda}{2NA} \qquad (4.16)$$

higher second-harmonic intensities are achieved using high NA objectives [98–100]. From Equation 4.16, the smallest spot sizes are achieved with light sources in the UV range using high NA objectives. For NIR lasers, *e.g.* centered at 800 $nm$, lateral resolutions of the order of 300 $nm$ can be achieved when using objectives with $NA \geq 1.3$.

It can be also perceived from equations 4.14 and 4.15, that although SHG and TPEF rely on two distinct physical mechanisms, their efficiency is inversely proportional to the pulse duration ($\tau_p$) [80, 100, 101]. Using ultra-short laser pulses, temporal confinement of photons is achieved. Ultra-short laser pulses are characterized by a high peak power ($P_{peak}$). However, due to the very short pulse duration ($\tau_p$), the tissue is exposed to a low energy ($E$), computed as:

$$E = P_{peak}\tau_p \qquad (4.17)$$

and to a low average power ($\bar{P}$). The average power of the laser is calculated as:

$$\bar{P} = P_{peak}\tau_p f_p \qquad (4.18)$$

where $f_p$ is the repetition frequency of the laser which is inversely proportional to the time required to complete a roundtrip inside the optical resonator [102]. Therefore, ultra-short lasers deliver high peak powers to the tissue while maintaining overall intensity exposures below the levels of optical breakdown and plasma formation. This makes live tissue imaging possible without inducing laser damage [102].

Because in 2PE systems excitation occurs in a very small volume inside the sample, raster scan using scanning mirrors is required to produce two-dimensional (2D) images (Figure 4.2.1). A piezo vertical stage can be used to change the axial position to produce 3D images (Figure 4.2.1) [80].

The generated signals are then collected by the objective lens and directed, using a beam splitter, to a fast and sensitive photodetector (Figure 4.2.1). Photomultiplier tubes (PMTs) are the most commonly used photodetectors for TPI [80]. The arrival time of generated signals can be additionally recorded for FLIM.

### 4.2.1 Generation of ultra-short laser pulses

The introduction of laser sources was crucial for the experimental development and the subsequent validation of TPI devices. The first laser (Light Amplification by Stimulated Emission of Radiation) was built in 1960 by the American engineer and physicist Theodor Maiman in Malibu (Hughes labs). It was a ruby laser emitting at a wavelength of 694 $nm$ [77]. The laser light is distinguishable from other light sources by being coherent, monochromatic, and collimated, *i.e.,* all emitted photons have the same phase, almost the same wavelength, and move in the same direction [103, 104]. Lasers were soon applied to the medical field. Only one year after its introduction, in 1961, it was used for photocoagulation in the retina of rabbits [105]. In 1962 the procedure was performed for the first time on a patient [106].

Lasers can have two distinct modes of operation: continuous wave or pulsed. However, the most efficient temporal confinement of photons required for TPI is achieved using ultra-short laser pulses, such as picoseconds ($ps, 10^{-12}s$) or femtosecond ($fs, 10^{-15}s$) laser pulses [80, 102]. The generation of ultra-short pulses is usually accomplished using mode-locking [81, 102, 103, 107–109]. The basic principle of this method is to establish a constant phase relationship between the longitudinal modes inside the laser cavity. This will cause the modes to interfere constructively and produce a train of intense laser pulses [108]. The time delay, $T$, between consecutive pulses is given by:

$$T = \frac{2L}{c} \qquad (4.19)$$

where $L$ is the cavity length [81, 102, 108].

In a free running laser, longitudinal modes are stationary waves within the resonator formed due to the constructive interference of light waves in a round trip within the

resonator leading to signal amplification [110]. The number of longitudinal modes ($N_l$) allowed within the resonator is finite, and is related to cavity length ($L$) and spectral bandwidth ($\Delta\nu$) by [102]:

$$N_l = \Delta\nu \frac{2L}{c} \quad (4.20)$$

From the frequencies that satisfy equation 4.20, are emitted by the laser only those that, in a roundtrip, are amplified by the medium with a gain higher than the losses [81, 103, 111]. Since the laser pulse duration and the spectral bandwidth are inversely proportional ($\tau_p \propto 1/\Delta\nu$), the shortest lasers pulses are obtained when the number of longitudinal modes oscillating together and, consequentially, the spectral bandwidth are maximized [81, 102, 108].

Mode-locking can be achieved passively or actively. In active mode-locking, modulators are implemented in the laser cavity and are activated by external signals. Typically, acousto- and electro-optic modulators are used [81, 102, 103, 109]. In passive mode-locking, the Kerr effect is commonly used to lock the phase of the laser modes and generate pulses below 10 $fs$ [81, 103, 107, 108, 112]. The Kerr effect is based on the nonlinear dependence of the refractive index and the intensity of the incident light. Thus, for high intensities, the index of refraction ($n$) becomes:

$$n = n_0 + n_2 I \quad (4.21)$$

where $n_0$ and $n_2$ are the linear and nonlinear refractive indexes, respectively and $I$ is the intensity [102, 109]. A laser with a Gaussian beam has an intensity profile with higher intensities at the center. Thus, as the laser beam passes through a Kerr medium, different refractive indexes will be applied depending on its intensity, leading to the self-focusing of the beam [102, 108, 109, 112, 113]. Kerr lens mode-locking makes the pulse generation energetically preferable to continuous wave [81].

When considering fast pulse production, a wavelength-dependent group velocity must also be considered. Optical elements cause laser pulse dispersion (pulse broadening). This effect is termed group velocity dispersion (GVD) and occurs due to the dependence of the reflective indexes of optical materials with the light wavelength [108]. Therefore, pulse

dispersion must be compensated to guarantee the production of ultra-short pulses and its delivery to the sample [102, 107, 112].

### 4.2.2 Fluorescence lifetime imaging (FLIM)

FLIM is an imaging modality in which the fluorescence decay properties of the sample are measured for every location of the fluorescence image. Thus, FLIM provides both spatial and temporal information, because image contrast is based not only on the fluorophore intensity but also on its lifetime [114, 115]. Time-resolved measurements can be accomplished using both time- or frequency-domain techniques. In the frequency-domain, the fluorophores in the tissue are excited using light sources with high frequency modulation, typically sinusoidal. Due to the modulation of the excitation source, the recorded fluorescence signal will also oscillate with the same frequency. However, due to the finite nature of the fluorescence lifetime, the recorded signal will have an attenuation of the oscillation amplitude (demodulation) and a time delay (phase) compared to the excitation wave. Considering an excitation wave with a sinusoidal modulation of $\cos(\omega t)$, the measured response wave will be in the form of $M\cos(\omega t + \varphi)$, where $M$ is the demodulation and $\varphi$ is the phase. The values of demodulation and phase are then used to compute the fluorescence lifetimes [81, 114–116]. In time-domain FLIM measurements, the fluorophores are excited using pulsed light and the fluorescence time response is measured as a function of time using fast detection acquisition systems [114, 115]. One of the most widely used time-domain FLIM techniques is time-correlated single-photon counting (TCSPC). The principle of operation of TCSPC is represented in Figure 4.2.2.

Using TCSPC, the decay curve of each fluorophore is obtained by measuring the time delay between the excitation pulse and the arrival of the photons [81, 117, 118]. To measure this delay, a part of the laser light is directed to a fast photodiode and sent through a constant fraction discriminator (CFD) into a time-to-amplitude converter (TAC) to generate triggering pulses. Each reference laser pulse resets the TAC. Following sample excitation, the photons are detected by photon detectors operating in single photon mode, *i.e.,* each photon generates an electric pulse which is processed via a CFD and

directed to the TAC. The time difference between the trigger pulse and the generated electric pulse is then computed, converted to a digital signal and stored (Figure 4.2.2). After detecting and accumulating a high number of photons, a histogram is obtained representing the fluorescence decay curve of the sample (Figure 4.2.2) [81, 117, 118]. The fluorescence decay $F(t)$ is typically a multiexponential function of the form:

$$F(t) = \sum_{i=1}^{n} a_i \, e^{\frac{-t}{\tau_i}} \qquad (4.22)$$

where $t$ is the time and $a_i$ the relative contribution of the fluorescence lifetime $\tau_i$.

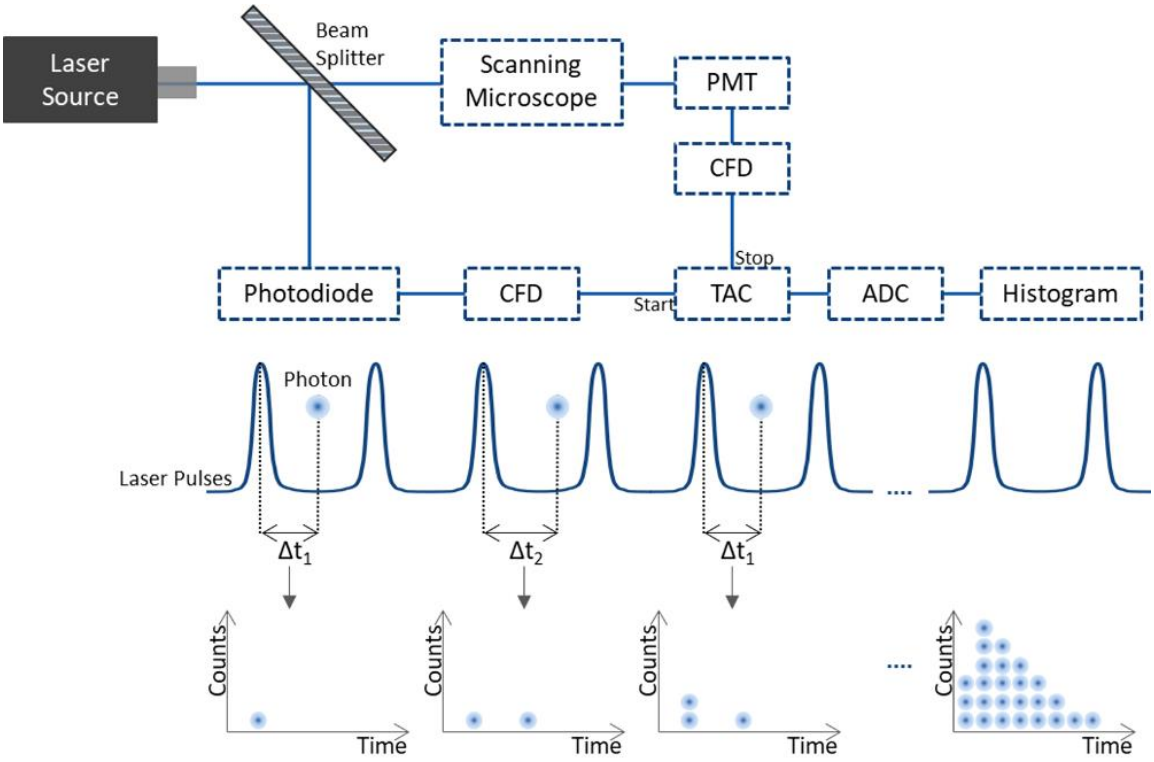


Figure 4.2.2 Schematic representation of the principle of operation of time-correlated single photon counting. PMT – photomultiplier tube; CFD – constant fraction discriminator; TAC – time-to-analog converter; ADC – analog-to-digital converter.

The arrival time of the electric pulse is independent of its amplitude, which makes the measurement of the AF lifetime independent of the fluorescence intensity [81]. However, a high enough number of photons is required to analyze precisely the AF lifetimes of the sample. In an ideal recording system, the fluorescence lifetime ($\tau_i$) of a single-exponential decay can be computed, after collecting $N$ photons, with a standard deviation ($\sigma$) of [119]:

$$\sigma = \frac{\tau}{\sqrt{N}} \qquad (4.23)$$

and the SNR can be determined by [119]:

$$SNR = \frac{\tau}{\sigma} = \sqrt{N} \qquad (4.24)$$

Thus, the lifetime of a fluorophore with a single lifetime component can be obtained with an accuracy of 10% if a minimum of 100 photons per pixel are recorded [119]. However, when the fluorophore has a multi-exponential decay the number of photons required for an accurate analysis of the data highly increases [119–121]. For the accurate analysis of a bi-exponential fluorescence decay curve, a minimum of 1000 photons per pixel is required, depending on the ratio of the fluorescence lifetimes and intensity [119]. In this case, the nearly-ideal photon counting efficiency of TCSPC is highly advantageous. Other advantages of TCSPC over other FLIM methodologies are its high sensitivity, low SNRs, and instrument response function (IRF) stability [117, 118].

Based on the principle of TCSPC, it can be easily perceived that if more than one photon is generated by a laser pulse only the first photon is measured while the remaining are disregarded. This could lead to an over-representation of short lifetime photons in the TCSPC histogram and it is typically known as the 'pile-up' effect. However, for low-level and high-repetition rate signals such as the ones used in TCSPC, the intensity is low enough so that the probability of more than one photon being generated per excitation pulse is negligible [81, 117].

## 4.3 Endogenous sources of contrast

The cornea morphology and metabolism can be retrieved noninvasively and label-free using TPI. For that, we rely on endogenous sources of contrast. In the cell layers, the AF of the metabolic cofactors provides morphological and metabolic information. The concept of using an imaging modality to retrieve the cell's metabolism is often referred to as optical metabolic imaging (OMI). In the corneal stroma, the SHG signal generated by collagen fibers provides information on the structural organization of this layer.

### 4.3.1 Metabolic cofactors

The autofluorescent coenzymes nicotinamide adenine dinucleotide and nicotinamide adenine dinucleotide phosphate (NAD(P)H), as well as the flavin mononucleotide and flavin adenine dinucleotide (flavins), are involved in several steps of the cell's metabolism, *i.e.,* the process by which nutrients are converted into energy in the form of adenosine trisphosphate (ATP) (Figure 4.3.1). This process is essential for tissue health and development and can occur anaerobically or aerobically. In the absence of oxygen, energy is produced via glycolysis in the cytoplasm of cells (Figure 4.3.1). If oxygen is present, the end results of the glycolysis are transported into the mitochondria where they undergo decarboxylation followed by the citric acid cycle and oxidative phosphorylation (Figure 4.3.1). NAD(P)H, present in both the cell cytoplasm and mitochondria, plays a role in both anaerobic and aerobic pathways of energy production, while flavins, which are present exclusively in the mitochondria, are involved only in the aerobic metabolism (Figure 4.3.1). The precise localization of these coenzymes within the cells provides tissue morphology, while their role in the cell's metabolism can be used to retrieve information on their metabolic state.

The feasibility of assessing the cell's metabolism using the AF of the NAD(P)H and flavins is intrinsically related to each fluorophore excitation and emission spectra, quantum yield, fluorescence intensity, and lifetime. Based on the fluorophore's excitation and emission spectra, the ideal wavelengths for selective excitation and detection of each endogenous fluorophore can be determined. The 2PE excitation spectra of NAD(P)H and flavins are slightly shifted towards shorter wavelengths, when compared to their 1PE spectra [83]. NAD(P)H has a 2PE absorption maximum between 690 and 730 $nm$ [76, 122], while flavins have two absorption maxima. The first between 700 and 730 $nm$ and the second at 900 $nm$ [122]. Regardless of the excitation type NAD(P)H and flavins exhibit the same emission spectra [74, 83]. Free NAD(P)H and flavins maximal emission occurs at about 460 $nm$ and 525 $nm$, respectively [76, 122].

The quantum yields of NAD(P)H and flavins are highly affected by their state of oxidation. NAD(P)H and flavins can exist in both oxidized ($NAD^+$/$NADP^+$/FMN/FAD) and reduced (NADH/NADPH/$FMNH_2$/$FADH_2$) forms. However, for NAD(P)H only the reduced forms are

autofluorescent, while flavins AF is only observed for the oxidized forms of the molecule [76, 122, 123]. During the energy production mechanisms, reactions of oxidation/reduction occur in which the metabolic cofactors are reduced and oxidized (Figure 4.3.1). As such, the AF intensity, *i.e.,* the number of NAD(P)H and flavins emitted photons per unit of area, can be used to determine the oxidation/reduction ratio within the cells and infer on its metabolic rate. An increase in the concentration of reduced forms of NAD(P)H as well as of oxidized forms of flavins, results in an AF intensity increase [123]. The ratio between flavins and NAD(P)H AF intensities is most commonly chosen as a redox ratio indicator [122].

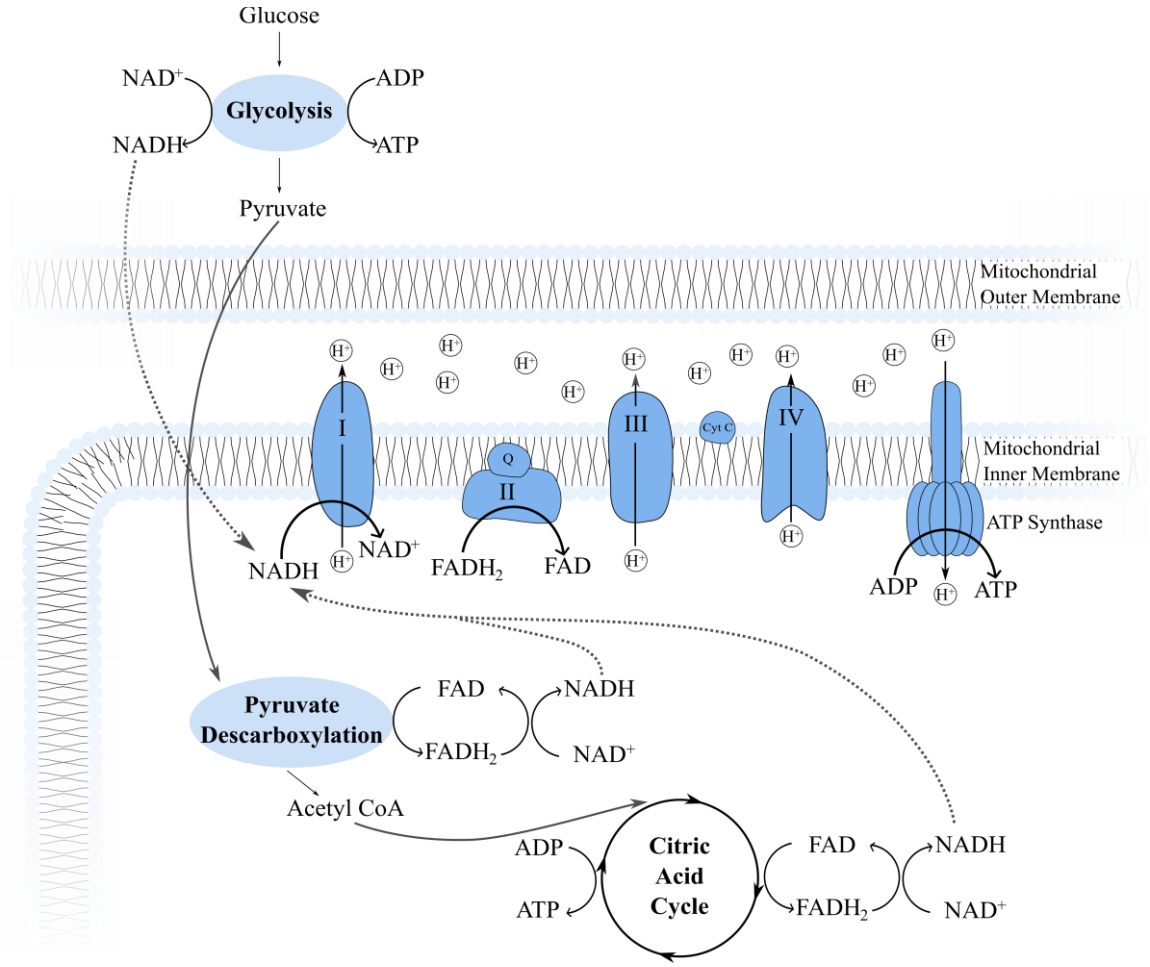


Figure 4.3.1 Simplified representation of the metabolism of glucose with focus on the involvement of the intrinsic fluorophores FAD and NADH. Acetyl CoA – acetyl coenzyme A; ADP – adenosine diphosphate; ATP – adenosine triphosphate; NADH/$NAD^+$ – reduced/oxidized nicotinamide adenine dinucleotide; $FADH_2$/FAD – reduced/oxidized flavin adenine dinucleotide.

The fluorescence lifetime is highly dependent on the fluorophore microenvironment [115]. As such, the same fluorophore can exhibit different lifetimes. The

microenvironmental alteration of interest for metabolic assessment is the bounding to proteins. The oxidation and reduction of NAD(P)H and flavins during energy production is catalyzed by enzymes (Figure 4.3.1) [124]. Therefore, the ratio between the free and protein-bound compounds of these molecules can also be used to determine the oxidation/reduction ratio and consequently the metabolism of cells [122, 125, 126]. In the case of NAD(P)H, a separation of free and protein-bound components based on their AF intensity can also be achieved. When bound to proteins the emission maximum is blue-shifted to 445 $nm$ [127]. Nevertheless, the proximity between the peaks and their spectral overlap hinder the task [127]. In 1992, Lakowicz *et al*. observed that when bound to malate dehydrogenase (enzyme involved in the reactions that occurs during the Citric acid cycle) the lifetime of NADH increased from approximately 0.4 $ns$ to 1.0 $ns$ [128]. Depending on the protein, longer lifetimes can also be observed [76]. In the case of flavins, the AF lifetime drastically decreases upon protein-bounding [76]. Thus, free and protein-bound components can be distinguished based on their fluorescence lifetime. The nearly independence of the lifetime from the concentration of the fluorophore makes the assessment of the metabolic cell state using the AF lifetime less susceptible to artifacts like photobleaching than using the AF intensity [74].

### 4.3.2 Collagen

The most common intrinsic protein of the human body, including the cornea, is collagen [22, 129]. This is a fibrous protein composed of three peptide chains with a tertiary triple-helix conformation (Figure 4.3.2). Individual collagen molecules can form covalent crosslinks with each other to form quaternary structures – fibrils, which can self-assemble into fibers (Figure 4.3.2) [129, 130]. As aforementioned, in the corneal stroma, collagen fibers are further organized into lamellae.

Collagen exhibits intrinsic fluorescence which can be used as an endogenous source of contrast to evaluate the BL, stroma, and DM. Collagen has a 1PE maximum around 340 $nm$ [76, 131]. However, with nonlinear excitation it can be excited in a broad range of wavelengths (between 500 and 1700 $nm$) [132]. The spectral emission maximum of collagen is dependent on the excitation wavelength. An increase in the excitation

wavelength results in a red-shift of the collagen AF emission [133]. Emission maxima between 380 and 520 $nm$ have been reported [76, 131, 133, 134].

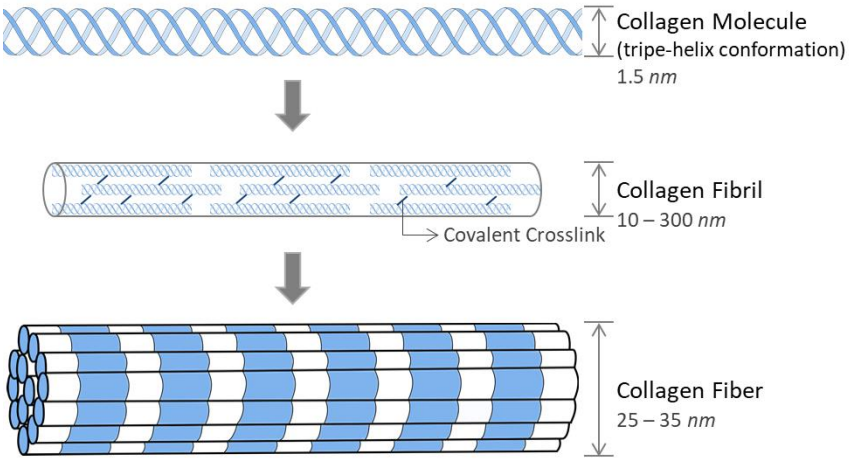


Figure 4.3.2 Collagen molecule conformation and self-assembly via covalent crosslinks into fibrils and fibers.

Two lifetimes components have been reported for collagen molecules. A fast one around 0.3 $ns$ and a slow one between 2.0 and 2.5 $ns$ [135, 136]. The AF lifetime of collagen varies according to its type. For collagen type I, the most abundant type of collagen in the corneal stroma, the slow component of AF lifetime is significantly longer than that of collagen types II, III, and IV [134].

Although the collagen AF may provide valuable information on the cornea, the capacity of collagen to generate SHG is of even more interest. The noncentrosymmetric conformation of collagen makes it an efficient SHG source [87–89, 94, 130]. Using SHG imaging, the orientation and overall degree of organization of the corneal stroma can be retrieved. This property of SHG imaging is intrinsically related to the dependence of the SHG efficiency on the light polarization and sample orientation [88, 98, 137].

As aforementioned, SHG is a coherent process, *i.e.* the second-harmonic wave propagates in forward direction to match the propagation direction of the excitation light. Only in this situation, they will remain phase matched [86–89, 98, 137]. However, in tissue, backward detected SHG signals can be recorded, which enables *in vivo* corneal applications of this imaging modality. The origin of the backward detected signals has been associated with scattering of forward generated second-harmonic signals [88, 98, 137]. It has also been demonstrated that the dispersion and inherent randomness of biological tissues results in imperfect phase matching which leads to generation of forward and backward

components of second-harmonic signals [88, 138, 139]. The higher the mismatch value, the higher backward emitted SHG signals [139]. The direction of SHG depends also on the diameter and packing density of the collagen fibrils. A decrease in the fibril diameter leads to a change of the emission angle of second-harmonic emission from forward to backward direction [88, 140].

# 5 State of the Art of Two-Photon Corneal Imaging

The first attempts to demonstrate the feasibility of using the metabolic cofactors' AF to determine the metabolic state of the cornea cells date to 1978, when Chance and Lieberman measured the redox ratio of the epithelial and endothelial cells of rabbit and cattle corneas using redox fluorometry [141]. In the decade that followed, several studies were published in which redox fluorometry was used to assess the influence of different conditions on the metabolic state of the cornea such as the influence of oxidative phosphorylation inhibitors [142–145], cell preservation medium [146], contact lens wearing [147], and diabetes [148, 149]. Despite demonstrating that the metabolic cofactors' AF could be used to assess the corneal metabolism, redox fluorometry lacked two-dimensionality. The first image of the cornea based on NAD(P)H AF was acquired in 1993 by Masters *et al.* [150]. A confocal microscope coupled with an argon laser for 1PE of NAD(P)H was used to image the cornea of rabbits at the epithelial and endothelial levels [150]. Since NAD(P)H is mainly present in the cytoplasm and mitochondria, the morphology of the cells was recognizable. Thus, this system could provide morphological and metabolic information on the cells. Nevertheless, this system suffered from the already mentioned limitations of 1PE.

The first TPEF AF intensity images of the cornea were acquired in 1995 by Piston *et al.* [151]. Using two-photon laser scanning microscopy with an ultrafast dye laser, generating 150 $fs$ pulses at an excitation wavelength of 705 $nm$, images of the cornea were acquired based on NAD(P)H AF. In the epithelial layer, different cell types were discriminated based on their morphology [151]. The feasibility to detect changes in the cornea metabolism was evaluated using inhibitors of the oxidative phosphorylation. An increase in the AF intensity of the epithelial cells, endothelial cells, and keratocytes associated with the decrease in metabolic activity was observed [151].

The feasibility to detect stromal collagen-generated SHG was demonstrated in the cornea of rabbits shortly after the introduction of this imaging modality [91, 152]. The first SHG images of the cornea in combination with TPEF were performed by König *et al.* and Yeh *et al.* in 2002 to characterize the morphology of porcine [153] and rabbit [154] corneas, respectively. Since then, applications of TPEF in combination with SHG to image the cornea have greatly increased. The morphology of rabbit corneas [151, 154], the porcine eye [153, 155–157] including the sclera, limbus, and conjunctiva [156], the mouse eye without enucleation [158], as well as the human cornea [159, 160], were characterized based on the tissue AF intensity and SHG. *In vivo* imaging of the cornea using TPEF/SHG was demonstrated for rabbits [161–164], mouse [165], and rats [166] but not in humans.

Efforts to determine the best approach to retrieve the collagen fibers orientation from SHG images have also been carried out. These include image analysis techniques such as fast Fourier Transform (FFT) [167–171] or the correlation between neighbor pixels of the image [172–174]. Due to its dependence on light polarization, polarized light is also often used for SHG image acquisition to assess the organization of collagen fibers [166, 175–177].

The organization of the mid and posterior stroma has been determined centrally and peripherally in human corneas based on SHG imaging [178, 179]. Park and coworkers used SHG imaging to describe for the first time two collagenous structures at the limbus [180]. Recently, SHG has also been used to evaluate the collagen organization in the junction between the cornea and the trabecular meshwork [181] and to investigate the collagen organization of the stroma and its connection with DM in endothelial keratoplasty grafts [182].

The possible application of TPEF and SHG as a corneal diagnostic tool has been evaluated. Tan *et al.* demonstrated the feasibility of using these imaging modalities to diagnose and monitor morphological alterations induced by different pathogens responsible for both bacterial and fungal keratitis [183]. Recently, TPI was used to reveal information on the infiltration mechanisms of pathogenic organisms in *ex vivo* and *in vivo* rabbit corneas during corneal infection [164]. Structural changes induced by edema have been revealed based on SHG imaging in bovine [184] and human corneas [159]. Steven and coworkers demonstrated that TPEF could be used to study immune cells transmigration in animal

models of corneal neovascularization [165]. Latour *et al.* reported on the possibility to detected cornea alterations induced by diabetes type 2 using SHG [185]. The feasibility of diagnosing and monitoring keratoconus based on SHG imaging by assessing morphological and structural alterations induced by the pathology to the collagen lamellae patterns of distribution [186], orientations [174, 187], and interweaving [188] has also been reported. Nevertheless, these studies focus on the analysis of AF intensity and collagen structural organization by SHG. FLIM analysis of the cells AF lifetime is important, since pathological conditions are known to affect the metabolic activity.

Along with its diagnosis capabilities, the advantages of using TPEF and SHG for patient follow-up have also been investigated. Several groups reported on the ability of using SHG to detect alterations to the collagen fibers' organization induced by corneal collagen crosslinking (CXL) [170, 189–192], a medical procedure commonly used to treat ectatic disorders such as keratoconus [193, 194]. Moreover, TPEF has been used to assess the riboflavin concentration in the stroma during the CXL process [195–198] which can lead to an improvement of the CXL efficiency. The feasibility of using the same system for tissue monitoring and surgery [153, 155, 157, 162, 163] as well as for monitoring post-surgery wound healing [199] and scar formation [200, 201] has also been tested.

To date, only a small number of FLIM corneal imaging applications exist. 1PE methods were used to evaluate time-related metabolic alterations in rats based on the AF lifetime of flavins [202]. König and coworkers used the 2PE AF lifetime of NAD(P)H to characterize mouse, rabbit, porcine, and human corneas [126]. Moreover, the NAD(P)H AF lifetime of corneal epithelial cells with different storage periods was measured [126]. The feasibility to assess alterations induced to rabbit's corneas by CXL using FLIM was demonstrated by Steven *et al.* [203]. Increases in the stroma AF intensity and lifetime were observed two weeks after CXL [203]. Gehlsen and coworkers reported on corneal wound healing monitoring using NAD(P)H lifetime [204].

With the experimental work that resulted in this PhD dissertation I, together with a group of ophthalmologists and femtosecond laser experts, further contributed to this field. We examined the healthy cornea, characterized the alterations induced to the human cornea due to storage time and by multiple pathologies using the tissue AF intensity, lifetime, and stromal organization, and demonstrated the feasibility of using FLIM to determine the

outcome of CXL soon after treatment. The results were published in several peer-reviewed papers and conference proceedings and are presented and discussed in this dissertation.

# 6 MATERIAL AND METHODS

## 6.1 TWO-PHOTON IMAGE ACQUISITION

In this work, two experimental setups were used for TPI of the cornea: (i) a custom-built two-photon laser-scanning microscope for five-dimensional (5D) microscopy (5D microscope), and (ii) the multiphoton tomograph MPT*flex* (JenLab GmbH, Jena, Germany). Both systems enabled the simultaneous acquisition of AF intensity, lifetime, and SHG. In this section, the instrumental setups of both systems are described.

### 6.1.1 5D Microscope

The instrumental setup of the 5D microscope is shown in Figure 6.1.1A. The system consists of a modified inverted microscope equipped with a NIR mode-locked Ti:sapphire laser (Integral Pro 400; FemtoLasers Produktions GmbH, Vienna, Austria) for sample excitation. The laser generates 10 $fs$ pulses at a frequency of 85 $MHz$ and an average output power of 400 $mW$, corresponding to a peak power of about 0.5 $MW$. Each laser pulse has an M-shaped spectral profile with two main peaks at 775 and 830 $nm$ and a central wavelength around 800 $nm$. The full width at half maximum (FWHM) of the laser spectrum is about 95 $nm$ (Figure 6.1.1B). This large bandwidth allows the simultaneous excitation of multiple fluorophores. The laser beam is guided via mirrors through an attenuator to control the power, a galvanometric scanner unit to change the focal position laterally, and a telescope to expand it (Figure 6.1.1A). A beam splitter is then used to direct the laser beam into the microscope objective for focusing onto the sample. In this system, a 40x NA 1.3 oil immersion objective with a working distance of 210 $\mu m$ is used. The objective is mounted onto a piezo-electric $z$-stage that is used to precisely control the

scanning height, enabling 3D imaging (Figure 6.1.1A). The GVD induced by the optical elements in the beam path is pre-compensated using chirped mirrors. Laser pulse widths below 15 $fs$, measured by autocorrelation, are achieved behind the microscope objective [205].

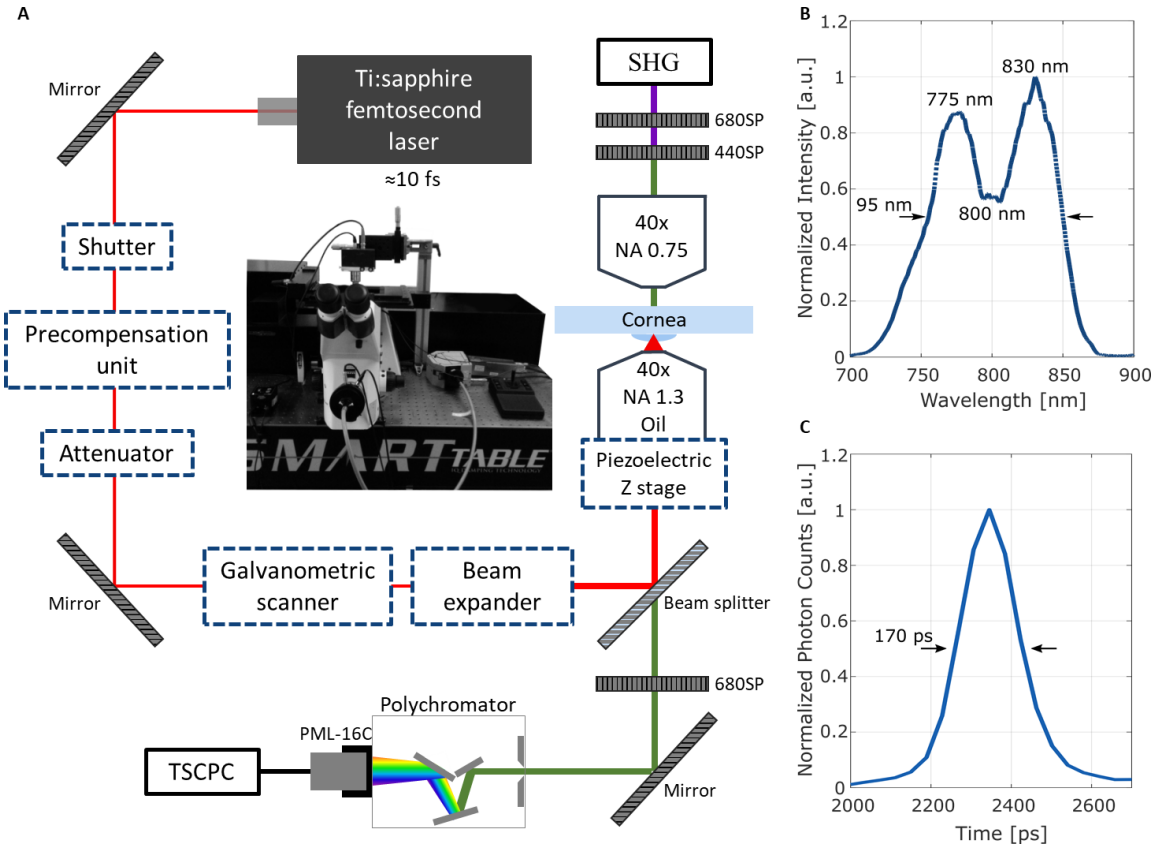


Figure 6.1.1 Schematic representation of the instrumental setup of the custom-built two-photon laser-scanning microscope for 5D microscopy (A). The spectrum of the laser (B) and the second-harmonic generation profile from crystallized urea (C) with the corresponding full width at half maximum are shown.

Signals are collected in reflection geometry, via the same objective and detected by a spectral photomultiplier module, consisting of a polychromator for spectral separation combined with a multi-anode PMT (PML-16C), with maximal efficiency in the green region of the light spectrum and quantum efficiency ($\eta$) below 20%. Detection is accomplished by 16 different channels in a spectral range between 400 and 600 $nm$. The 16-channel PMT detector (16PML-PMT) is coupled to a TCSPC SPC-150 module (Becker & Hickl, Berlin, Germany) for FLIM acquisition (Figure 6.1.1A). The spectra of the tissue and endogenous fluorophores were used to determine the wavelength ranges suitable for analysis of each corneal layer. A 680 $nm$ short-pass filter (FF01-680/SP-25, Semrock Inc., New York) is used

to block residual laser light. The IRF of the system was recorded from the SHG profile of crystalized urea and has a FWHM of ~170 $ps$ (Figure 6.1.1C).

Additionally, SHG signals are collected via a 40x NA 0.75 air objective and detected in forward direction by a single channel PMT detector (H7732; Hamamatsu Photonics, Hamamatsu, Japan) with a $\eta$ < 25 % (Figure 6.1.1A). Forward-emitted AF signals are blocked using a 440 $nm$ short-pass filter (FF01-440/SP-25, Semrock Inc., New York) whereas the laser light is additionally blocked using a 680 $nm$ short-pass filter (FF01-680/SP-25).

The acquisition time for forward-detected SHG images, with 512 × 512 pixels, was 7.4 $s$, corresponding to a pixel dwell time of 0.028 $ms/pixel$. Due to the lower sensitivity (lower $\eta$) and the spectral separation of detected signals, SHG and AF signals detect in reflection geometry using the 16PML-PMT required accumulation over 9 to 13 consecutive frames. Laser powers between 6 and 15 $mW$ were used depending on imaging depth. Each frame with 256 × 256 pixels was acquired within 7.4 $s$, corresponding to a pixel dwell time of 0.11 $ms/pixel$. Up to three non-overlapping areas were imaged per sample.

With the 5D microscope, images can be acquired with lateral (2D), axial (3D), temporal (4D), and spectral (5D) resolutions of 0.3 $\mu m$, (1 – 2) $\mu m$, 170 $ps$, and 12.5 $nm$, respectively.

### 6.1.2 Multiphoton tomograph – MPT*flex*

Figure 6.1.2A shows the certified medical device MPT*flex* and a schematic representation of the instrument's optical setup. The system consists of three main parts (i) an optoelectronic housing, (ii) an articulated mirror-arm, and (iii) a flexible scan head (Figure 6.1.2A). The optoelectronic housing is a movable case that holds the laser and other optical and electronic components. The system is equipped 80 $MHz$ NIR Ti:sapphire laser generating 100 $fs$ pulses with an average output power of about 900 $mW$. The laser wavelength is tunable between 710 and 920 $nm$ which enables the selective excitation of different fluorophores. The laser spectra for the center wavelengths of 760 and 850 $nm$ are shown in Figure 6.1.2B. For both emission wavelengths, the spectra FWHM,

representing the laser bandwidth, is 9 $nm$ (Figure 6.1.2B). The laser pulses are guided via the flexible mirror-arm to the scanning head and focused onto the sample via the objective. In this system, a 40x NA 1.3 oil immersion objective with a working distance of 210 $\mu m$ is used to focus the laser light onto the sample. To allow imaging along the entire corneal thickness this objective was replaced with a 20x NA 1.0 water immersion objective with a working distance of 1700 $\mu m$. At the sample, the laser pulses had widths of ~200 $fs$.

For lateral scanning and acquisition of *en-face* images, two scanning mirrors for $x$ and $y$ directional scanning are used. *En-face* images at different depths are acquired by changing the focal depth using a piezo-driven $z$-scanner. In this way, 3D images of the cornea are recorded. Cross-sectional images are obtained by combining $x$ line scanning with adjustments of the $z$ position of the objective at the end of each line.

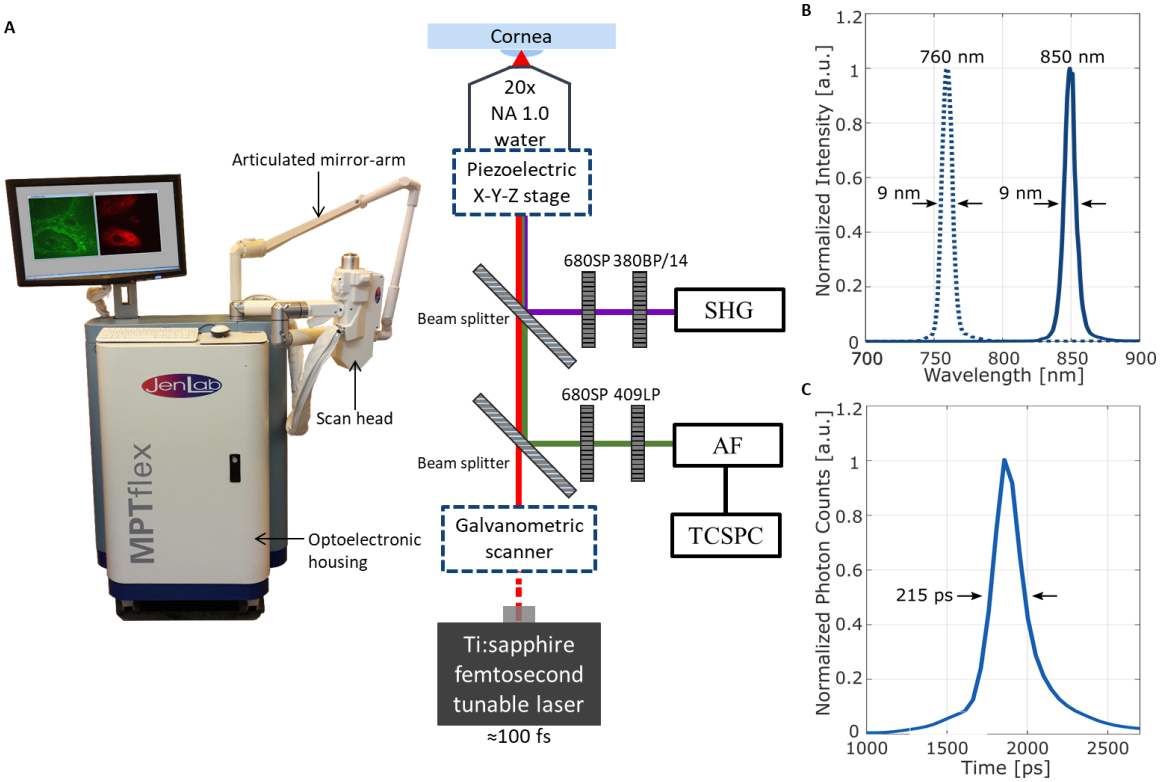


Figure 6.1.2 Multiphoton tomograph MPT*flex* (JenLab GmbH, Jena, Germany) with schematic representation of the optical setup equipped with a 20x NA 1.0 water immersion objective (A). The spectrum of laser (B) and the second-harmonic generation profile from crystallized urea (C) with the corresponding full width at half maximum are shown.

Signals are collected, via the objective, in reflection geometry and detected simultaneously by two PMTs. A beam splitter with a cut-off wavelength of 409 $nm$ is used

to direct short wavelength signals to the first PMT (R1924; Hamamatsu Photonics, Hamamatsu, Japan) with $\eta \approx 26$ % measured at peak sensitivity wavelength (420 $nm$). With excitation wavelengths up to ~810 $nm$, these correspond to SHG photons. A band-pass filter with a transmission window centered at 380 $nm$ and a bandwidth of 14 $nm$ is used to further block AF photons. Long wavelength signals are directed by a beam splitter with a cut-off wavelength of 660 $nm$ to the second PMT (R9880U; Hamamatsu Photonics, Hamamatsu, Japan) with a radiant sensitivity of 130 $mA/W$ measured at peak sensitivity wavelength (400 $nm$) corresponding to $\eta \approx 40$ %. A 409 $nm$ long-pass filter is used to further block short wavelength signals. This detector is coupled to a TCSPC SPC-830 module (Becker & Hickl GmbH, Berlin, Germany) for FLIM acquisition (Figure 6.1.2A). 680 $nm$ short-pass filters are used in both optical paths to prevent residual laser light from reaching the detectors. The apparent SHG profile of crystalized urea was used to acquire the IRF and determine the temporal resolution of the system (Figure 6.1.1C).

Images acquired with the MPT*flex* using the 20x NA 1.0 water immersion objective have lateral, axial, and temporal resolutions of 0.45 $\mu m$, (2 – 3) $\mu m$, and ~215 $ps$, respectively. When using the 40x NA 1.3 oil immersion objective, lateral and axial resolutions improve to 0.30 $\mu m$, (1 – 2) $\mu m$, respectively. An acquisition time of 6.2 $s$ per frame was used to acquire *en-face* images with 512 × 512 pixels, corresponding to a pixel dwell time of 0.024 $ms$ */pixel*. Cross-sectional images with 512 × 1024 pixels were acquired in 68 $s$. Depending on imaging depth, laser powers between 5 and 15 $mW$ were used for image acquisition with the 40x NA 1.3 oil immersion objective. For imaging with the 20x NA 1.0 water immersion objective the laser power varied between 20 and 50 $mW$.

## 6.2 Image analysis

### 6.2.1 Autofluorescence intensity and lifetime

The morphology and metabolic state of the corneal cells was characterized based on the AF intensity and lifetime of their endogenous fluorophores. The AF intensity was

determined based on the total number of photons detected. The AF lifetime was obtained using the commercial software SPCImage (Becker & Hickl GmbH, Berlin, Germany).

The recorded TCSPC histogram is a convolution of the decay curve of the sample with the IRF. As such, for an accurate determination of the sample's AF lifetime, the signal was deconvoluted with the IRF. As aforementioned, the IRFs of the 5D microscope and the MPT*flex* were obtained using the instrumental temporal profiles of crystallized urea (Figure 6.1.1C and Figure 6.1.2C, respectively). The AF lifetimes were then obtained by fitting the fluorescence decay curve (Equation 4.22) to an exponential function. To ensure a sufficient number of photons for a precise analysis of the lifetime data, neighboring pixels were binned prior to data fitting, *i.e.,* their respective photon counts were summed up. The fitting result of the TCSPC data with a bi-exponential decay using SPCImage is shown in Figure 6.2.1.

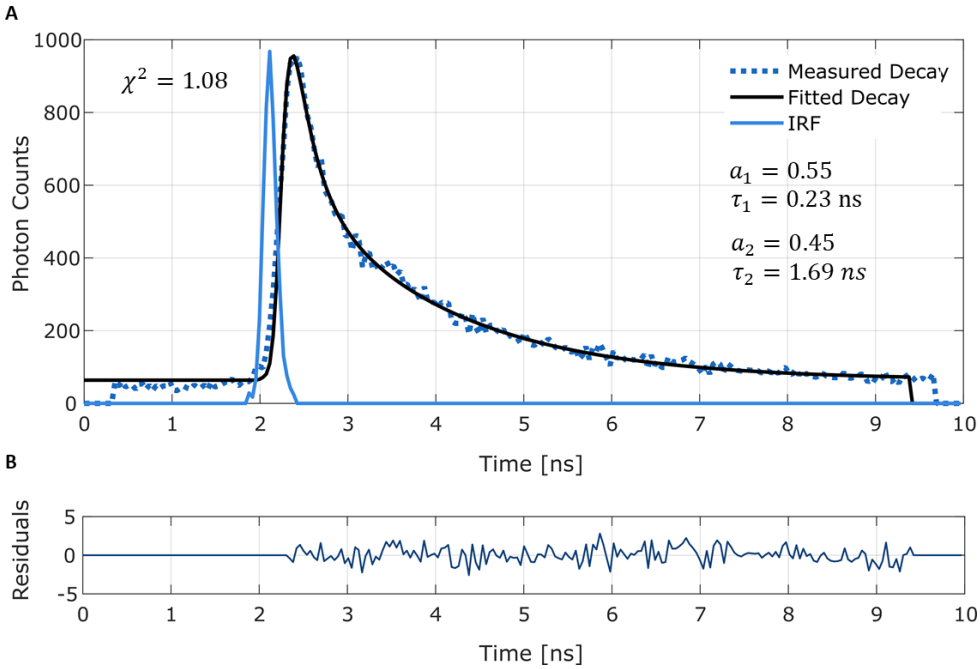


Figure 6.2.1 Fitting of a bi-exponential time-correlated single photon counting (TCSPC) decay curve using SPCImage (Becker & Hickl GmbH, Berlin, Germany). After deconvolution with the instrument response function (IRF), the measured data is fitted with an exponential decay with two-components (A). Residuals distribution (B) and $\chi^2$ value (A) are used to assess fit quality.

The mean AF lifetime ($\tau_m$) of the sample is the average of all lifetime components weighted by their relative contributions:

$$\tau_m = \frac{\sum_{i=1}^{N} a_i \tau_i}{\sum_{i=1}^{N} a_i} \quad (6.1)$$

For a single-exponential decay, $\tau_m$ and $\tau$ correspond to the same lifetime value. In a bi-exponential decay $\tau_m$ is computed as:

$$\tau_m = a_1\tau_1 + a_2\tau_2 \quad (6.2)$$

where the sum of the two relative contributions ($a_1$ and $a_2$) equals one.

The fit quality is assessed based on the weighted residuals curve and $\chi^2$. The latter is computed as:

$$\chi^2 = \frac{\sum_{i=1}^{N} \left[\frac{M_i - F_i}{\sqrt{F_i}}\right]^2}{N - p} = \frac{\sum_{i=1}^{N} R_i^2}{N - p} \quad (6.3)$$

where $F_i$ and $M_i$ are the measured and computed decay points, respectively, $N$ is the total number of data points analyzed, $p$ is the number of fitting parameters, and $R_i$ are the residuals. A good fit is characterized by residual values randomly distributed around zero and a $\chi^2$ close to one (Figure 6.2.1).

### 6.2.2 Second-Harmonic Generation

The generation of second-harmonic signals from the collagen fibers in the cornea was used to assess the organization of the BL and stroma based on the orientation of collagen. Two methods were selected for this evaluation: (i) gray-level co-occurrence matrices (GLCMs) and (ii) a novel metric obtained from fast Fourier transform (FFT) analysis.

GLCM is a statistical tool used to determine the texture of an image by evaluating the relationship between the intensity values of neighboring pixels. It can provide information on regional contrast, energy, homogeneity, and correlation. For the analysis of the collagen fibrillar structures we focused on the correlation between neighboring pixels. Based on this metric, information on collagen geometrical arrangement and its organization with distance can be derived [172, 173, 206]. It has been previously reported

that for collagen organized into linear and distinct fibrils the correlation between the intensity of neighbor pixels decreases rapidly with distance. When collagen organization is less defined, lower correlation values are achieved for longer distances [172, 173, 206].

In this study, GLCMs from SHG images of the stroma were computed using MATLAB (The MathWorks, Inc., Massachusetts, USA). The correlations between the intensity values of adjacent pixels were computed in the vertical, horizontal, and diagonal directions for the same distance intervals in equally sized images.

To demonstrate the feasibility of GLCM to efficiently evaluate the arrangement of collagen within the cornea, two phantom images were generated using MATLAB. A random image was rendered using a uniform random distribution, *i.e.* the intensity of the pixels within the image was randomly attributed. To simulate the fibrillary structures, an image with uniform random distribution was filtered using a directional average filter with a defined direction. The simulated images and the corresponding correlation values are shown in Figure 6.2.2. The correlation between the intensity values of neighboring pixels was computed in the horizontal, vertical, and diagonal directions with displacements between 1 and 32 pixels. As anticipated, in images with simulated fibrillary structures with a defined orientation, a rapid decrease in correlation is observed with distance in all directions (Figure 6.2.2A). For random images, due to the lack of organization, no correlation exists between neighboring pixels with distance (Figure 6.2.2B).

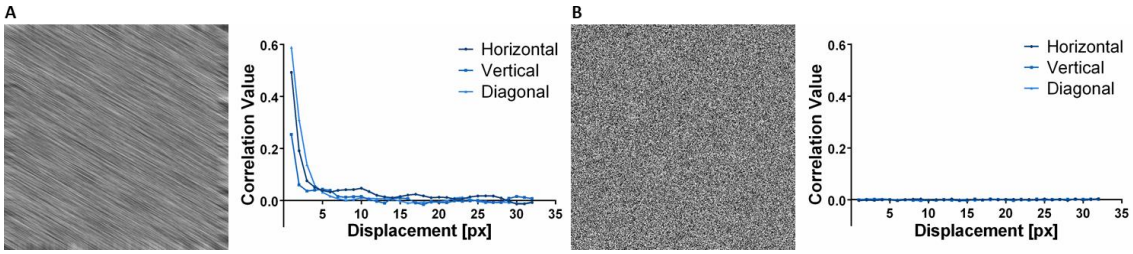


Figure 6.2.2 Validation of the gray-level co-occurrence matrix method. Phantom images with simulated fibrillary organization with defined orientation (A) and random image (B) and their corresponding correlation values in horizontal, vertical, and diagonal direction with displacements between 1 and 32 pixels.

The analysis of the orientation of collagen fibers within the stroma was accomplished using a novel metric, Peak Prominence (PP) developed in collaboration with JenLab GmbH. To retrieve PP from the SHG images, first an FFT is applied to the data based on the description by Mega *et al*. [167]. Briefly, the 2D-FFT image is filtered with a bandpass filter

to reduce both high and low frequency components, followed by a histogram shift to adjust contrast, and a median filter. Then, the radon transform is applied to obtain the prevalence of the different orientations. The main orientation ($d$) of the fibers is computed as:

$$d = \underset{\theta \in \Theta}{\operatorname{argmax}}\, FO(\theta) \qquad (6.4)$$

where Θ is a finite set of orientations ($\Theta \in [0, 180]°$) and $FO(\theta)$ is the frequentness of the orientation $\theta \in \Theta$ in the image derived by the radon transform. The PP is then used to obtain the degree of alignment of the fibers and is defined as:

$$PP = \sqrt{\frac{1}{n-1}\sum_{\theta \in \Theta}\left(FO_{max} - FO(\theta)\right)^2} \qquad (6.5)$$

where $n$ is the cardinality of Θ and $FO_{max}$ is the maximum of $FO(\theta)$. The value of PP indicates how much the orientations of the fibers within the image deviates from the main orientation. For the same area, if all fibers have a similar orientation, a sharp distribution peak and consequently a high PP value are expected, whereas if the fibers are not aligned and are therefore less organized, a disperse distribution peak and a low PP value are anticipated.

To validate our metric, a set of images simulating the fibrous-like pattern of collagen within the stroma was generated using MATLAB. First an image with 512 × 512 pixels was created using a uniform random distribution. This image was then filtered using directional average filters with 15 pixels of length. At each pixel location the orientation of the filter kernel was randomized, according to a normal random distribution of angles, defined by its mean angle of orientation ($\bar{\theta} = \{30, 60, 90, 120, 150\}\}$) and standard deviation ($\sigma_o = \{0, 0.2, 0.4, 0.6, 0.8, 1.0, 1.2, 1.4, 1.6, 1.8, 2.0\}$). All possible combinations of angles of orientation and standard deviations were used to create a total of 126 images. Examples of obtained images for $\bar{\theta}$ = 90° and the respective kernel orientation histograms are shown in Figure 6.2.3A and B, respectively. Narrower histograms, obtained for lower standard deviations, indicate that more pixels are filtered with similarly orientated kernels and the fibrous-like pattern in the image becomes more evident. With a wider histogram

(larger standard deviation), many different kernel orientations are used across the image. In Figure 6.2.3C, an example with a completely uniform random distribution is shown. In this case, no fibrous-like pattern exists.

The values of PP obtained for each orientation angle as a function of the standard deviation are shown in Figure 6.2.3D. As shown, the highest PP values are achieved when most pixels in the image are filtered using equally oriented kernels ($\sigma_o$ = 0). An increase in the standard deviation, leading to a decrease in collagen alignment, results in a progressive decrease in PP (Figure 6.2.3D). The lowest PP value was obtained for images without fibrous-like patterns (PP = 858, Figure 6.2.3C). This indicates that PP can be used to obtain the level of collagen alignment and consequently its level of organization.

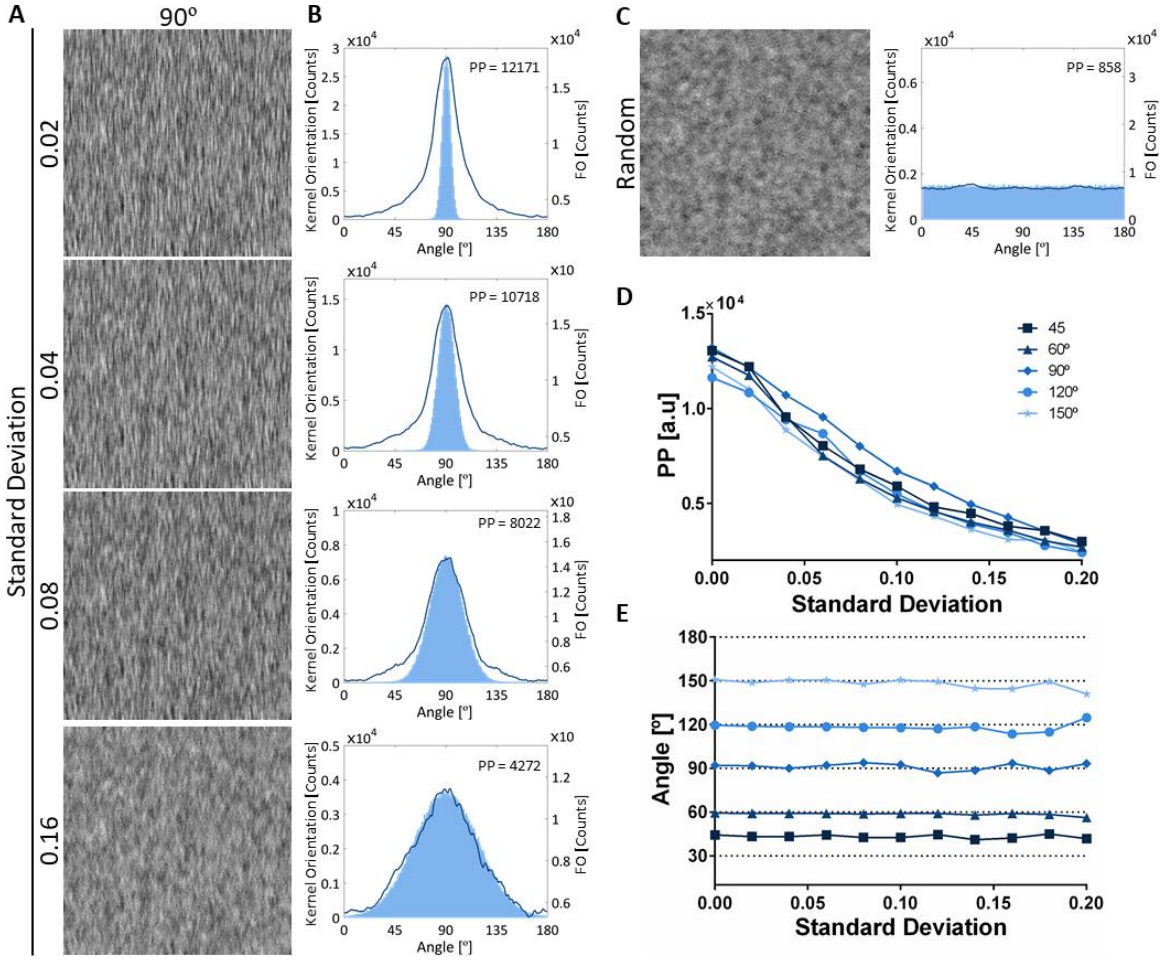


Figure 6.2.3 Validation of the peak prominence (PP) metric. Examples of generated phantom images with a main orientation of 90º and increasingly higher standard deviations (A) and its corresponding kernel orientation histograms and frequentness of orientation ($FO$) obtained for each image (B). Randomly oriented image and its corresponding kernel orientation histogram and $FO$ (C). PP values obtained for each main orientation angle as function of the standard deviation (D) as well as their main orientation angles (E).

The feasibility to assess the main orientation of the fibers is shown in Figure 6.2.3E. Additionally, the frequentness of orientation $FO(\theta)$ obtained for $\bar{\theta}$ = 90° is shown in Figure 6.2.3B. A good overlap between the kernel orientation histograms and $FO(\theta)$ was achieved. Data indicates that the main orientation of the fibers as well as the range of angles present in the image can be accurately determined.

### 6.2.3 3D representations

Depth resolved representations of the tissue were created from individual, sequential, and equally spaced *en-face* images. The matVTK toolbox for MATLAB was used to render the 3D volumes [207].

### 6.2.4 Statistical analysis

The commercial software GraphPad Prism version 6.05 (GraphPad Software Inc., California, USA) was used for the statistical analysis. Statistically significant alterations to the free to protein-bound ratio of NAD(P)H, to the average stroma AF intensity and lifetime, and to the PP value caused by different conditions (*e.g.* storage time, pathologies, and CXL) were computed using the *t-test*. When data did not follow a gaussian distribution or the number of samples was too small, the non-parametric equivalent, *Mann-Whitney U test*, was used. Results were considered as statistically significant if the *p* value was lower than 0.05. The results are presented as averages and standard deviations (SD).

## 6.3 SAMPLE PREPARATION

### 6.3.1 Porcine eyes

Fresh enucleated eyes of pigs aged up to 6 months were obtained from a local slaughterhouse. Phosphate buffered saline (PBS) was used for sample transportation and storage.

Prior to image acquisition, the eyes were dissected. First, the excessive tissue was removed and discarded. Then the cornea was dissected by cutting a central ring with a diameter of 9.0 $mm$ (Figure 6.3.1A) using a corneal trephine blade (Katena Products Inc, New Jersey, USA) or by cutting the eye at the corneal-scleral boundary (Figure 6.3.1B). The excised corneas were mounted in glass bottom Petri dishes from either the epithelial or endothelial sides to image all layers of the tissue. A total of 23 dissected corneas were imaged using the 5D microscope. Additionally, TPI measurements of the cornea on 10 *in vitro* intact eyes (without excision) were also performed using the MPT*flex* (Figure 6.3.1C).

During image acquisition, corneal hydration was maintained using live cell imaging solution (#A14291DJ, Life Technologies, California, USA), a physiological medium specially designed for imaging of live cells. Time-induced alterations were minimized by keeping the entire experiment time, including transport, below 12 $h$.

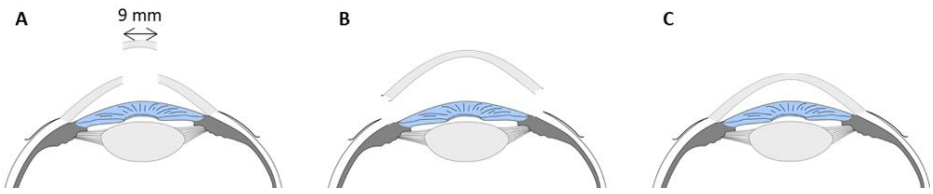


Figure 6.3.1 Representation of porcine cornea preparation prior to two-photon imaging acquisition. Images were acquired from the: dissected corneal rings, cut centrally, with a diameter of 9 $mm$ (A); dissected cornea cut at the corneal-scleral rim (B); intact eye (C).

### 6.3.2 Human corneal donor buttons

Human corneas were provided by the Lions Cornea Bank Saar-Lor-Lux, Trier/Westpfalz at the Department of Ophthalmology, Saarland University Medical Center, Homburg/Saar, Germany. The samples were obtained from donors without corneal diseases and were discarded from transplantation due to viability problem, such as a low endothelial cell counts. These samples were classified as non-pathological (NP).

Prior to image acquisition, corneal donor tissue was stored using organ culture methods [208]. Samples were kept at 34° C under a 5% $CO_2$ atmosphere in culture Medium II with Dextran T500 (#F9017, Biochrom GmbH, Berlin, Germany) supplemented with 5% new-born calf serum (#S0415, Biochrom GmbH, Berlin, Germany). The study was conducted according to the principles of the World Medical Association's Declaration of Helsinki for the scientific use of human tissue.

#### Storage time

Alterations induced by storage time were evaluated by comparing the morphology, metabolism, and collagen fibers' organization of corneas with different storage times. A total of 10 samples were used. They were divided into three groups according to their storage time:

- Short-term storage (STS) – below 1 week of storage (n = 4);
- Medium-term storage (MTS) – between 3 and 4 weeks of storage (n = 3);
- Long-term storage (LTS) – between 8 weeks and 13 weeks of storage (n = 3).

The ECD was (1808 ± 16) $cells/mm^2$ in MTS samples and (1310 ± 382) $cells/mm^2$ in LTS samples. Values were computed as the average between ECD retrieved manually and with the NAVIS cell count system (Nidek Co., Gamagori, Japan). No information was provided on STS samples.

For image acquisition, the samples were rinsed in PBS and placed in glass-bottom petri dishes. Samples were mounted from either the epithelial or endothelial sides to allow

imaging all anatomic layers. Live cell imaging solution was used to keep the hydration of the tissue during measurements.

## Corneal collagen crosslinking

The effect of Accelerated CXL (ACXL) in corneal AF was assessed for a total of 39 NP donor corneal buttons with average storage times of (17 ± 14) weeks. The samples were divided into three groups as illustrated in Figure 6.3.2.

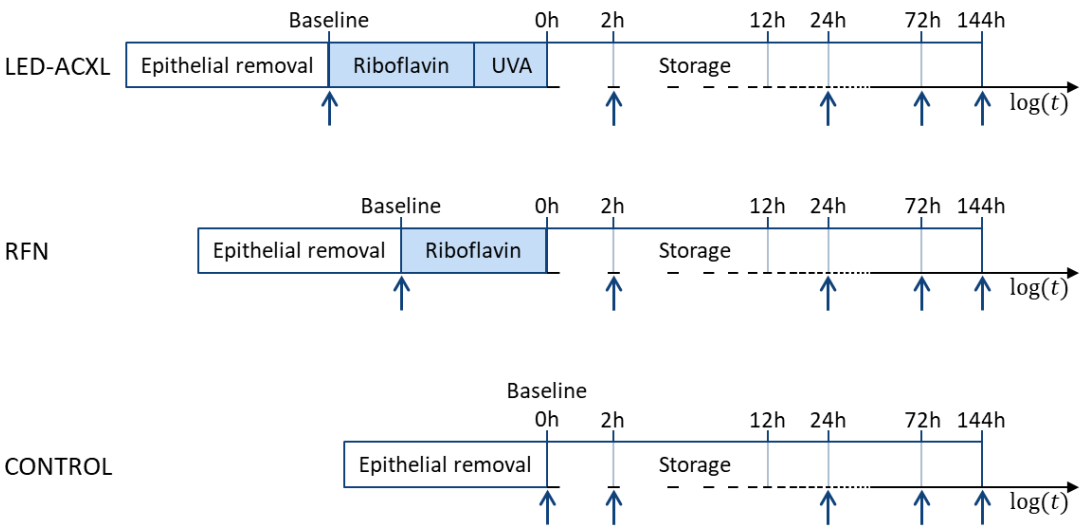


Figure 6.3.2 Schematic representation of the experimental protocol. Vertical arrows represent time points of two-photon image acquisition.

For the LED-ACXL group (n = 14), ACXL was performed after de-epithelialization by applying 0.1% riboflavin solution (Vibex rapid™ Avedro, Inc., MA, USA) every 2 $min$ for 20 $min$ (Figure 6.3.3A) and irradiating with an UVA light source for 10 $min$ (Figure 6.3.3B and C). UVA irradiation was performed using an in-house adapted ACXL setup consisting of a light-emitting diode (LED) emitting at a wavelength of 365 $nm$ mounted in an inverted microscope (Figure 6.3.3). To assess the feasibility of our setup to perform ACXL, LED-crosslinked corneas were compared with samples crosslinked using the commercial ACXL system KXL™ (Avedro, Inc., MA, USA). A total of 6 samples were crosslinked using the KXL system. With both ACXL setups, the UVA emission wavelength was 365 $nm$. *A* total irradiance of 12 $mW/cm^2$ corresponding to an energy dose of 7.2 $J/cm^2$ was used. This energy dose has been demonstrated to be as effective as the conventional 5.4 $J/cm^2$ to perform ACXL [66, 209].

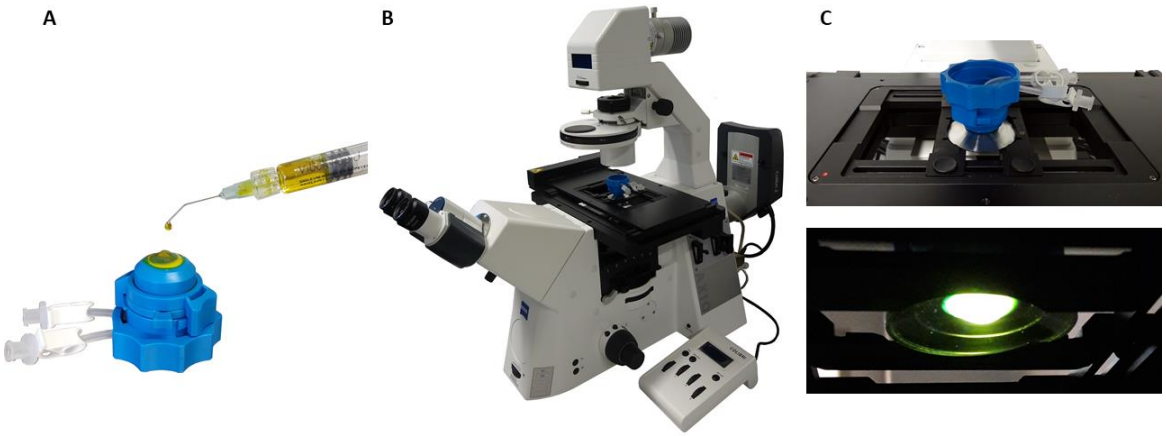


Figure 6.3.3 Application of riboflavin drops (A) and the in-house adapted setup for irradiation of the cornea with UVA light (B), with close ups of the cornea irradiation process (C).

For the RFN group (n = 9), the samples were infused with 0.1% riboflavin solution (every 2 $min$ for a total of 20 $min$) without UVA irradiation. The samples in the control group (n = 10) were not treated (Figure 6.3.2).

Additionally, two keratoconus corneas were used. ACXL was performed in one of the samples and the other was used as control. Signed and informed consent was obtained from the patients.

For image acquisition, with the MPT*flex*, corneas were mounted in an artificial anterior chamber as demonstrated in Figure 6.3.4. Hydration of the samples was maintained throughout the measurements using live cell imaging solution. For all groups, images were acquired immediately after epithelial removal (baseline) and 2, 24, 72, and 144 $h$ later (Figure 6.3.2).

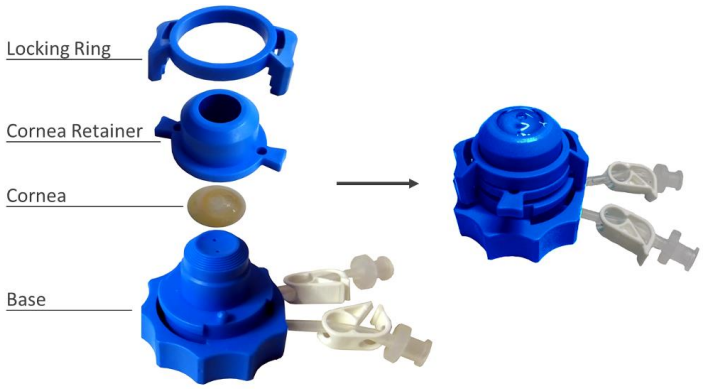


Figure 6.3.4 Mounting of human corneas into artificial anterior chambers.

### 6.3.3 Pathological human corneas

Pathological changes induced to the corneal morphology, metabolism, and structural organization were assessed by comparing NP STS donor corneal buttons with corneas of patients suffering from:

- Keratoconus (n = 5);
- *Acanthamoeba* keratitis (n = 1);
- Stromal corneal scars (n = 1).

Pathological samples were provided by the Department of Ophthalmology, Saarland University, Medical Center, Homburg/Saar, Germany. Immediately after keratoplasty, the excised samples were stored under the same conditions as the human corneal donor tissue to preserve sample viability and minimize time-induced alterations.

Prior to image acquisition, samples were rinsed in PBS and mounted in individual glass bottom petri dishes. Sample hydration was maintained using live cell imaging solution. All experimental procedures were performed within 24 $h$ after surgery. Imaging acquisition was performed using the 5D microscope. Patients have provided written and informed consent for the use of their tissue for research purposes.

# 7 RESULTS

The main purpose of this work was to demonstrate the potential of TPI as a novel ophthalmological clinical device for corneal imaging. For that, I demonstrated the feasibility of two different TPI systems to evaluate the cornea and provide novel information to aid tissue evaluation. I started this work, by examining the safety of the acquisition parameters used with each TPI system as well as their ability to image different endogenous fluorophores (section 7.1). Then, I characterized the cell's morphology and metabolic activity, as well as the stroma organization in porcine corneas using TPI (section 7.2). The characterization of human corneas and the advantages of TPI for sample evaluation during storage in cornea banks were then assessed and are described in section 7.3. Finally, I demonstrate the potential of TPI for the diagnosis of different corneal pathologies (section 7.4) and the evaluation of the clinical outcome of CXL (section 7.5).

## 7.1 CHARACTERIZATION OF TPI INSTRUMENTS

### 7.1.1 Optical window for safe TPI

In TPI, good image contrast as well as an accurate analysis of the AF lifetime data rely on a sufficiently high number of photons. Therefore, the parameters, namely the mean laser intensity and acquisition time, used for image acquisition with the 5D microscope and the MPT*flex* were tested and optimized. From Equation 4.14 it is easily perceived that an increase in the laser intensity will increase the number of absorbed photons per pulse. Longer acquisition times also result in an increase of the total number of absorbed photons. Therefore, both acquisition parameters must be increased to obtain maximal

photon counts. However, tissue safety must also be considered when imaging biological samples since high laser intensities can ultimately lead to damage. Therefore, the possible phototoxicity induced by the imaging parameters of both systems was evaluated by monitoring the AF intensity and cell morphology of the corneal epithelial layer. The results presented here were partially published in Batista *et al*. "*Two-Photon Spectral Fluorescence Lifetime and Second-Harmonic Generation Imaging of the Porcine Cornea with a 12 Femtosecond Laser Microscope*" Journal Biomedical Optics 21(3), 036002:1-11, 2016 [210].

Photon detection was accomplished with the 5D microscope using the spectral detector 16PML-PMT. Although the spectral separation of the detected photons is an advantage, the low quantum efficiency of this detector ($\eta$ < 20 %) requires the accumulation of several frames to obtain enough photon counts for lifetime data analysis. Typically, 9 to 13 frames were accumulated using a maximal laser power of 15 $mW$ and pixel dwell times of 0.11 $ms/pixel$. To evaluate the effect of these imaging parameters on the tissue, the AF intensity and morphology of porcine corneal epithelial cells was monitored over 20 consecutive images acquired using laser powers of 15 $mW$ and the same pixel dwell times. Three non-overlapping areas were measured per sample. A decrease of 4 % in the AF emission was observed during the first 10 images due to photobleaching followed by a stabilization. No alteration to the cell's morphology was observed (Figure 7.1.1A).

Changes induced by image acquisition with the MPTflex to the morphology and AF intensity of porcine superficial cells were examined in three non-overlapping areas. Images were acquired over 5 consecutive frames using an excitation wavelength of 760 $nm$, pixel dwell times of 0.024 $ms/pixel$, and a laser power of 10 $mW$. As shown in Figure 7.1.1B, the number of detected photons was approximately constant throughout the measurement and no visible alterations were observed in the morphology of the cells. This indicates that the acquisition parameters selected for both systems are safe for corneal imaging.

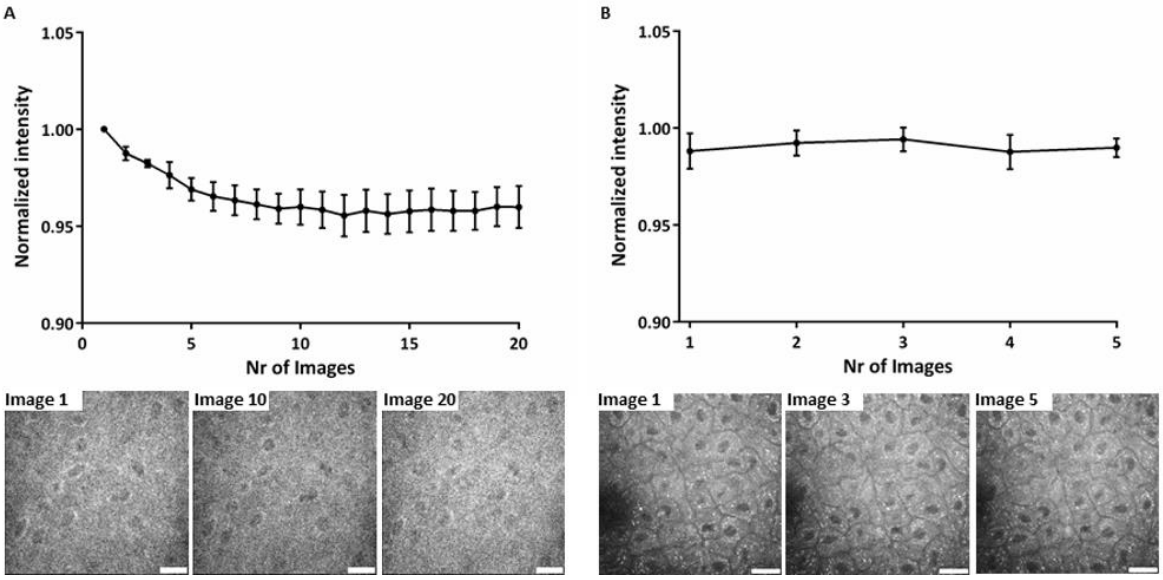


Figure 7.1.1 Laser-induced changes to porcine corneal epithelial cells autofluorescence intensity (top) and morphology (bottom) during 20 and 5 consecutive images acquired with the 5D microscope (A) and the MPT*flex* (B), respectively. Scale bar = 20 $\mu m$. Data partially published in [210].

### 7.1.2 Spectral separation of the detected signals

The excitation and detection of multiple fluorophores is possible using both the 5D microscope and the MPT*flex*. With the former, the large bandwidth of the excitation laser (Figure 6.1.1B) enables the simultaneous excitation of multiple fluorophores while the spectral detector system allows separation of the detected signals based on their wavelength. Using the MPT*flex*, the excitation laser can be tuned to different wavelengths to selectively excite specific fluorophores (Figure 6.1.2B) and signal detection is performed simultaneously by two distinct PMTs. Since in each layer of the cornea multiple endogenous sources of contrast can contribute to the detected signal, the feasibility to excite and detect different fluorophores was analyzed for both systems. For that purpose, the spectra of different corneal layers and of pure reference solutions of endogenous fluorophores were acquired. The results presented here were partially published in Batista *et al*. "Assessment of the metabolism and morphology of the porcine cornea, lens, and retina by two-photon imaging" Journal of Biophotonics 11(7), e201700324, 2018 [211].

Corneal cells are metabolically active and AF signals from the metabolic cofactors NAD(P)H and flavins are expected. Therefore, the spectra of pure solutions of NADH

(#N8129, Sigma-Aldrich, USA), and FAD (#F6625, Sigma-Aldrich, USA) in Tris hydrochloride solution (#T1944, Sigma-Aldrich, USA) were recorded (Figure 7.1.2A). The cornea BL, stroma, and DM are mainly composed of collagen. Thus, the spectrum of lyophilized collagen type I (#C5983, Sigma-Aldrich, USA) was recorded as a reference (Figure 7.1.2B). Due to the generation of SHG from collagen fibers, a reference SHG spectrum was also recorded from crystalized urea (Figure 7.1.2B).

Sample excitation was accomplished using the 10 $fs$ laser with broad bandwidth centered at 800 $nm$ (L800) of the 5D microscope, and the tunable laser of the MPT*flex* tuned at 760 $nm$ (L760) and 850 $nm$ (L850) for selective excitation of NAD(P)H and flavins, respectively.

Using the spectral characteristics of the 16PML-PMT, the spectra were reconstructed based on the number of photons detected per channel. The accuracy of the reconstructed spectra was verified using a thermoelectric-cooled CCD-array spectrometer (BTC112, B&W Tek, Newark, USA). Spectra recorded with the BTC112 were corrected for the sensitivity of the spectrometer and the spectral transmission efficiency of the optical path. To correct for its sensitivity, the spectrum of a halogen lamp was recorded as a reference and corrected to match the spectrum of a black body with a temperature of 3300 *Kelvin*. The transmission of the optical path was corrected by comparing the halogen lamp spectrum acquired through the optical path with the spectrum recorded directly.

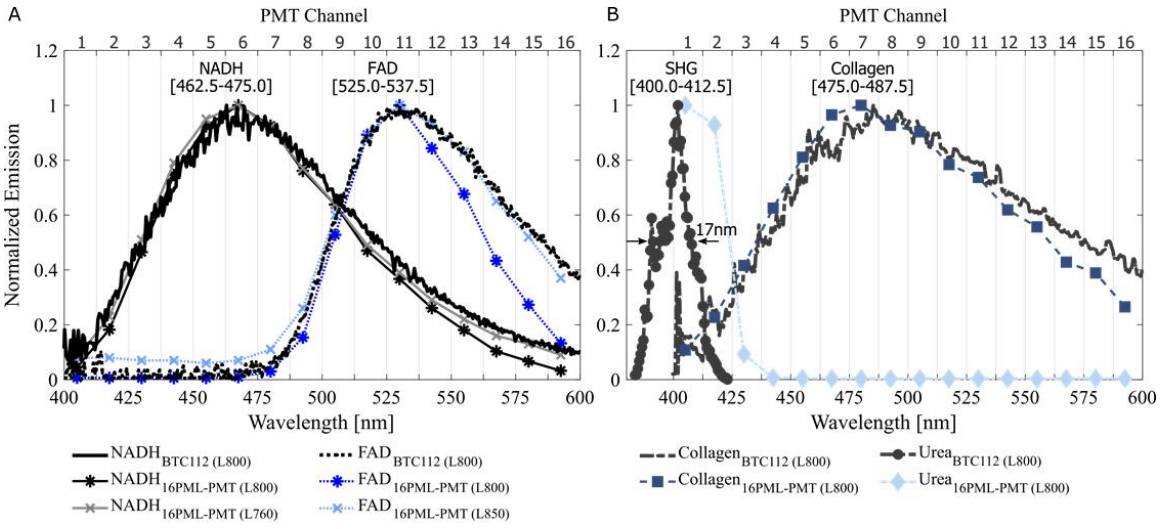


Figure 7.1.2 Fluorescence emission spectra of pure solutions of NADH and FAD (A) in Tris hydrochloride and of lyophilized collagen type I, and SHG from crystallized urea (B). The spectra were obtained with the 16-channel PMT detector (16PML-PMT) and a spectrometer (BTC112). The fluorophores were excited using a 10 $fs$ broad bandwidth excitation laser centered at 800 $nm$ (L800) and using a 100 $fs$ laser tuned at 760 $nm$ (L760) or 850 $nm$ (L850). Data published in [211].

As shown in Figure 7.1.2, the spectra reconstructed from the 16PML-PMT and the spectra measured with the BTC112 spectrometer are in good agreement, demonstrating the accuracy of the reconstructed spectra. With both acquisition methods, maximal NADH and FAD emissions were observed in the spectral intervals between 462.5 and 475.0 $nm$ and between 525.0 and 537.5 $nm$ corresponding to the PMT channels numbers 6 and 11, respectively. Moreover, simultaneous excitation of NADH and FAD using the broad bandwidth laser (L800) yielded similar spectra as narrow band selective excitations using L760 and L850, respectively (Figure 7.1.2A). The maximum collagen AF emission was observed between 475.0 and 487.5 $nm$ with both spectra acquisition methods (Figure 7.1.2B). The SHG reference spectrum was obtained from laser light interaction with crystallized urea (Figure 7.1.2B). Although the SHG maximum emission was the same with both acquisition methods, a broader peak was observed with the 16PML-PMT when compared with the BTC112 (Figure 7.1.2B). The SHG spectrum recorded had a FWHM of 17 $nm$ (Figure 7.1.2B). The lower spectral resolution of the 16PML-PMT, results in a strong SHG signal detection in the first two channels of the detector (Figure 7.1.2B).

The feasibility to detect and discriminate between different corneal fluorophores when using the 5D microscope was assessed by recording the spectra of porcine corneal epithelium, stroma, and endothelium using the 16PML-PMT (Figure 7.1.3). The spectra of the cellular layers (epithelium and endothelium) had a single emission maximum in the spectral range between 437.5 and 450.0 $nm$, corresponding to the PMT channel number 4 (Figure 7.1.3A). The emission spectrum of cornea cells resembles the spectrum of pure NADH solution. However, the spectra of the cornea epithelium and endothelium are shifted to shorter wavelengths. This might be due to the presence of protein-bound components of the fluorophore within the tissue. Protein-bound NAD(P)H has a maximal fluorescence emission at 445 $nm$ [127]. Due to the presence of NAD(P)H free and bound to proteins a broader spectrum was also observed in the corneal cell layers. In the spectral PMT channel numbers 5 and 6 the decreases in the total photon counts were on average 3% and 8%, respectively. Due to the spectral resolution of the 16PML-PMT and the proximity between the AF emission maxima of NADH free and bound to proteins, the discrimination of the two emission peaks was not possible.

Selective excitation of flavins within the cornea was performed using L850. As shown in Figure 7.1.3A, this yielded a relatively flat spectrum. Two peaks with low photon counts were observed in the PMT channel numbers 3 and 15 probably due to artifacts. In the spectral range where flavin emission is maximal (between 525.0 and 537.5 $nm$), the number of photons detected was very low. Moreover, selective excitation of NAD(P)H using L760 resulted in a similar cornea-epithelial spectrum as the simultaneous excitation of NAD(P)H and flavins within the tissue using L800 (Figure 7.1.3A). This indicates that although flavins are present in the corneal cells, their contribution to the AF detected signal is negligible when compared to the AF signal originating from NAD(P)H.

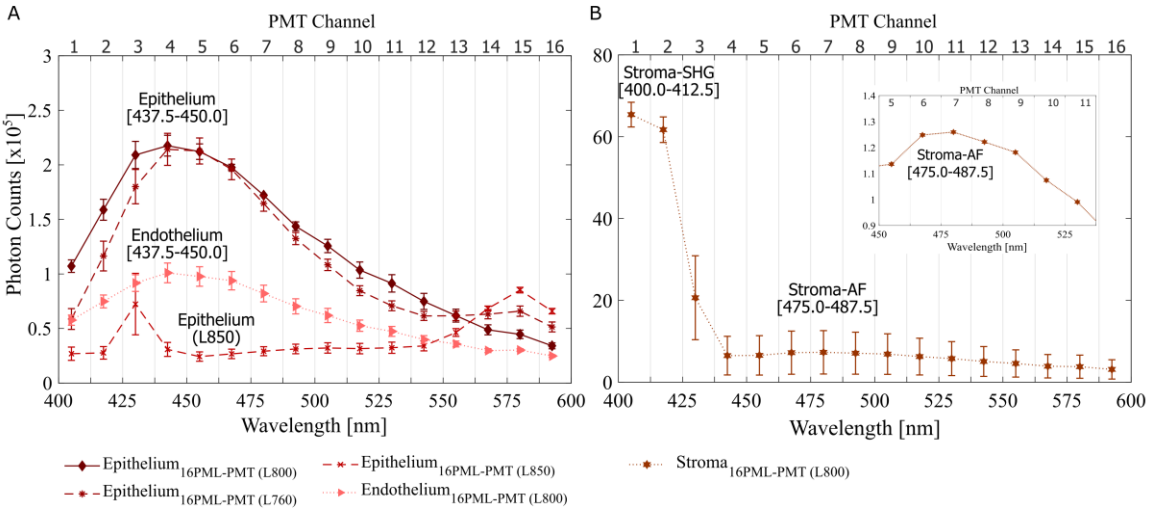


Figure 7.1.3 Autofluorescence emission spectra (as average ± SD) of the cornea epithelium and endothelium (A), and stroma (B). The spectra were obtained with the 16-channel PMT detector (16PML-PMT). The fluorophores were excited using a 10 $fs$ broad bandwidth excitation laser centered at 800 $nm$ (L800) and using a 100 $fs$ laser tuned at 760 $nm$ (L760) or 850 $nm$ (L850). Data published in [211].

The feasibility of detecting autofluorescence signals from both NAD(P)H and flavins in the corneal epithelial layer using the MPT*flex* was determined through the analysis of the total number of photons collected using different excitation wavelengths (710, 760, 800, 850, and 900 $nm$). Up to five non-overlapping areas from three porcine corneas were acquired. The average photon counts and representative images of the porcine cornea epithelial layer, obtained with each excitation wavelength are shown in Figure 7.1.4.

A drastic decrease in the number of detected signals was observed with the increase of the excitation wavelength (Figure 7.1.4). Considering the excitation spectra of NAD(P)H and flavins, fluorescence absorption and emission of both fluorophores was anticipated when using short excitation wavelengths. Therefore, the high number of photons

detected for excitation wavelengths of 710 $nm$ and 760 $nm$ was expected. The molar attenuation coefficient of NAD(P)H decreases with the increase of the excitation wavelength, and above 850 $nm$ flavins are exclusively excited [83]. Thus, the low number of photons detected using excitation wavelengths above 850 $nm$ indicate that, when using the MPT*flex*, the detection of flavins from the corneal epithelial cells is negligible.

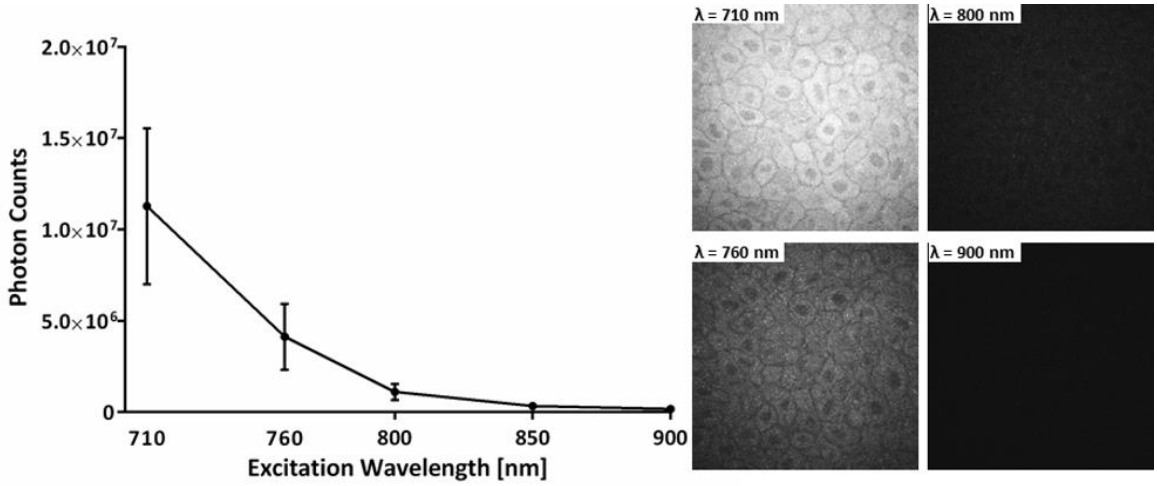


Figure 7.1.4 Total number of photons detected from the porcine corneal epithelial layer using different excitation wavelengths (left). Representative autofluorescence intensity images are shown (right). Data acquired using the MPT*flex*.

The emission spectrum of the cornea stroma had a maximum between 400.0 and 412.5 $nm$ which is consistent with a SHG signal at half the excitation laser wavelength (Figure 7.1.3B). Additionally, this layer has weak AF emission from collagen and keratocytes NAD(P)H AF. Maximal AF emission was observed between 475.0 and 487.5 $nm$, corresponding to the PMT channel number 7 (Figure 7.1.3B).

Using the 5D microscope, spectral separation of the detected signals was performed based on the emission spectra of the corneal layers and of the pure fluorophores. The selected spectral ranges of the 16PML-PMT better suitable for the analysis of each layer of the cornea are shown in Table 7.1.1. For the cornea epithelium and endothelium, a spectral range suitable for NAD(P)H detection was selected. For the BL, stroma, and DM, where collagen is the major source of AF, a spectral range corresponding to this fluorophore emission was chosen. For analyzing the stroma, spectral ranges suitable for the analysis of SHG emission and NAD(P)H emission from keratocytes were also used. Moreover, due to the spectral overlap between collagen and NAD(P)H AF emissions, the

analysis of keratocytes AF was performed in selective regions of interest (ROI). Using the MPTflex, an excitation wavelength of 760 $nm$ was selected for excitation of NAD(P)H within the corneal cells and of collagen in the stroma.

Table 7.1.1 Detection wavelength ranges and corresponding PMT channels selected for the analysis of the autofluorescence of different corneal layers using the 5D microscope.

| Corneal layer | Wavelength range [$nm$] | PMT channels |
|---|---|---|
| ***Epithelium*** | 425 – 500 | 3 – 8 |
| ***BL*** | 425 – 575 | 3 – 14 |
| ***Stroma SHG*** | 400 – 425 | 1 – 2 |
| ***Stroma Collagen AF*** | 425 – 575 | 3 – 14 |
| ***Stroma NAD(P)H AF*** | 425 – 500 | 3 – 8 |
| ***DM*** | 425 – 575 | 3 – 14 |
| ***Endothelium*** | 425 – 500 | 3 – 8 |

## 7.2 TPI OF PORCINE EYES

Porcine corneas were imaged and characterized using both the 5D microscope and the MPT*flex*. In this section, the simultaneous assessment of the tissue morphology, metabolic activity, and organization of collagen fibers using TPI is addressed. NAD(P)H AF intensity was used as a contrast mechanism for morphological evaluation. The ratio between the free and protein-bound components of this metabolic cofactor was used to infer on and compare the metabolic activity of different cell types. The structural organization of the corneal stroma was assessed using SHG signals collected in both forward and backward directions. The organization of the collagen fibers was obtained using FFT analysis. The results presented here were partially published in Batista *et al*. "*Two-Photon Spectral Fluorescence Lifetime and Second-Harmonic Generation Imaging of the Porcine Cornea with a 12 Femtosecond Laser Microscope*" Journal Biomedical Optics 21(3), 036002:1-11, 2016 [210].

### 7.2.1 Porcine cornea morphology

Using TPI, the morphology of the porcine cornea was evaluated at multiple depths based on its AF intensity and SHG using both acquisition systems (5D microscope and MPT*flex*). Images of all corneal layers, as well as the interfaces between them, are shown in Figure 7.2.1. In the corneal epithelial layer, single cells are visible. As such, the discrimination into superficial, wing cells, and basal cells using their anatomic characteristics is possible. Moreover, due to the sub-cellular resolution of TPI, the mitochondrial distribution within the cells is visible. In superficial cells, mitochondria appear spread out around the cell cytoplasm, whereas in basal cells these organelles are preferably located around the nucleus (Figure 7.2.1).

Posteriorly to the epithelium, SHG signals from the highly organized collagen fibers of the stroma were immediately detected. Thus, confirming the lack of BL in pigs. Backward

detected SHG images of the stroma at two different depths (94 and 128 $\mu m$) are also shown. In the DM, collagen AF signals were detected.

In the corneal endothelium, individual cells are visible and their honeycomb-like organization recognizable (Figure 7.2.1). These cells are regularly shaped. Average widths of (24.3 ± 2.2) $\mu m$ were measured. The ECD determined based on the number of cells in the field-of-view was found to be (2350 ± 146) $cells/mm^2$.

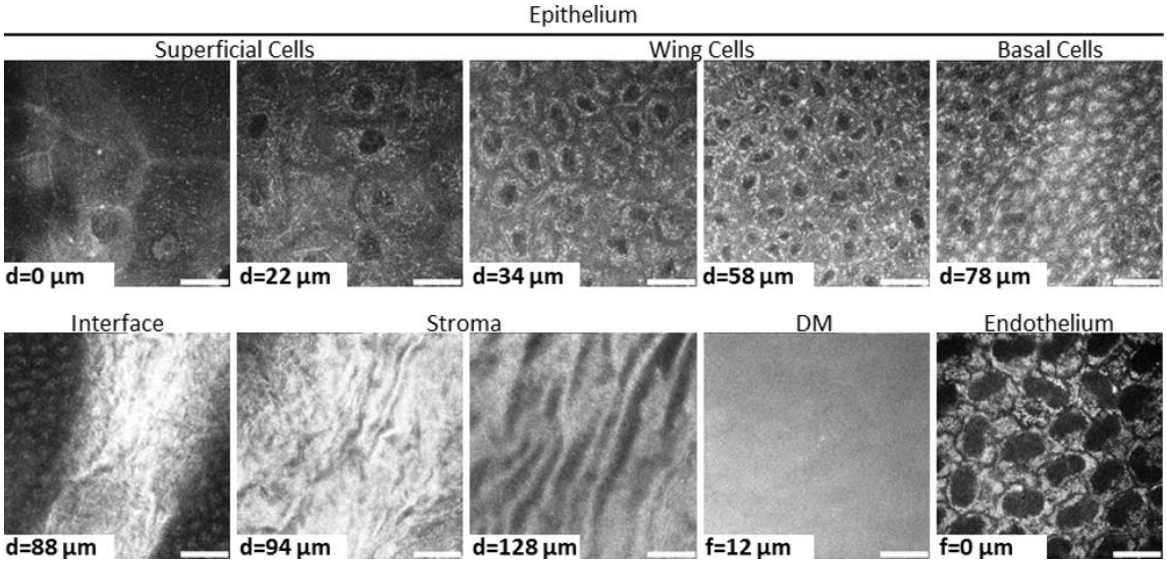


Figure 7.2.1 Autofluorescence intensity and second-harmonic generation images of the porcine cornea at multiple depths. Imaging depth is indicated. The distance measured from the epithelial surface is represented as $d$, whereas the distance $f$ is measured relative to the endothelial surface. DM – Descemet's membrane. Images acquired using the 5D microscope. Scale bar = 20 $\mu m$. Data published in [210].

The feasibility to image the entire cornea in a single acquisition in the intact eye was also demonstrated. For that purpose, an objective with a longer working distance (1.7 $mm$) was used. A 3D composite representation of the entire cornea, reconstructed from sequential AF intensity (green) and SHG (red) images acquired in a single session with 5 $\mu m$ interval between images, is shown in Figure 7.2.2A. A cross-section composite image of the tissue (Figure 7.2.2B) and its corresponding AF lifetime image (Figure 7.2.2C) are also shown. Images were acquired using the MPT*flex*. In the figure all corneal layers can be distinguished and the corneal thickness, as well as the thickness of each individual corneal layer, can be directly determined. Corneal thicknesses between 780 and 980 $\mu m$ were measured for the entire porcine cornea. The ranges of thicknesses obtained for each corneal layer are shown in Table 7.2.1. Values were obtained with margins of error between 2 and 5 $\mu m$.

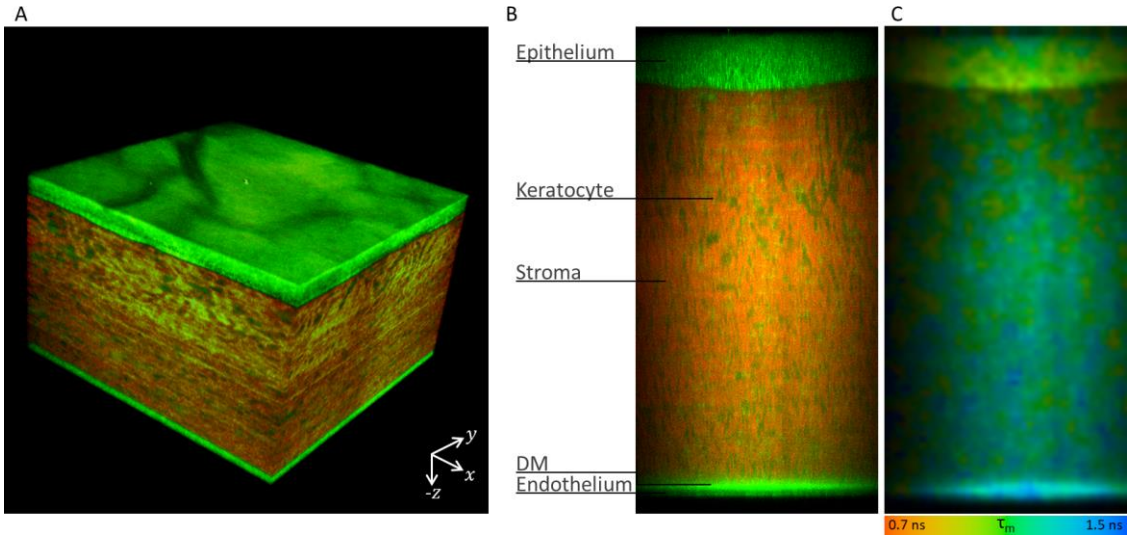


Figure 7.2.2 3D composite representation of the porcine cornea with 210 × 210 × 780 $\mu m^3$ reconstructed from autofluorescence (green) and second-harmonic generation (red) images of the tissue (A). Cross-sectional composite image of the sample representing an area of 450 × 900 $\mu m^2$ in which all layers of the tissue can be discriminated (B) and its corresponding autofluorescence lifetime image (C). Data obtained using the MPT*flex*.

Table 7.2.1 Thickness of the porcine corneal layers (as min – max) measured from two-photon images.

| **Corneal Layer** | **Thickness [$\mu m$]** |
|---|---|
| **Epithelium** | 70 – 80 |
| **Stroma** | 665 – 870 |
| **DM** | 6 – 10 |
| **Endothelium** | 6 – 8 |

### 7.2.2 Porcine cornea AF lifetime and metabolism

In addition to the morphological evaluation, using TPI, each corneal layer was characterized based on its AF lifetime. Figure 7.2.3 shows AF intensity and corresponding AF lifetime images of the epithelium, stroma, DM, and endothelium.

All cell types of the epithelium and endothelium have similar AF lifetime values (Figure 7.2.3). In the stroma, keratocytes with dendritic/stellate shapes can be easily recognized by their brighter AF intensity and longer AF lifetimes. Keratocytes are indicated by arrows (Figure 7.2.3). In the DM, all pixels of the image have similar AF lifetime (Figure 7.2.3).

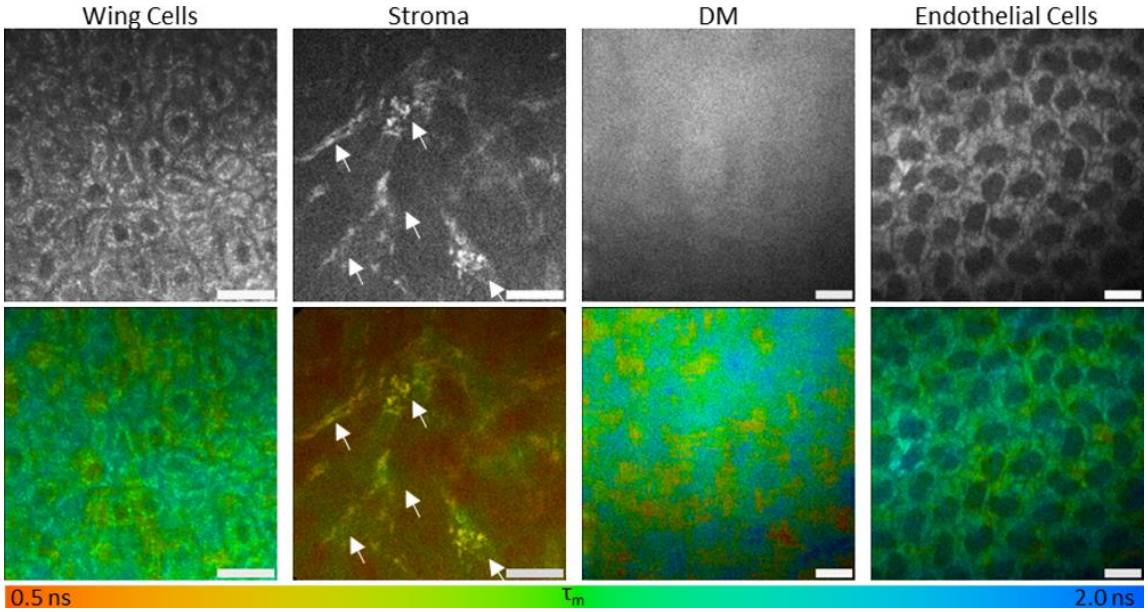


Figure 7.2.3 Autofluorescence (AF) intensity (top row) and corresponding AF lifetime images (bottom row) of all layers of the porcine cornea. AF lifetime images are color-coded for mean AF lifetime, as indicated in the color bar. Keratocytes in dendritic/stellate shape are indicated by arrows. Images acquired using the 5D microscope. Scale bar = 20 $\mu m$. Data published in [210].

The average AF lifetimes obtained for each corneal layer are shown in Table 7.2.2. For the analysis of the corneal epithelium, all cell types (superficial, wing, and basal cells) were considered. Keratocytes AF lifetime was assessed in manually defined ROIs containing these cells.

Table 7.2.2 Porcine corneal layers' autofluorescence lifetimes and relative contributions. Values are shown as average ± SD.

| Corneal Layer | $\tau_1$ $[ns]$ | $\tau_2$ $[ns]$ | $\tau_m$ $[ns]$ | $a_1$ [%] | $a_2$ [%] |
|---|---|---|---|---|---|
| **Epithelium** | 0.45±0.08 | 2.44±0.13 | 1.30±0.18 | 57.4±5.8 | 42.6±5.8 |
| **Stroma collagen** | 0.21±0.04 | 2.26±0.22 | 0.68±0.10 | 76.8±3.8 | 23.2±3.8 |
| **Keratocytes** | 0.31±0.06 | 2.23±0.16 | 0.88±0.08 | 70.4±3.6 | 29.7±3.6 |
| **DM** | 0.35±0.04 | 2.47±0.19 | 1.35±0.11 | 52.2±6.6 | 47.8±6.6 |
| **Endothelium** | 0.53±0.06 | 2.39±0.16 | 1.40±0.10 | 52.6±5.2 | 47.4±5.2 |

The ratio between the free ($a_1$) and protein-bound ($a_2$) components of NAD(P)H ($a_1/a_2$) was used to assess the metabolic state of different cells in the cornea. The ratios calculated for the entire epithelium, keratocytes, and endothelium are shown in Figure

7.2.4. The lowest NAD(P)H $a_1/a_2$ ratio was observed for the endothelial cells. In epithelial cells and keratocytes, the NAD(P)H $a_1/a_2$ ratio was significantly higher than in the endothelium ($\rho < 0.05$ and $\rho < 0.0001$, respectively). The keratocytes NAD(P)H $a_1/a_2$ ratio was also significantly higher than that observed for the epithelium ($\rho < 0.0001$).

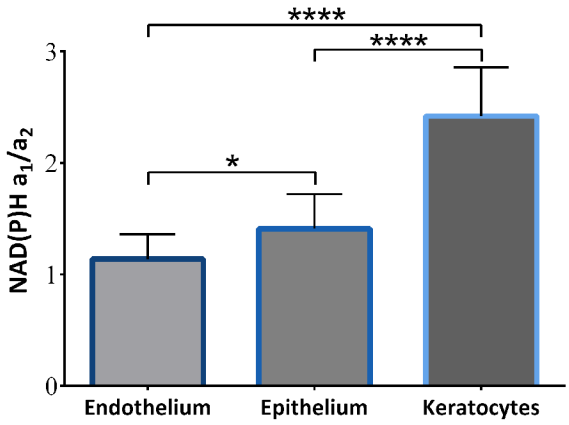


Figure 7.2.4 Free ($a_1$) to protein-bound ($a_2$) NAD(P)H ratio of the endothelium, epithelium, and stroma keratocytes. Date is presented as average + SD. Statistical significance determined using *t-test*: * $\rho < 0.05$; **** $\rho < 0.0001$.

## Depth-resolved metabolism of epithelial cells

The metabolic state of different cells of the epithelial layer was analyzed using the AF of NAD(P)H. Figure 7.2.5 shows AF intensity and corresponding AF lifetime images for different corneal depths color-coded according to the NAD(P)H mean AF lifetime for different corneal depths. The average variations in the NAD(P)H AF lifetimes and $a_1/a_2$ ratios with depth are also shown. A decline in the mean AF lifetime was observed with depth (Figure 7.2.5A and B). Moreover, basal cells have a higher NAD(P)H $a_1/a_2$ ratio than superficial cells (Figure 7.2.5C).

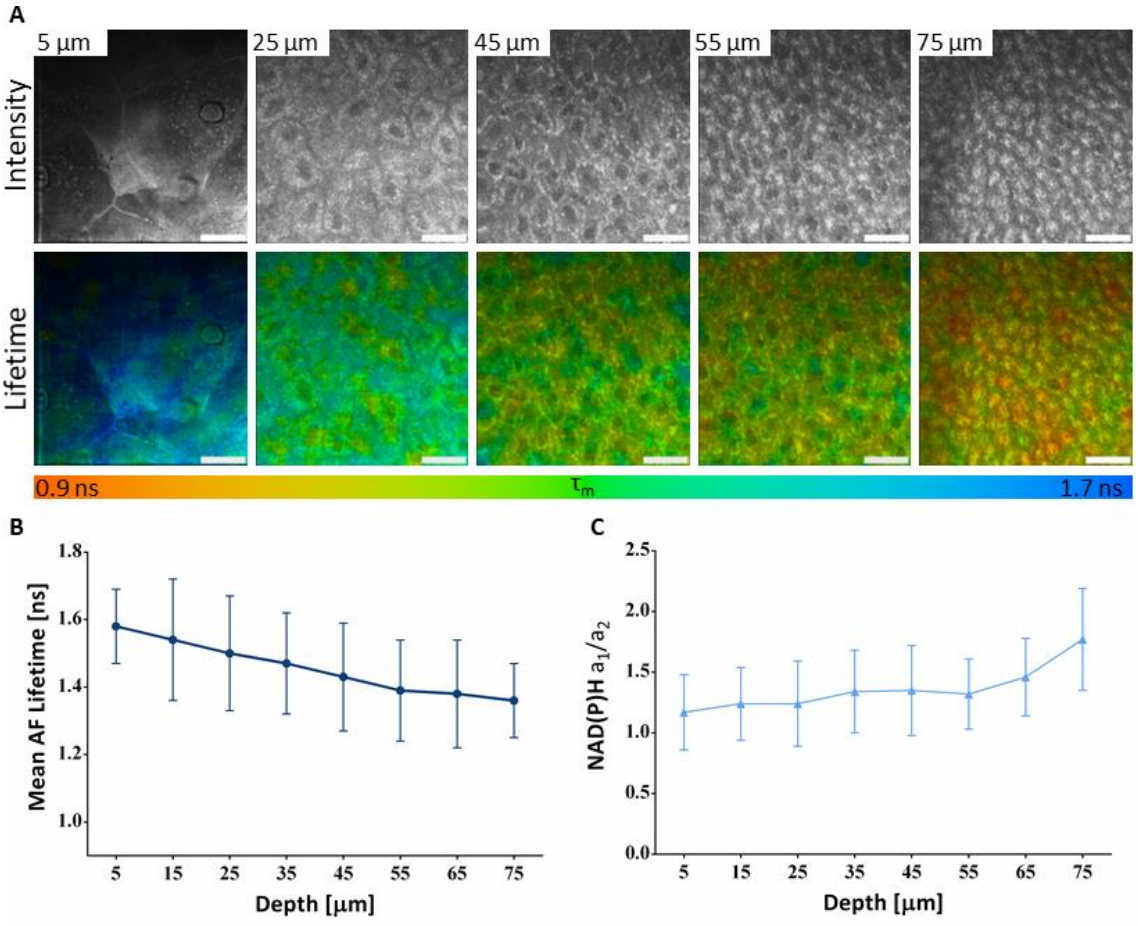


Figure 7.2.5 Autofluorescence (AF) intensity and corresponding NAD(P)H AF lifetime images of the corneal epithelial layer at multiple depths (A). Color ranges are as indicated in the color bar. Scale bar = 20 $\mu m$. Depth-resolved mean AF lifetime (B) and NAD(P)H free ($a_1$) to protein-bound ($a_2$) ratio (C), shown as average ± SD. Images obtained using the 5D microscope. Data published in [210].

### 7.2.3 Structural organization of the porcine corneal stroma

To evaluate the structural organization of the corneal stroma, SHG images were acquired in both forward and backward directions. Representative images of each and generated $xz$ and $yz$ projections are shown in Figure 7.2.6A and B, respectively. Figure 7.2.6C and D show 3D representations of the cornea stroma representing volumes of approximately $153 \times 153 \times 40\ \mu m^3$ reconstructed from individual SHG images acquired with 2 $\mu m$ steps between them in the backward and forward directions, respectively.

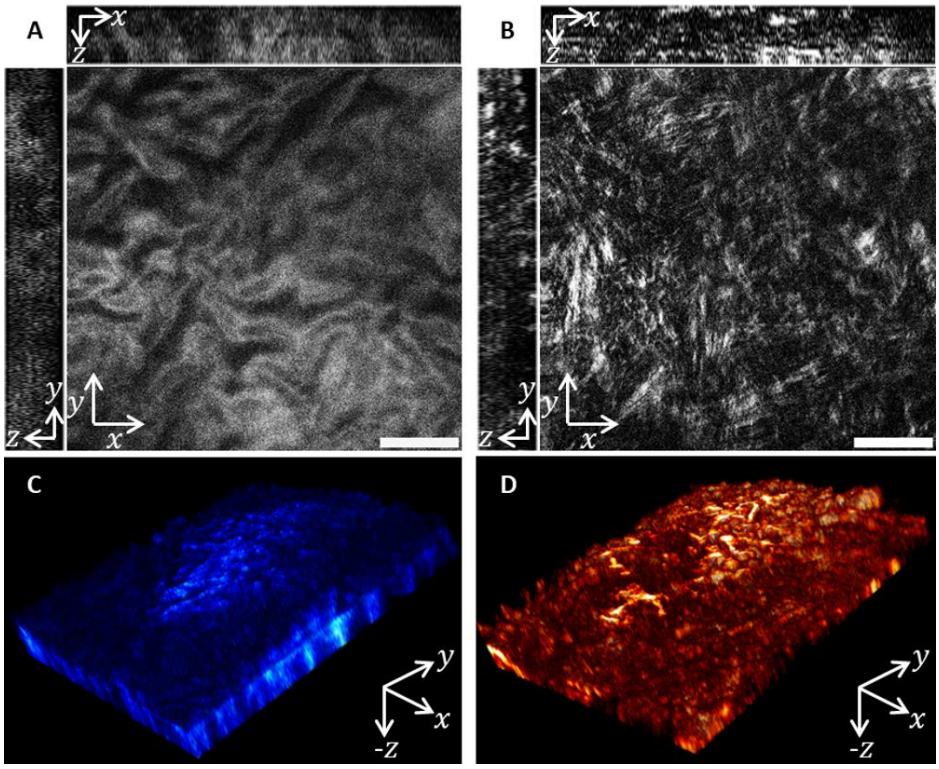


Figure 7.2.6 Second-harmonic generation (SHG) images and $xz/yz$ projections of the porcine corneal stroma recorded in the backward (A) and forward directions (B). 3D representations with approximately $153 \times 153 \times 40\ \mu m^3$ reconstructed from SHG images acquired in the backward (C) and forward directions (D) are also shown. Images acquired using the 5D microscope. Scale bar = 30 $\mu m$. Data published in [210].

In backward detected images, individual collagen fibers cannot be resolved. Thus, the images typically have diffused and speckle-like signals (Figure 7.2.6A). In forward direction collagen fibers can be discriminated and their orientation easily assessed. The feasibility of retrieve the organization of collagen fibers using both backward and forward detected images was assessed using the PP value obtained from FFT analysis (section 6.2.2). Prior to the application of the algorithm, images were divided into equally sized domains with $200 \times 200$ pixels corresponding to areas of $30 \times 30\ \mu m^2$. The distribution of PP values obtained from SHG images of the same regions of the stroma acquired in both directions are shown in Figure 7.2.7. As shown in the figure, backward detected images yield lower PP values. These images have more artifacts, which leads to lower orientation coherence and consequently lower PP values. Nevertheless, these artifacts are distributed uniformly, and the histogram patterns for both imaging configurations are very similar.

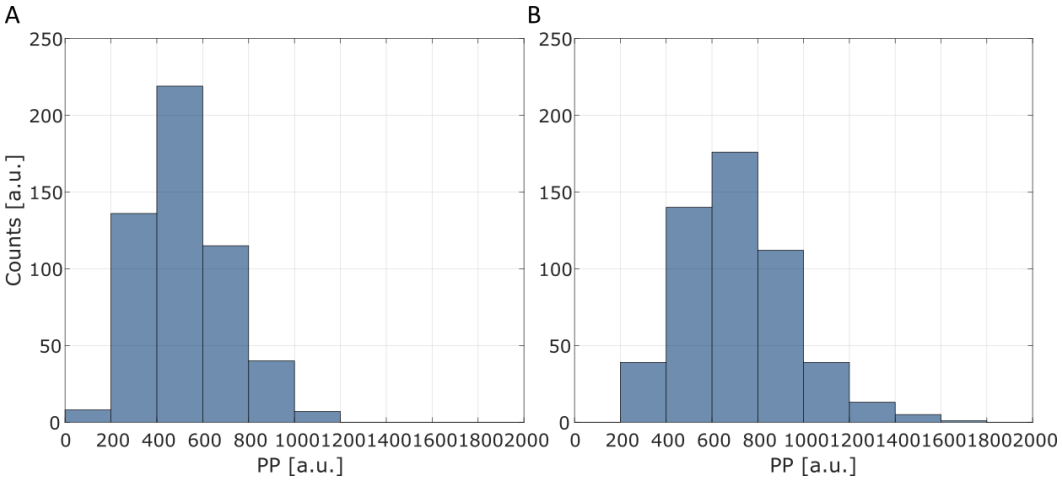


Figure 7.2.7 Histogram distributions of peak prominence (PP) values obtained from SHG images acquired in backward (A) and forward (B) directions.

## 7.3 IMAGING AND EVALUATION OF HUMAN CORNEAL DONOR BUTTONS

Evaluation of *ex vivo* human corneal donor buttons is essential in cornea banks and ensures the best chance of selecting healthy and viable samples for a positive transplantation outcome. Currently, the assessment of donor corneal tissue is mostly limited to morphological analysis of the tissue. An improvement in the evaluation of donor corneal buttons using TPI could lead to a better assessment of tissue suitability prior to transplant decreasing the number of graft rejection. Moreover, it could be used to optimize storage conditions and potentially increase the number of usable samples.

In this section, I demonstrate the advantages of using TPI to characterize human corneas and to assess suitable donor corneas prior to transplantation based on corneal cells morphology, metabolism, and stromal structural organization. AF and SHG signals from donor corneas with different storage times were characterized. Metabolic alterations induced by storage were assessed using the NAD(P)H $a_1/a_2$ ratios. The organization of the corneal stroma was evaluated based on GLCM and FFT analysis of SHG images. The results presented in this section were published in Batista *et al*., "*Assessment of human corneas prior to transplantation using high-resolution two-photon imaging*" Investigative Ophthalmology & Visual Science 59(1), 176-184, 2018 [212].

### 7.3.1 Corneal morphology and storage-induced alterations

The morphological characteristics of human corneas were evaluated at multiple depths using TPI. Moreover, the capacity to assess alterations induced by storage time to the endothelial cells morphology and layer thicknesses was demonstrated. Figure 7.3.1A shows a cross-section of the human cornea (A) as well as *en-face* AF intensity (red) and SHG (green) composite images of the corneal epithelium, BL, stroma, DM, and endothelium (B). In the epithelial and endothelial layers, single cells are visible. Thus, different cell types can be discriminated based on their anatomy. AF and SHG signals were

simultaneously detected at the BM and stroma. Single keratocytes (indicated by arrows) are visible in the corneal stroma. In the DM a strong AF signal was detected (Figure 7.3.1B).

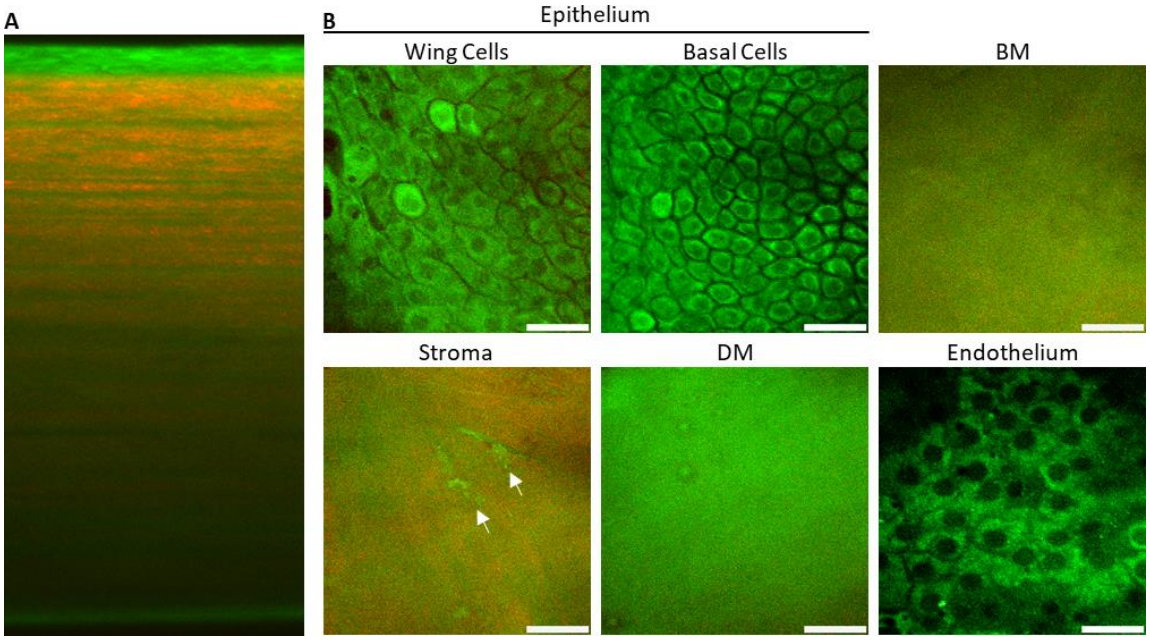


Figure 7.3.1 Human cornea cross-sectional autofluorescence intensity (green) and second-harmonic generation (red) composite image corresponding to an area of 50 × 1000 $\mu m^2$ (A) and *en-face* AF intensity and SHG composite images of the epithelium, Bowman's layer (BL), stroma, Descemet's membrane (DM), and endothelium (B). Stromal keratocytes are indicated by arrows. Images acquired using the MPT*flex*. Scale bars = 30 $\mu m$.

TPI enabled the assessment of corneal endothelial cells average shape, size, and density (Figure 7.3.2A). The lack of AF in the cellular membranes was taken as an advantage to manually highlight the contours of individual cells (Figure 7.3.2B) and segment them (Figure 7.3.2C). For STS corneas, endothelial cells were polyhedrons with (6 ± 1) sides and lengths of (19 ± 6) $\mu m$. The ECD computed based on the number of cells in the field-of-view was found to be (2037 ± 500) $cells/mm^2$. Cells were counted using stereological methods. In MTS samples, cells were enlarged and the ECD was lower. MTS endothelial cells had (7 ± 1) sides with lengths of (39 ± 6.1) $\mu m$. The ECD was found to be (1461 ± 190) $cells/mm^2$.

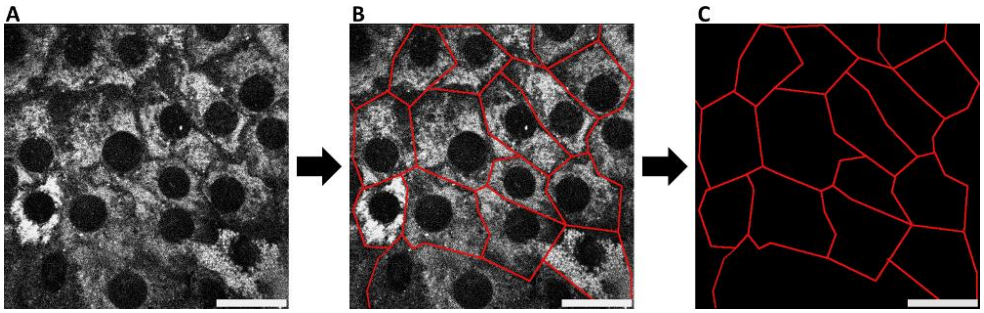


Figure 7.3.2 Endothelial cell segmentation on two-photon images: using the lack of AF at the cell membrane (A), endothelial cell contours can be traced (B) to generate a segmentation of the endothelial layer (C). Images acquired using the 5D microscope. Scale bar = 30 $\mu m$. Data published in [212].

Alterations in the thickness of different corneal layers during storage were also assessed (Table 7.3.1). A decrease in the epithelial layer thickness was observed for MTS corneas when compared to STS samples (Table 7.3.1). This thickness further decreased for LTS samples to values between 6 and 15 $\mu m$.

Table 7.3.1 Variations in the thicknesses of human corneal layers with storage. Values are shown as min – max. BL – Bowman's layer; DM – Descemet's membrane.

| *Corneal Layer* | *Epithelium* | *BL* | *DM* | *Endothelium* |
|---|---|---|---|---|
| **STS corneas [$\mu m$]** | 40 – 55 | 5 – 10 | 10 – 16 | 6 – 10 |
| **MTS corneas [$\mu m$]** | 12 – 39 | 6 – 18 | 8 – 11 | 5 – 6 |

### 7.3.2 Corneal AF lifetime and storage-induced metabolic changes

The average AF lifetimes of each layer of the human cornea and their relative contributions are shown in Table 7.3.2. For the analysis of the corneal epithelium, all cell types were considered. In the corneal stroma, both collagen and keratocytes are sources of AF. Due to the spectral overlap of their endogenous AF, separate analysis of keratocytes AF was only possible by selecting ROIs. Representative AF lifetime images of the epithelium, stroma, and endothelium, color-coded for the mean AF lifetime, are shown in Figure 7.3.3.

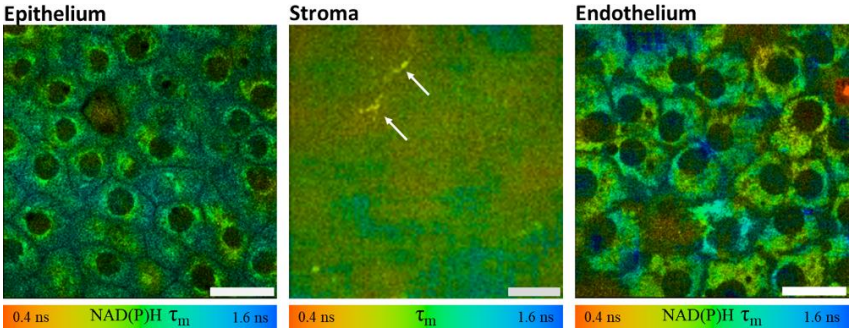


Figure 7.3.3 Autofluorescence lifetime images of the human cornea epithelium (A), stroma (B), and endothelium (C) color-coded for the mean AF lifetime as indicated in the color bars. In the corneal stroma, arrows point to keratocytes. Scale bar = 30 $\mu m$. Data published in [212].

Table 7.3.2 Autofluorescence lifetimes and relative contributions of all layers of human corneas with short-term storage. Values are represented as average ± SD.

| Corneal Layer | $\tau_1$ $[ns]$ | $\tau_2$ $[ns]$ | $\tau_m$ $[ns]$ | $a_1$ [%] | $a_2$ [%] |
|---|---|---|---|---|---|
| **Epithelium** | 0.41±0.09 | 1.83±0.15 | 1.83±0.15 | 52.6±2.7 | 47.4±2.7 |
| **BL** | 0.37±0.09 | 2.07±0.20 | 1.27±0.13 | 47.0±5.5 | 53.0±5.5 |
| **Stroma collagen** | 0.24±0.07 | 2.10±0.10 | 1.04±0.20 | 57.0±8.7 | 43.0±8.7 |
| **Keratocytes** | 0.16±0.02 | 2.03±0.07 | 0.65±0.01 | 73.8±1.3 | 26.2±1.3 |
| **DM** | 0.28±0.05 | 2.11±0.04 | 1.15±0.09 | 52.2±3.2 | 47.8±3.2 |
| **Endothelium** | 0.31±0.06 | 1.76±0.13 | 0.97±0.05 | 54.4±1.9 | 45.6±1.9 |

The effect of storage duration on the metabolic activity of different cell types was evaluated based on the NAD(P)H $a_1/a_2$ ratio. Images of epithelial and endothelial cells, with different storage times, color-coded for NAD(P)H $a_1/a_2$ ratio, as well as the average alterations of NAD(P)H $a_1/a_2$ for each cell type, are shown in Figure 7.3.4. For epithelial cells, the NAD(P)H $a_1/a_2$ ratio was significantly higher for LTS and MTS corneas than for STS corneas ($\rho < 0.0001$ and $\rho < 0.05$, respectively). A significant increase from MTS to LTS ($\rho < 0.0001$) was also observed (Figure 7.3.4A and C). In the endothelium, the NAD(P)H $a_1/a_2$ ratio significantly increased ($\rho < 0.05$) with storage time (Figure 7.3.4B and D). No information could be obtained on the endothelial layer of LTS corneas due to the very low number of cells. For stromal keratocytes, NAD(P)H $a_1/a_2$ ratio was significantly lower for LTS corneas when compared to STS ($\rho < 0.0001$) and MTS samples ($\rho < 0.0001$). No

differences were observed in the NAD(P)H $a_1/a_2$ ratio of keratocytes between STS and MTS corneas (Figure 7.3.4E).

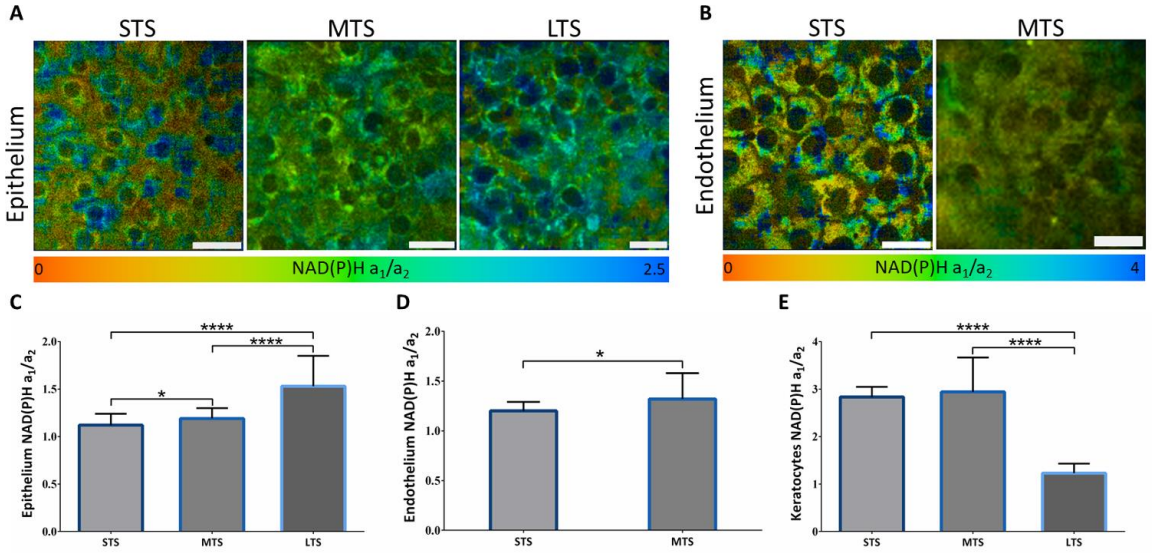


Figure 7.3.4 Autofluorescence lifetime images of the human corneal epithelial (A) and endothelial (B) cells with short- (STS), medium- (MTS), and long-term storage (LTS) times color-coded for the NAD(P)H free to protein-bound ($a_1/a_2$) ratio as indicated in the color bars. Scale bar = 30 $\mu m$. Average + SD NAD(P)H $a_1/a_2$ ratio for epithelial cells (C), endothelial cells (D), and keratocytes (E). Statistical differences assessed using the non-parametric *Mann-Whitney U test*. * $p < 0.05$; **** $p < 0.0001$. Images acquired using the 5D microscope and published in [212].

### 7.3.3 Alterations in the stromal organization during storage

SHG images were used to characterize the organization of collagen fibers in the BL and stroma and to assess alterations induced by storage time. Backward detected SHG images of the BL and the stroma at multiple depths, as well as a 3D representation of the human cornea stroma, rendered from sequential SHG images, acquired with 5 $\mu m$ depth intervals, are shown in Figure 7.3.5A and B, respectively.

The geometrical arrangement of collagen was evaluated through the correlation between neighboring pixels as a function of distance using GLCM (section 6.2.2). The correlation was analyzed along the vertical, horizontal, and diagonal image directions with distances ranging from 1 to 16 $\mu m$. The curves obtained for the BL and stroma of STS corneas and for the stroma of MTS and LTS corneas are shown in Figure 7.3.5C. In the BL of STS corneas, a slow linear decrease in correlation between neighbor pixels with distance was observed for all directions, whereas for the stroma of the same samples, a fast-logarithmic decrease

was observed. For MTS and LTS corneas, a progressively slower decrease in correlation between neighbor pixels with depth was observed compared to STS samples (Figure 7.3.5C).

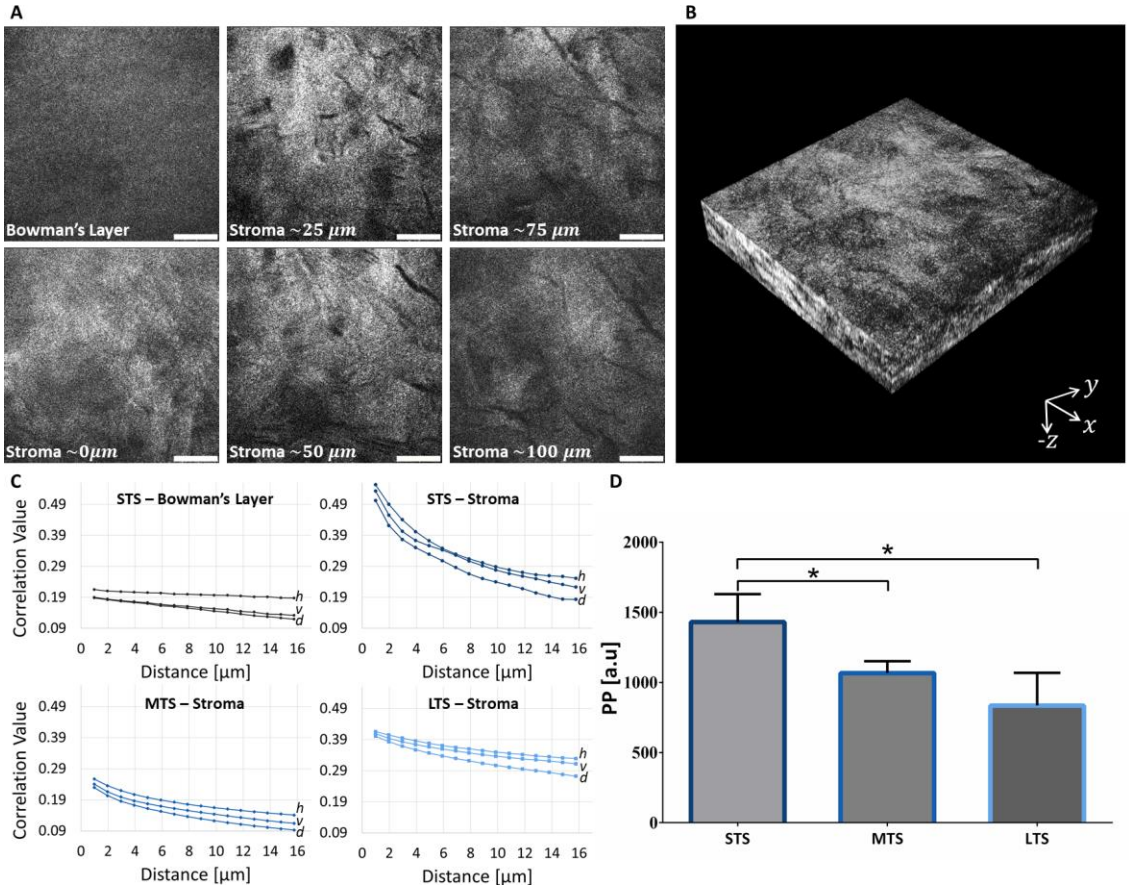


Figure 7.3.5 Backward detected second-harmonic generation images of the human cornea Bowman's layer and the stroma 0, 25, 50, 75, and 100 $\mu m$ deep (A). 3D representation of the tissue corresponding to a total volume of 150 × 150 × 100 $\mu m^3$ rendered form SHG images (B). Images acquired with the 5D microscope. Scale bar = 30 $\mu m$. Correlation as a function of distance in the horizontal (*h*), vertical (*v*), and diagonal (*d*) directions (C). Average + SD peak prominence (PP) of the main orientation (D). The *Mann-Whitney U test* was used for statistical analysis. * $p < 0.05$. Data published in [212].

Alterations to the collagen fibers' organization over time were evaluated by FFT analysis of SHG images using the above-defined variable PP (section 6.2.2). Before applying the algorithm, images were equally divided into smaller domains with 400 × 400 pixels, corresponding to 80 × 80 $\mu m^2$. The PP values obtained for STS, MTS, and LTS corneas are shown in Figure 7.3.5D. For MTS and LTS corneas, PP was significantly lower than that observed for STS samples ($\rho < 0.05$).

## 7.4 TPI OF DISEASED HUMAN CORNEAS

The differential diagnosis of corneal pathologies is one of the possible clinical application of TPI. It could lead to an improved diagnosis of pathologies and a better understanding of the underlying pathophysiological mechanisms. Therefore, in this section, the feasibility of TPI to discriminate between non-pathological (NP) and pathological human corneas based on the tissue AF intensity, lifetime, and SHG is reported. Three pathologies were considered in this proof of principle analysis:

- **Keratoconus (KC)** – a corneal ectatic disorder, *i.e.,* a noninflammatory disorder that affects the corneal shape, usually characterized by the progressive thinning and stepping of the cornea finally leading to the formation of a cone [213, 214].
- ***Acanthamoeba* keratitis (AK)** – results from the contamination with the free-living organism *amoeba* and it causes corneal ulceration and necrosis at the epithelial and stromal levels [215–217].
- **Stromal corneal scars (SCS)** – typically formed during abnormal corneal wound healing due to injury, infections, or even refractive surgery that can lead to the opacification of the cornea, reducing the visual acuity [218].

In this section, the morphology of the tissue, obtained by detecting its AF intensity, was used to visualize the morphological alterations reported for each pathology. In addition, the AF lifetime of NAD(P)H was used to further characterize the tissue and to evaluate the metabolic activity of the epithelial cells. SHG images of the corneal stroma were used to assess alterations caused by the pathologies to the structural organization of this layer. The results presented here were published in Batista *et al*. "High-resolution, label-free two-photon imaging of diseased human corneas" Journal of Biomedical Optics 23(3), 036002:1-8, 2018 [219].

### 7.4.1 Pathological changes in the corneal epithelium

Based on the AF intensity, morphological changes caused by the different pathologies in epithelial superficial, wing, and basal cells were observed (Figure 7.4.1). In NP corneas,

cells within each sub-layer had a regular size and shape. This was not the case for pathological conditions. For KC, an enlargement and elongation of cells were observed. In the epithelial cells of the AK cornea, abnormal AF signals were detected from the cell membrane (Figure 7.4.1). Additionally, some areas of the epithelium lack basal cells (Figure 7.4.1, red arrows). In SCS, basal cells were enlarged compared with the corresponding cells of NP corneas. Spots with bright AF were also detected throughout the epithelial layer, possibly due to the deposition of debris (Figure 7.4.1, white arrows).

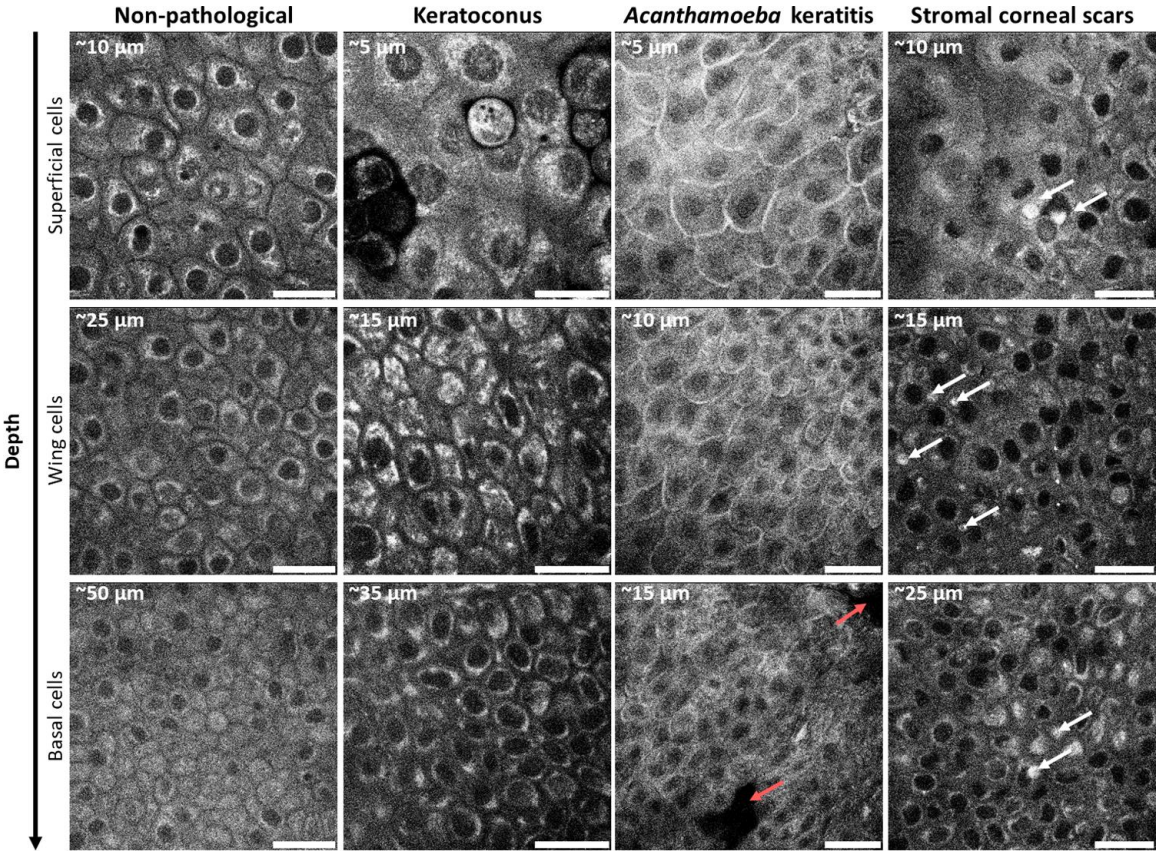


Figure 7.4.1 Autofluorescence intensity images of the corneal epithelium of non-pathological, keratoconus, *Acanthamoeba* keratitis, and stromal corneal scars samples. For each condition, superficial, wing, and basal cells and their respective depths are shown. Red arrows point to regions without basal cells in *Acanthamoeba* keratitis corneas, whereas white arrows indicate debris in stromal corneal scars. Scale bar = 30 $\mu m$. Data published in [219].

Corneal epithelial thickness was altered for every pathology. For NP corneas, the measured epithelium thickness was approximately (48 ± 6) $\mu m$. In KC, AK, and SCS corneas this value decreased to (31 ± 9) $\mu m$, (25 ± 5) $\mu m$, and (30 ± 4) $\mu m$, respectively.

Using the epithelium AF lifetime, pathology-induced alterations were further highlighted. Figure 7.4.2 shows AF lifetime images and lifetime distributions of the entire fields-of-

view, single cells, and anomalies of each pathology. As shown, in NP corneas all cells have similar mean AF lifetimes. In KC, AK, and SCS conditions, the epithelium exhibits an heterogenous lifetime distribution (Figure 7.4.2). In KC corneas, longer AF lifetimes were observed for cells with altered/abnormal morphology than the surrounding cells (Figure 7.4.2). In the AK cornea, the abnormal cell membrane AF had a longer mean AF lifetime than the cell cytoplasm (Figure 7.4.2). In the SCS cornea, debris had a homogenous and short mean AF lifetime (Figure 7.4.2).

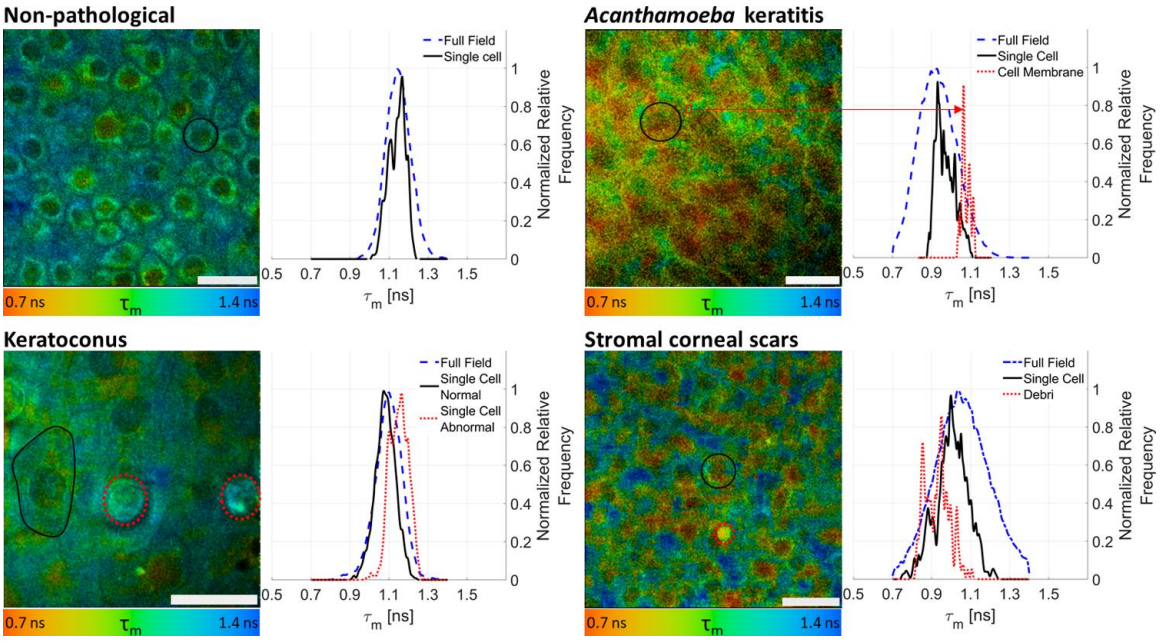


Figure 7.4.2 Autofluorescence (AF) lifetime images and distributions of non-pathological corneas and samples affected by keratoconus (KC), *Acanthamoeba* keratitis (AK), and stromal corneal scars (SCS). AF lifetime images are color-coded for the mean AF lifetime as indicated in the color bars. AF lifetime distributions for the entire field-of-view of each condition are represented as dashed blue lines. Full black lines show the AF distribution of regions of interest (ROIs) with single cells. ROIs of cells with altered/abnormal morphology, abnormal AF from cell membrane, and debris are shown in dotted red lines for KC, AK, and SCS, respectively. The boundaries of all the ROIs are traced in the respective AF lifetime images. The lines used to trace the ROIs (full black and dotted red) match the lines in the graphs. Scale bar = 30 $\mu m$. Data published in [219].

Induced metabolic alterations on epithelial cells were evaluated using NAD(P)H $a_1/a_2$ ratios (Figure 7.4.3). A significant increase in the NAD(P)H $a_1/a_2$ ratio was observed for KC corneas when compared to NP samples ($\rho < 0.0001$). A tendency for an increase was also observed for corneas affected by AK and SCS (Figure 7.4.3).

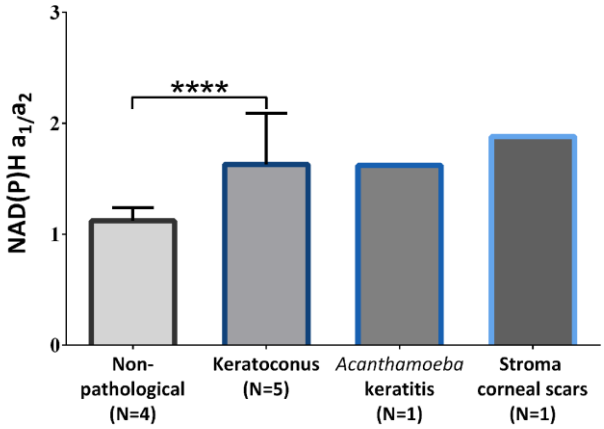


Figure 7.4.3 NAD(P)H free to protein-bound ($a_1/a_2$) ratios of the corneal epithelial cells for non-pathological and diseased corneas (average + SD). Statistical differences assessed with the non-parametric *Mann-Whitney U test*. **** $\rho < 0.0001$. Data published in [219].

### 7.4.2 Optical evaluation of pathological changes in the corneal stroma

In the SHG images of NP, KC, AK, and SCS corneas, qualitative differences were visible for all pathologies (Figure 7.4.4). Quantitative assessment of pathology-induced changes was performed by FFT analysis (Figure 7.4.5A). The PP value decreased significantly in KC corneas ($\rho < 0.01$). For AK and SCS corneas, a tendency for a decrease in PP was also observed (Figure 7.4.5A).

The feasibility to diagnose different pathologies based on the stroma AF lifetime was also evaluated (Figure 7.4.5B). KC corneas have significantly lower mean AF lifetime than NP corneas ($\rho < 0.0001$). A tendency for a decrease was also observed for AK. For SCS, the stroma mean AF lifetime shows a tendency to increase (Figure 7.4.5B).

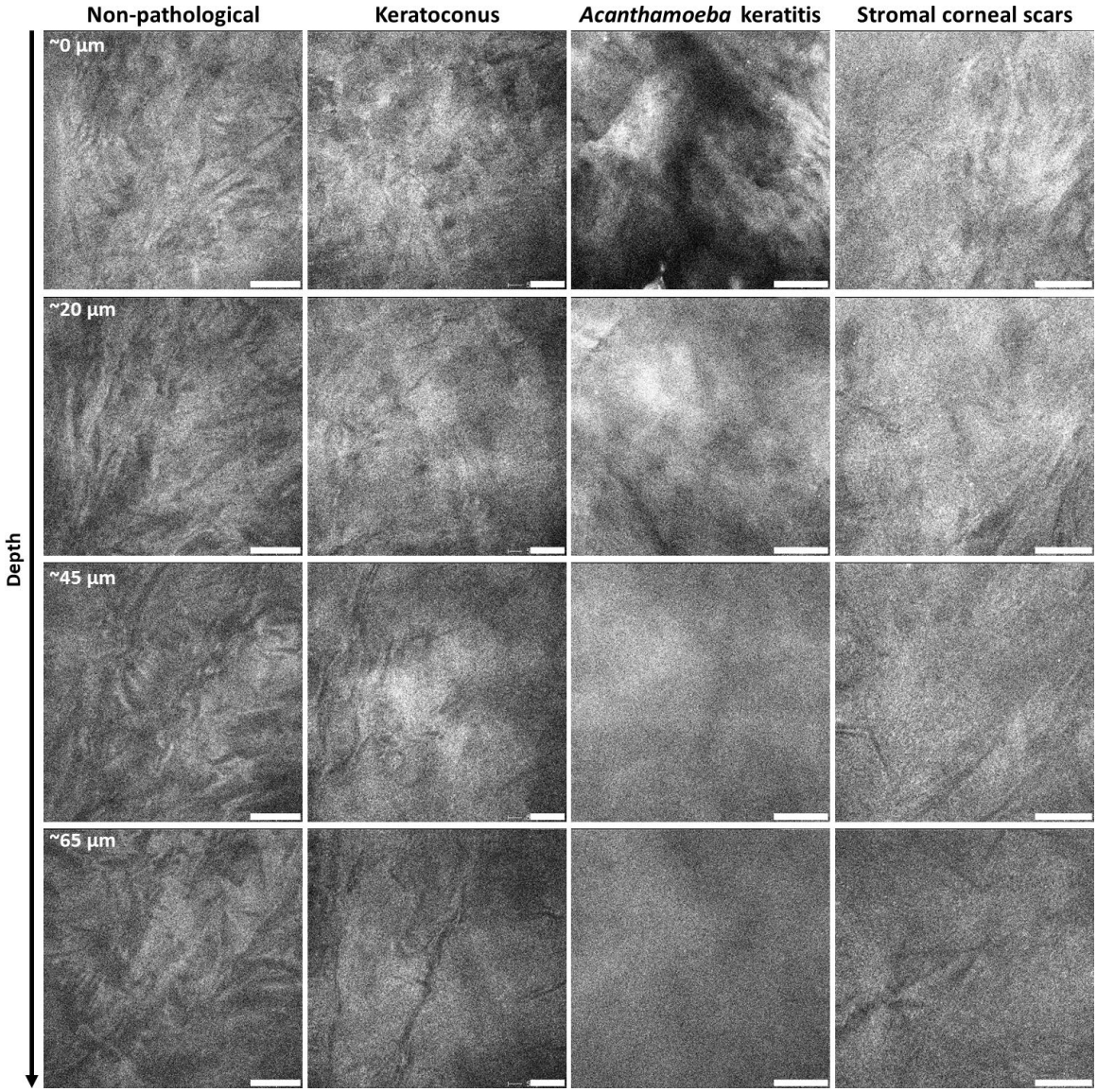


Figure 7.4.4 Depth-resolved second-harmonic generation images of non-pathological human corneas, and corneas diagnosed with keratoconus, *Acanthamoeba* keratitis, and stromal corneal scars. Scale bar = 30 $\mu m$. Data published in [219].

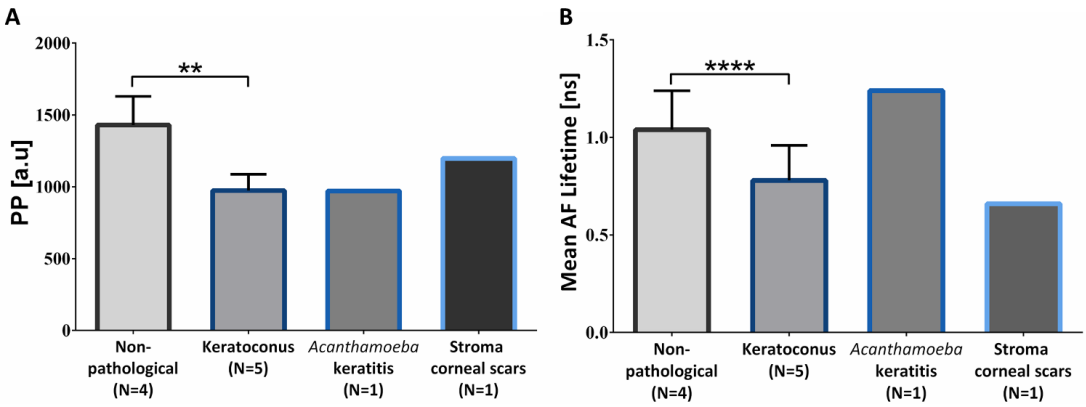


Figure 7.4.5 Peak prominence (PP) of the main orientation (A) and mean AF lifetimes of the stroma (B) for non-pathological and diseased corneas. Values presented as average + SD. The *Mann-Whitney U test* was used for statistical analysis. ** $p < 0.01$; **** $\rho < 0.0001$. Data published in [219].

## 7.5 Assessment of corneal collagen crosslinking in human corneas

Corneal collagen crosslinking (CXL) is a procedure used in clinical practice to treat ectatic disorders such as KC and ectasia secondary to laser refractive surgery by strengthening the mechanical stability of the cornea [193, 194]. Recently, the therapeutic effects of CXL in myopia progression, corneal edema, and infectious keratitis have also been demonstrated [192–194, 220]. The basis of CXL is the photodynamic reaction between ultraviolet A (UVA) light and riboflavin. From this, reactive oxygen species (ROS) are produced that induce the formation of new covalent crosslink bounds between collagen molecules and fibrils leading to tissue strengthening [193, 194]. Its feasibility to strengthen the corneal stroma was first demonstrated in 1997 by Spoerl *et al*. [221], and it was introduced to treat KC patients six years later [222]. In the past years, attempts to improve the treatment efficiency and patient comfort have been carried out. Namely, the duration of the procedure has been shortened by increasing the UVA exposure power. Accelerated CXL (ACXL) was first performed in 2011 by Schumacher *et al.* [223]. Since then, it has been demonstrated that it can achieve the same effect as the conventional protocol [209, 224, 225].

The safety and reliability in halting KC progression of CXL has been demonstrated in several clinical trials [51, 222, 225–228]. Nevertheless, cases of treatment failure also occur [229–231]. CXL failure rates up to 16.5% have been reported [230]. In the case of treatment failure, secondary CXL is usually considered [231]. Although being a minimally invasive procedure, current CXL treatments require cornea de-epithelialization. Due to the high density of nerve endings in this tissue, this leads to pain, burning sensation, and tearing discomfort for several days [193]. The clinical outcome of CXL/ACXL is typically observed for the first time several weeks after treatment. The evaluation of CXL/ACXL outcome sooner after treatment is important and can shed some light into treatment efficiency. In this section, the cornea AF was used to assess the outcome of ACXL. Data showed that using TPI, crosslinking can be evaluated noninvasively, label-free, and with fast acquisition times soon after treatment. Therefore, TPI could potentially become an

important tool in the follow-up and assessment of the clinical outcome of this and other medical procedures.

### 7.5.1 Riboflavin diffusion

The photosensitizer used for ACXL (riboflavin) has intrinsic fluorescence. The emission spectra of this fluorophore and of the cornea endogenous fluorophores are shown in Figure 7.5.1. Spectra were acquired with a thermoelectric-cooled CCD-array spectrometer (BTC112, B&W Tek, Newark, USA) and were corrected for its sensitivity and the spectral transmission efficiency of the optical path. As shown in the figure, riboflavin emission overlaps with NAD(P)H, flavins, and collagen emission. Therefore, the presence of riboflavin in the cornea influences the overall stroma AF intensity and lifetime. In this study, this influence was avoided by measuring the samples after the diffusion of the riboflavin out of the cornea. The diffusion process was monitored by TPI in a total of 4 human samples. TPI measurements were performed every 30 $min$ for a period of 120 $min$ (Figure 7.5.2).

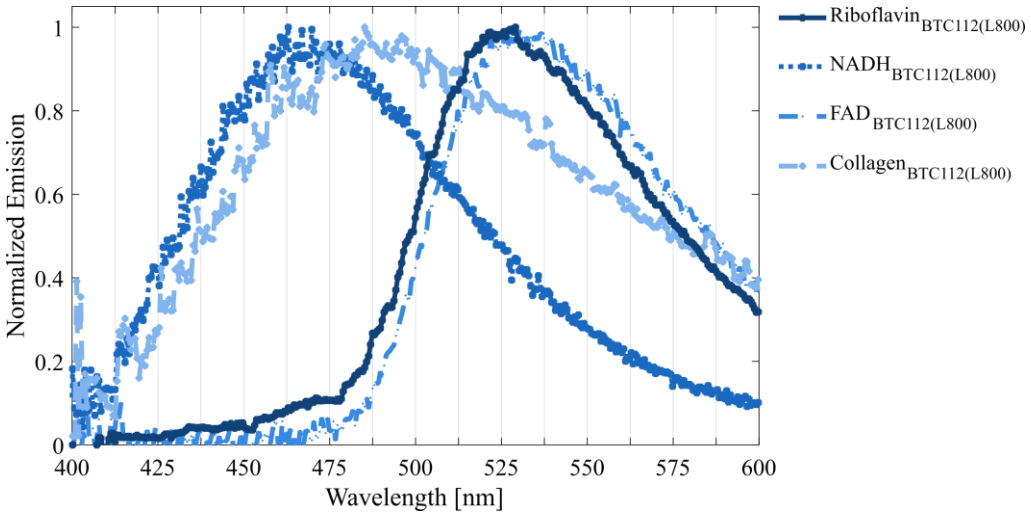


Figure 7.5.1 Fluorescence emission spectra of the pure solutions of 0.1 % riboflavin, NADH and FAD in Tris hydrochloride and of lyophilized collagen type I. The spectra were obtained with a spectrometer (BTC112). The fluorophores were excited using a 10 $fs$ broad bandwidth excitation laser centered at 800 $nm$ (L800).

Figure 7.5.3 shows cross-sectional images of the cornea before the application of riboflavin (baseline), immediately after applying the photosensitizer (0 $min$), and after 30,

60, 90, and 120 $min$. Average changes to mean AF lifetime and intensity variation ($\Delta I$) with time are also shown. $\Delta I$ was computed as:

$$\Delta I = I_t - I_B \qquad (7.1)$$

where $I_B$ and $I_t$ stand for the AF intensity, obtained from the total photon counts, at baseline and at the different measuring time points, respectively.

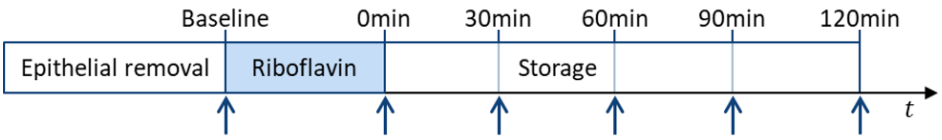


Figure 7.5.2 Schematic representation of the assessment of riboflavin diffusion out of the cornea. Vertical arrows represent time points of two-photon image acquisition.

Prior to riboflavin application the corneal stroma presented a bi-exponential AF decay with a mean AF lifetime of (1.24 ± 0.03) $ns$ (Figure 7.5.3A). Immediately after riboflavin application ($t$ = 0 $min$), the AF lifetime was significantly higher than that of the baseline measurement ($\rho$ < 0.05; Figure 7.5.3A and B). A single exponential decay with lifetime of (3.12 ± 0.06) $ns$ was measured (Figure 7.5.3B) which is in good agreement with the lifetime measured for the pure 0.1% solution of riboflavin ((3.37 ± 0.06) $ns$). A significant increase in $\Delta I$ was also observed ($\rho$ < 0.05). Approximately 150 000 more photon counts were detected in the cornea following the application of riboflavin (Figure 7.5.3C). After 30 $min$ storage, two distinct regions in the corneal stroma AF signal can be observed. Longer AF lifetimes were observed in the posterior stroma than the anterior stroma (Figure 7.5.3A). These regions are likely to contain different riboflavin concentrations. Both the AF lifetime and $\Delta I$ decreased significantly when compared to values obtained at $t$ = 0 $min$ ($\rho$ < 0.05) and the AF lifetime exhibited again a bi-exponential decay. However, the stroma average AF lifetime and $\Delta I$ values were still significantly higher than the baseline values ($\rho$ < 0.05; Figure 7.5.3B and C). Both parameters continued to decrease progressively after 60 and 90 $min$ storage ($\rho$ < 0.05; Figure 7.5.3B and C). The baseline AF lifetime and $\Delta I$ values were reached after 120 $min$ of storage (Figure 7.5.3B and C).

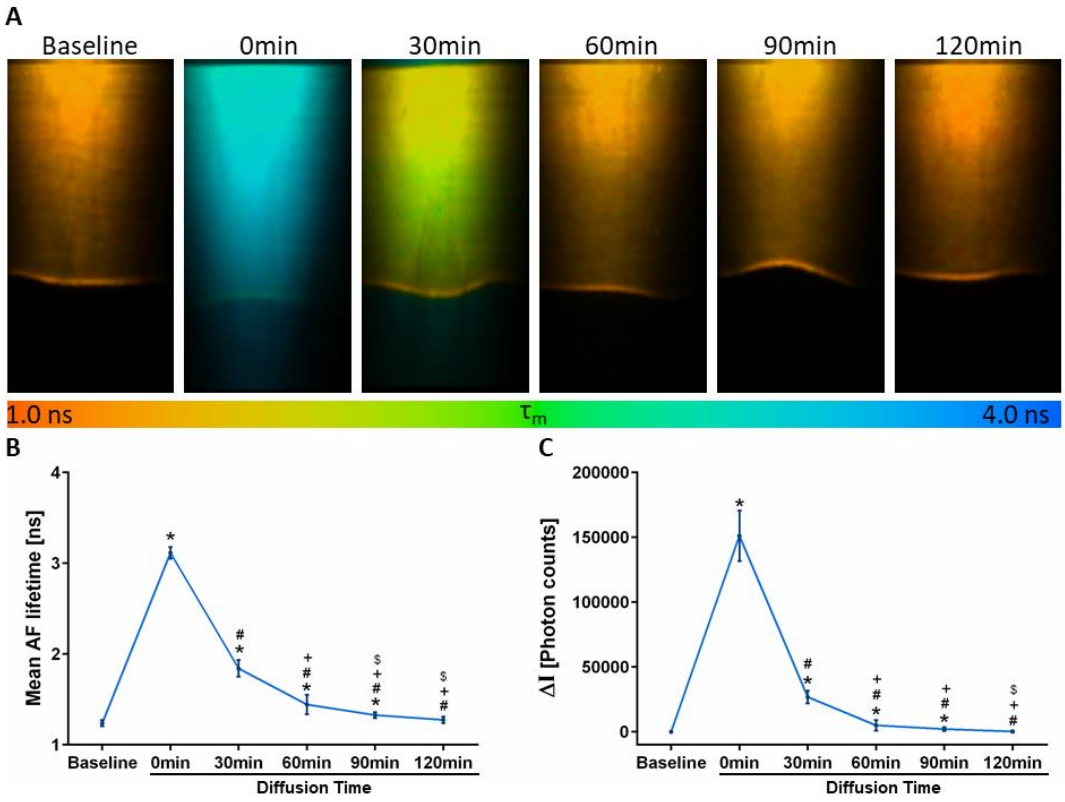


Figure 7.5.3 Cross-sectional autofluorescence (AF) lifetime images of the cornea during riboflavin diffusion (A). Average mean AF (B) and variation in AF intensity ($\Delta I$) over time (C). AF lifetime images are color-coded for the mean AF lifetime as indicated in the color bar. Statistical significance computed using *Mann-Whitney U test*. * ρ < 0.05 compared with baseline; $^{\#}$ ρ < 0.05 compared with $t$ = 0 $min$; $^{+}$ ρ < 0.05 compared with $t$ = 30 $min$; $^{\$}$ ρ < 0.05 compared with $t$ = 60 $min$.

### 7.5.2 ACXL-induced alterations to the corneal stroma AF

To assess the alterations induced by ACXL, the tissue AF intensity (Figure 7.5.4) and lifetime (Figure 7.5.5) were analyzed prior to treatment (baseline) and 2, 24, 72, and 144 $h$ later (Figure 6.3.2). At each time point, *en-face* images of two non-overlapping areas covering either 130 × 130 $\mu m^2$ or 300 × 300 $\mu m^2$ of the tissue were acquired using the MPT*flex*. The samples were images up to a depth of 300 $\mu m$, with 5 $\mu m$ steps in the $z$ direction between the images. Additionally, up to six cross-sections of the samples were obtained.

Figure 7.5.4A shows 3D representations of the human cornea AF intensity for control, RFN, and LED-ACXL at $t$ = 72 $h$, reconstructed from individual and sequential AF intensity images covering a volume of 300 × 300 × 300 $\mu m^3$. As shown in the figure, LED-ACXL

corneas have a higher AF intensity than the untreated samples (control) and samples treated only with riboflavin without UVA irradiation (RFN). The average variations in AF intensity from the baseline measurement to each time point ($\Delta I$) were calculated for all groups and are shown in Figure 7.5.4B. For control and RFN groups, no significant alterations were observed over time. For LED-ACXL corneas, the AF intensity increased significantly as soon as 2 $h$ after ACXL ($\rho$ < 0.01) and remained significantly higher than that of baseline in subsequent acquisitions ($\rho$ < 0.01).

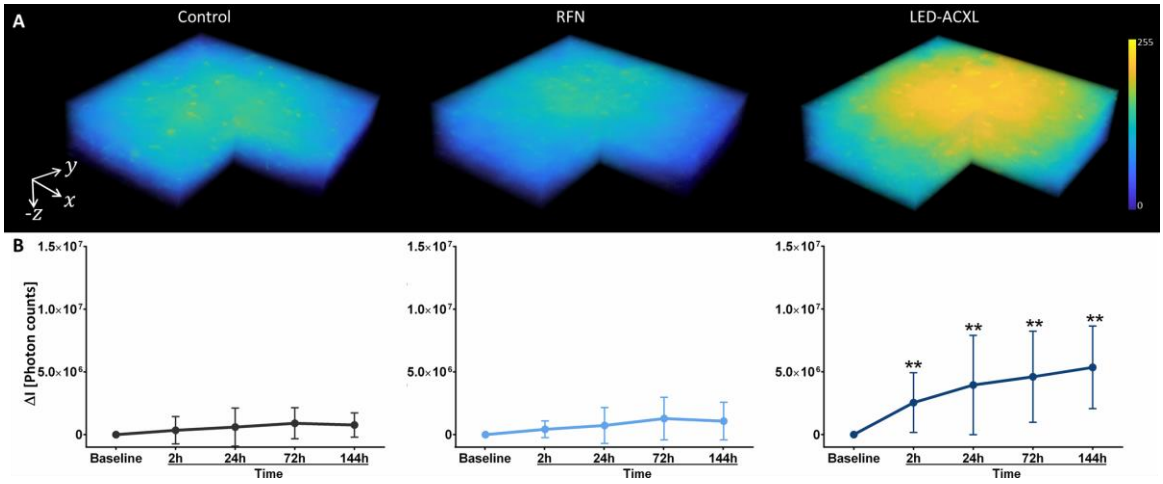


Figure 7.5.4 3D representations of the human cornea for control, RFN, and LED-ACXL conditions at $t$ = 72 $h$ (A). Volumes were rendered from *en-face* autofluorescence (AF) intensity images and cover 300 × 300 × 300 $\mu m^3$. Average variations in the AF intensity ($\Delta I$) for all groups over time (B). Statistical significance computed using *t-test*. ** ρ < 0.01.

Figure 7.5.5 shows representative cross-sectional AF lifetime images of control, RFN, and LED-ACXL corneas as well as the average variations in their mean AF lifetime over time. As shown, no significant alterations were observed in the control and RFN corneas (Figure 7.5.5B). In these groups, corneas show a uniform AF lifetime throughout the experiment (Figure 7.5.5A).

In LED-ACXL corneas, the stroma mean AF was significantly higher than that of the baseline measurement for all subsequent acquisitions (Figure 7.5.5B). Immediately after riboflavin diffusion out of the sample ($t$ = 2 $h$), a general increase in the mean AF lifetime was observed. After 24, 72, and 144 $h$, longer lifetimes were observed in the anterior portion of the stroma (Figure 7.5.5A).

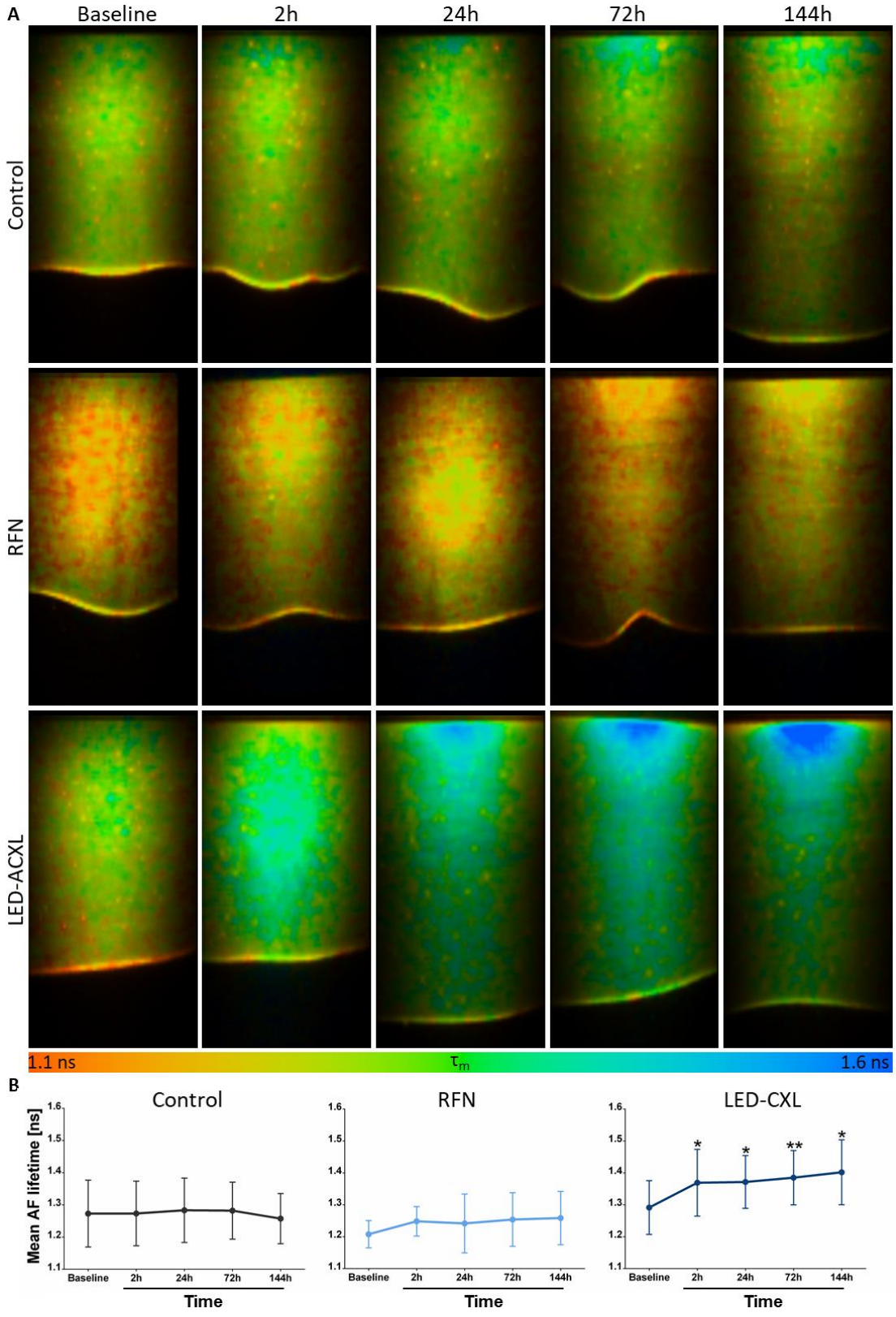


Figure 7.5.5 Cross-sectional autofluorescence (AF) lifetime images of the cornea at baseline and at 2, 24, 72, and 144 $h$ for control, RFN, and LED-ACXL groups (A) and average variations in the mean AF lifetime over time (B). AF lifetime images are color-coded for the mean AF lifetime as indicated in the color bar. Cross-sections cover an area of 600 × 1200 $\mu m^2$. Statistical significance obtained using *t-test*. * ρ < 0.05; ** ρ < 0.01.

Depth-dependent alterations in the AF intensity and lifetime induced by LED-ACXL are shown in Figure 7.5.6A and Figure 7.5.6B, respectively. Additionally, representative AF intensity and corresponding AF lifetime images of LED-ACXL corneas for the same corneal depth over time are shown in Figure 7.5.6C. A similar increase in both the AF intensity and mean lifetime was observed for all corneal depths 2 $h$ after ACXL. After 24, 72, and 144 $h$, the increase in both parameters becomes progressively higher in the anterior than in the posterior stroma (Figure 7.5.6A and B). At a corneal depth of 40 $\mu m$ a progressive increase in the AF intensity and lifetime can be seen (Figure 7.5.6C).

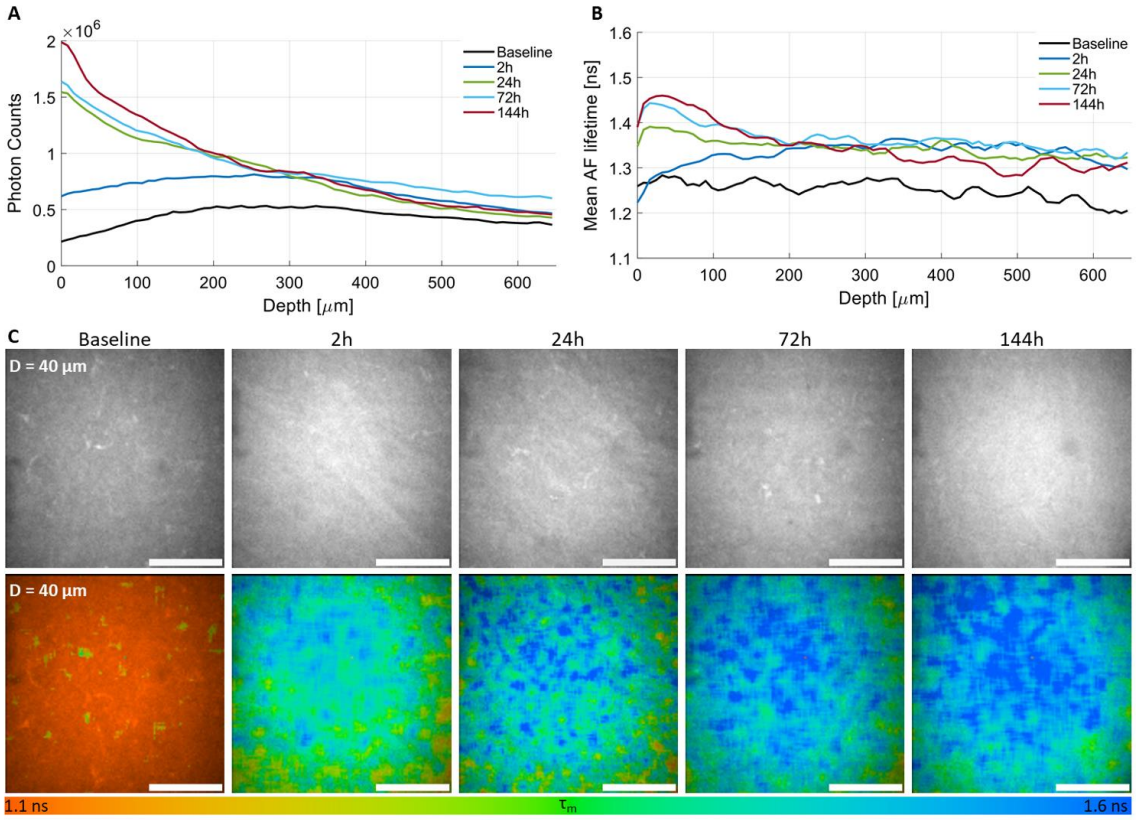


Figure 7.5.6 LED-ACXL corneal stroma autofluorescence (AF) intensity (A) and mean AF lifetime (B) as a function of depth for baseline and 2, 24, 72, and 144 $h$ after treatment. AF intensity and corresponding AF lifetime images, color-coded for the mean AF lifetime as indicated in the color bar, for the same corneal depth at baseline and 2, 24, 72, and 144 $h$ (C). Scale bar = 100 $\mu m$.

## Comparison between LED-ACXL and KXL

To confirm the feasibility of our setup to perform ACXL, the results from LED-ACXL corneas and corneas crosslinked with the commercial system KXL were compared. ACXL with both systems led to an increase in the AF lifetime after treatment, particularly in the anterior

portion of the stroma (Figure 7.5.7). No significant were observed between the stroma mean AF lifetime 24, 72, and 144 $h$ after performing ACXL with either system (Figure 7.5.7).

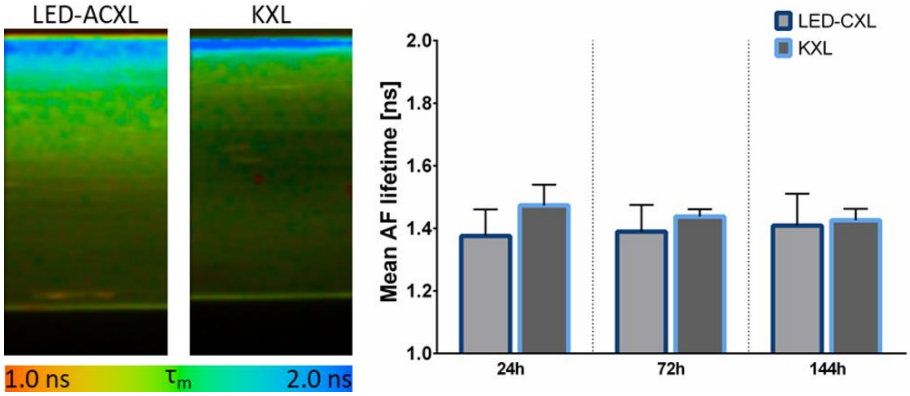


Figure 7.5.7 Cross-sectional autofluorescence (AF) lifetime images of the cornea 72 $h$ after ACXL with LED source (LED-ACXL) and the commercial system KXL™ and average alterations to the stroma mean AF lifetime over time with both light sources. Images are color-coded for the mean AF lifetime as indicated in the color bar. Cross-sections represent areas of 65 × 1250 $\mu m^2$.

## 7.5.3 ACXL-induced alterations to the AF of keratoconus corneas

Figure 7.5.8 shows cross-sectional images of a KC cornea and of a KC sample 24 $h$ after ACXL (KC-ACXL). The mean AF lifetime of both samples is also shown. As shown in the figure, the KC-ACXL has a longer mean AF lifetime than the keratoconus sample. The increase is more pronounced in the anterior stroma. Moreover, in this region a decrease in keratocytes AF was also detected (Figure 7.5.8, white arrows).

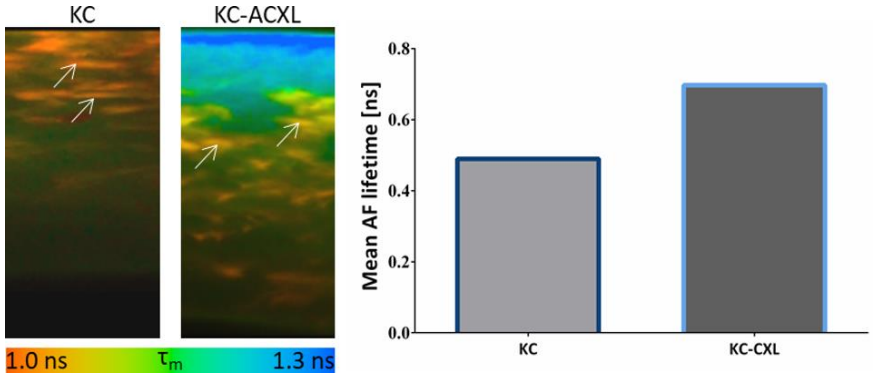


Figure 7.5.8 Cross-sectional autofluorescence (AF) lifetime images color-coded for the mean AF lifetime (as indicated in the color bar) of the keratoconus (KC) and keratoconus crosslinked (KC-ACXL) corneas 24 $h$ after ACXL with the commercial system KXL™ and their mean AF lifetime. Cross-sections represent areas of 65 × 700 $\mu m^2$. Arrows point to keratocytes AF.

# 8 DISCUSSION

The main goal of this work was to demonstrate the feasibility of TPI to image and characterize the cornea and its potential as a novel ophthalmological clinical methodology. Currently, in clinical practice, the cornea is evaluated based on its morphology. Imaging modalities such as SLBM are used to assess the cornea macroscopically and provide overall information regarding the health of the eye. The tissue is examined microscopically using techniques such as SM, CM, and AS-OCT. These techniques provide valuable and complementary information on the tissue. However, it is for the most part, limited to the tissue morphology. Information on the metabolic activity of corneal cells and the structural organization of the collagen fibers in the stroma cannot be retrieved using current clinical devices. Nevertheless, such aspects are highly important when evaluating the tissue health and viability. Changes to the cell's metabolism precede morphological ones and changes to the collagen organization are noticeable prior to those in tissue transparency.

In this study, I showed that the cornea can be simultaneously characterized based on its morphology, metabolism, and structural organization using TPI. Both porcine and human corneas were characterized using two TPI instrument setups. Both setups were optimized for corneal imaging. The results obtained show that TPI can provide morphological information similar to current imaging modalities. Different corneal layers were distinguished, and their thicknesses computed. Cells were characterized based on their anatomic properties, such as size and density. Moreover, I showed that TPI provides additional information on each layer. AF lifetime was used to assess the metabolic activity of epithelial cells, endothelial cells, and keratocytes. SHG imaging was used to assess the structural organization of collagen within the stroma. This information can complement the assessment of the cornea and improve the current state of tissue examination. I

showed that TPI is an efficient tool for the evaluation of samples in cornea banks with the potential to improve sample selection prior to transplantation. Additional information obtained from the tissue AF and SHG signals proved to be valuable for pathology characterization and can lead to better diagnostical markers. The examination of crosslinked corneas using TPI can lead to earlier assessment of the treatment outcome. In sum, TPI can improve the clinical evaluation of the cornea and the introduction of a new medical device based on this imaging modality is of high interest. Detailed discussions of the feasibility of using TPI for corneal examination (section 8.1) and its advantages for donor corneal tissue evaluation (section 8.2), pathology diagnosis (section 8.3), and CXL follow-up (section 8.4) are presented in this chapter.

## 8.1 Corneal examination using TPI

The porcine and human corneas were characterized based on their AF intensity, lifetime, and SHG with high spatial and spectral resolutions using both the 5D microscope and the MPT*flex*.

Discrimination between different layers of porcine (Figure 7.2.1) and human corneas (Figure 7.3.1) was achieved based on the tissue AF and SHG. Thus, for a good image contrast and for an accurate analysis of the fluorescence lifetime data (section 4.2.2), a high number of photons was required. Higher mean laser intensities and longer acquisition times can be used to collect more photons. However, laser-induced corneal photodamage must be avoided. In this work, the acquisition parameters of both setups were optimized to collect sufficient photons without compromising tissue safety (Figure 7.1.1).

In the corneal epithelium and endothelium, AF signals originating from NAD(P)H and flavins were anticipated. Excitation of NAD(P)H and flavins is possible using the 5D microscope and the MPT*flex* and was demonstrated (Figure 7.1.2A). Using the excitation sources of both systems, the fluorescence emission spectra of both metabolic cofactors were recorded and the maximum emission wavelengths were in agreement with reported

values of the free components of NADH and FAD [122]. However, the detection of flavins using either system seems unlikely (Figure 7.1.3 and Figure 7.1.4).

Considering the two-photon cross-sections ( $\delta$ ) of both fluorophores, a higher fluorescence emission of flavins could be anticipated. For the same excitation wavelength NAD(P)H has a $\delta_2$ of approximately 0.02 $GM$ (Göppert-Mayer = $1 \times 10^{-58}\ m^4 s$), whereas the $\delta_2$ of flavins is approximately 0.08 $GM$ [80, 83]. From equation 4.14, the number of photons absorbed per laser pulse can be computed for flavins and NAD(P)H as:

$$n_a(Flavins) \approx 0.08 \times 10^{-58} \frac{\bar{P}^2}{\tau_p f_p^2} \left( \frac{NA^2 \pi}{hc\lambda} \right)^2$$

$$n_a(NAD(P)H) \approx 0.02 \times 10^{-58} \frac{\bar{P}^2}{\tau_p f_p^2} \left( \frac{NA^2 \pi}{hc\lambda} \right)^2$$

Thus, imaging acquisition using the 5D microscope ($\bar{P}$ = 15 $mW$; $\tau_p$ = 15 $fs$; $f_p$ = 85 $MHz$; $\lambda \approx$ 800 $nm$; NA = 1.3) yields approximately $1.85 \times 10^{-2}$ excitations per pulse for flavins and only $4.63 \times 10^{-3}$ for NAD(P)H. However, the molecular concentration of NAD(P)H within the cornea is about 125 times higher that of flavins [232, 233]. So, if the mean molecular concentration of NAD(P)H is 10.000 molecules per excitation volume, only 80 molecules of flavins are present in the same volume. Then, the number of photons per laser pulse expected for NAD(P)H and flavins is, on average 46.4 and 1.5 photons, respectively. Considering the pixel dwell times used (0.11 $ms/pixel$), about 433346 NAD(P)H generated photons and 13867 flavins generated photons are emitted isotropically in space during each acquisition frame (7.4 $s$). Finally, the number of NAD(P)H and flavins generated photons detected in reflection geometry (≈ 50 %), considering a collection efficiency of 10 % and the quantum efficiency of the 16PML-PMT ($\eta \approx$ 20 %) is approximately 4333 and 139, respectively. Using the MPT*flex* ($\bar{P}$ = 50 $mW$; $\tau_p$ = 200 $fs$; $f_p$ = 80 $MHz$; $\lambda_{FAD}$ = 850 $nm$; $\lambda_{NAD(P)H}$ = 760 $nm$; NA = 1.0), approximately $5.07 \times 10^{-3}$ and $1.69 \times 10^{-3}$ excitations per pulse are expected for flavins and NAD(P)H, respectively. Considering the fluorophore's molecular concentration and a pixel dwell time of 0.024 $ms/pixel$, 158158 NAD(P)H generated photons are emitted isotropically in space during 6.2 $s$. During the same acquisition time only 3793 flavins generated photons are emitted.

Taking into consideration the collection efficiency (10 %) and the PMT's quantum efficiency ($\eta \approx 40$ %) the possible number of NAD(P)H and flavins detected photons is approximately 3163 and 76 photons, respectively.

These results show that on average for each 100 NAD(P)H detected photons, only 3.2 and 2.4 flavin photons are detected when using the 5D microscope and the MPT*flex*, respectively. Therefore, strongly decreasing the likelihood of flavins detection within the cornea using both acquisition methods. The efficiency of flavins detection could be increased, for both systems by increasing the mean laser intensity or the image acquisition time. However, an increase in either of these parameters can lead to undesired tissue damage. The use of PMTs with higher quantum efficiencies could also improve flavin detection in the cornea.

Within the cells, NAD(P)H is located both in the cell's cytoplasm and mitochondria. Thus, only these structures exhibit AF, enabling single cell discrimination and classification based on anatomic properties. Additionally, due to the high lateral resolution of TPI ($\approx$ 300 $nm$), mitochondria were resolved and loss of organelles characteristic of epithelial cell differentiation was noticeable [20].

In the stroma of both porcine and human corneas, two distinct signals were collected: SHG and AF generated from collagen and keratocytes. The feasibility of exciting and detecting both signals was demonstrated (Figure 7.1.2B and Figure 7.1.3B). The fluorescence emission spectrum of collagen was recorded and exhibited an emission maximum consistent with the literature [133]. The feasibility to detect SHG was shown using a sample of crystalized urea. Within the corneal sample, as can be perceived from the emission spectrum of the stroma (Figure 7.1.2B), AF signals are usually weaker than SHG. Therefore, the analysis of AF signals is only possible with spectral separation of the detected signals, and it was achieved with both acquisition systems.

The DM is mainly composed by collagen [20]. However, from this layer, no SHG was detected. This phenomenon has been previously reported [26, 159]. SHG is only generated by structures with noncentrosymmetric organization. Although the microstructure of collagen molecules fulfills that requirement, its macroscopic organization into fibrillary structures is also essential for SHG generation [87, 130].

Therefore, the lack of collagen organization in the DM prevents the generation of second-harmonic signals from this layer [26, 159].

In the corneal endothelium, due to single cell discrimination, cell sizes and ECDs could be computed. The values obtained for the porcine and STS human corneas are consistent with those reported for healthy pig and human tissues, respectively [20, 234].

Image acquisition using a long working distance objective allowed imaging of the entire corneal thickness in a single acquisition. Corneal thicknesses and thicknesses of individual layers computed for the porcine and human corneas are consistent with reported values [20, 24]. The capacity to record images at any depth opens the possibility to create 3D representations, *i.e.*, acquire depth-resolved information. Moreover, cross-sectional images can be directly recorded which allows a straightforward comparison between TPI images of the cornea and the standard stained histological sections.

All layers were additionally characterized based on their AF lifetime. In the cellular layers of porcine and human corneas, two NAD(P)H AF lifetime components were observed: a fast lifetime associated with its free component and a slow lifetime associated with the protein-bound component [76, 128]. Similar AF lifetimes have been previously reported for the human corneal epithelium [126].

The AF of collagen and keratocytes in the stroma was analyzed separately using demarked ROIs. The recorded collagen AF lifetimes match the short and long lifetime components reported for this fluorophore (0.3 $ns$ and 2.0 – 2.5 $ns$, respectively) [135, 136]. Keratocytes showed AF lifetimes consistent with NAD(P)H AF.

For the DM and BL in the human cornea, AF lifetimes matching those reported of collagen were also observed. However, differences in the average mean AF lifetime of these layers was noticed. As aforementioned, collagen types may exhibit different mean AF lifetimes [134]. Therefore, the type of collagen composing each layer and its overall concentration may influence their AF lifetime. Moreover, the presence of other molecular components such as glycoproteins in the DM and keratocytes in the stroma can influence collagen's microenvironment and, consequently, its AF lifetime.

The metabolic activity of the porcine cornea epithelium, endothelium, and keratocytes was evaluated and directly compared using the AF of NAD(P)H. The use of the metabolic cofactors' AF for the evaluation of the cell's metabolism has already been studied and is widely accepted. In most of the applications, the redox ratio, computed as the ratio between the AF intensity of flavins and NAD(P)H is used for metabolic assessment [122]. However, recently the AF lifetime of the endogenous fluorophores has also been taken into consideration. Walsh and Skala introduced the OMI index, which is a linear combination of the normalized redox ratio and the mean AF lifetimes of NAD(P)H and flavins [235, 236]. Additionally, Alam and Periasamy introduced a FLIM-based redox ratio, computed as the ratio between the protein-bound components of NAD(P)H and FAD ($NAD(P)H\ a_2\ \%/FAD\ a_1\ \%$) [237]. Nevertheless, these approaches consider the AF of NAD(P)H and flavins and, as discussed above, with the 5D microscope and the MPTflex, the detection of flavins from the corneal tissue is unlikely. Therefore, in this study, the ratio between the free ($a_1$) and protein-bound ($a_2$) components of NAD(P)H was used to determine the metabolic state of the corneal cells. The feasibility of using this parameter to evaluate the metabolism of cells has already been demonstrated [122, 126, 238].

The highest NAD(P)H $a_1/a_2$ ratio of the cornea was observed for keratocytes, indicating that these cells have the lowest metabolic activity of all corneal cells. These cells are usually in a quiescent state [20, 215]. Therefore, a low metabolic activity was anticipated. The results also showed that the metabolic activity of endothelial cells was significantly higher than that of epithelial cells. This is in accordance with the high metabolic rate of the endothelium [20, 23].

A depth-resolved evaluation of the AF lifetime of the porcine corneal epithelium showed characteristic changes linked with cell differentiation. Lower mean AF lifetimes and higher NAD(P)H $a_1/a_2$ ratios were observed for basal cells than for wing and superficial cells. Since fully differentiated cells have been described to have higher NAD(P)H mean AF lifetime and lower NAD(P)H $a_1/a_2$ ratios than their stem cell precursors, these results may be related to the differentiation of basal cells into wing and superficial cells [238, 239].

The organization of collagen fibers within the stroma was obtained from SHG images of the tissue. As previously demonstrated, SHG signals can be recorded in both backward and forward directions. However, they yield very different images. Whereas in forward

detected SHG images the orientation of the fibers can be directly seen, the same is not possible in backward detected images. These is related to the small diameter of collagen fibers and the impossibility to resolve them in the backward direction. Nevertheless, the organization of collagen fibers can also be extrapolated from backward detected SHG images. In this study, a novel parameter obtained from FFT analysis, termed peak prominence (PP) of the main orientation, was introduced to retrieve the overall alignment of collagen fibers. The feasibility to obtain the organization of collagen fibers from forward and backward detected SHG images was demonstrated (Figure 7.2.7). Although lower PP values were computed for backward detected SHG images, the distribution pattern of PP values was equivalent for both acquisition methods. This indicates that both imaging configurations yield similar information regarding stromal structural organization. The values of PP cannot be compared between backward and forward direction images, but comparing two, either backward or forward, detected images should yield the same conclusions. Our group has also demonstrated previously that the orientation of collagen fibers in the stroma could be computed with good agreement from backward and forward detected polarized-resolved SHG images [175].

## 8.2 Human corneal donor selection prior to transplantation

Transplantation is the last clinical option to restore the sight of patients affected with corneal pathologies when all other treatments have failed. Performed successfully for the first time in the early 20$^{th}$ century [240], the transplant of the cornea is currently the most common type of transplantation in the world [2, 3] with over 60 000 patients being transplanted every year [3].

The success rates of corneal transplantations are higher than other organ transplants due to the tissue inherent immune privilege [241, 242]. Nevertheless, rejection of corneal grafts still occurs in about 3000 to 4200 cases yearly [3]. Several risks factors have been attributed to rejections, such as corneal storage methods and duration [3]. Moreover, the

number of transplants is limited by donor corneal buttons' availability. Worldwide only one cornea is available for every seventy needed [2]. Meanwhile, a significant percentage of donated corneas is excluded for transplantation due to suitability problems, such as low ECDs. The donor's medical record and positive blood serology are other exclusion factors [4, 5].

The methods currently used for the evaluation of donor corneal tissue solely depend on the analysis of tissue morphology. Thus, the cell's metabolism and stromal structural organization are disregarded. TPI can provide a more complete evaluation of human corneas than current clinical devices. Based on TPI, the suitability of donor corneal buttons can be assessed using morphological, metabolic, and structural features. Thus, this imaging modality may improve the assessment of the corneal suitability for transplantation. Moreover, it could be used to evaluate the tissue-storage conditions, possibly leading to their improvement and consequently to an increase of the number of samples usable for transplantation.

The analysis of endothelial cells is mandatory in pre-transplantation evaluation since these cells do not regenerate and are essential to the proper function of the cornea [20–23]. As discussed in the previous section, TPI can also provide important morphological information on the endothelial layer such as cell size, shape, and density. With storage time, a decrease in the ECDs and cell enlargement was observed. Such alterations were already anticipated due to endothelial cell loss [20–23]. A decrease in the epithelial thickness was also observed with storage. This indicates that during storage this layer does not regenerate at a rate sufficiently high to maintain an intact surface.

The evaluation of ECDs and layer thickness, although important to assess the viability of the tissue, can already been obtained using the current clinical devices. One of the great advantages of using TPI is the feasibility to additionally assess changes in the cell's metabolism. To the best of my knowledge, this study describes for the first time the changes in metabolic activity of all corneal cell types over time based on the AF lifetime of metabolic cofactors (Figure 7.3.4). In the corneal epithelium and endothelium, a significant increase in the NAD(P)H $a_1/a_2$ ratio was observed. Such alterations to the free to protein-bound ratio of this metabolic cofactor were already anticipated and have been associated with a decrease in energy production [122, 126]. Higher NAD(P)H $a_1/a_2$ ratios

have also been observed for the epithelial cells of samples stored for 1 week and 1 month when compared to fresh samples [126]. For keratocytes, the opposite behavior was observed. NAD(P)H $a_1/a_2$ ratio decreased significantly with storage time, indicating an increase in the metabolic activity. This indicates that keratocytes, which are usually activated in the case of corneal injury [20], may also become active due to adverse storage conditions.

Another advantage of TPI in the evaluation of donor corneal tissue is the possibility to infer on early alterations of tissue transparency based on SHG imaging. Corneal transparency is essential for the proper function of the tissue and must also be evaluated prior to transplantation. However, with the exception of some in-house developed systems, this evaluation is usually subjective [243]. I demonstrate that TPI can also provide an objective evaluation on tissue transparency. The analysis of the arrangement of collagen fibers within the stroma using both GLCM and FFT analysis, showed a significant decrease in the corneal stroma organization with storage. Such a decrease was anticipated and should be detectable prior to any noticeable alterations in the corneal transparency. A higher degree of organization was also observed for the stroma than the BL of STS samples. Considering the anatomic characteristics of collagen fibers in the BL and in the stroma [20] such an increase was already expected.

## 8.3 Diagnosis of corneal pathologies

Pathologies and dysfunctions of the cornea are the second major cause of blindness in the world, with cataracts being the first [1]. Therefore, a precise and early diagnosis is of major importance and essential to ensure a positive prognosis. The advances in corneal imaging modalities have improved the diagnosis of pathologies and led to earlier and earlier detections. However, these advances were limited to the evaluation of morphological alterations. Information on pathology-induced changes to the cell's metabolism and the structural organization of the stroma cannot yet be retrieved and evaluated in clinical practice.

In this study, NP human corneas and corneas diagnosed with different pathologies were characterized at multiple depths based on their AF intensity, lifetime, and SHG. Differences between NP and pathological corneas were used to demonstrate the feasibility of TPI to diagnose corneal diseases. The samples were distinguishable not only by their morphology but also by their metabolic activity, structural organization of collagen fibers, and stroma mean AF lifetime. Therefore, TPI provides information complementary to current clinical devices which can lead to an improved diagnosis and enhance our understanding of the pathophysiology of different diseases.

The AF intensity was used to reveal the morphological changes caused by each pathology, while its AF lifetime provided additional insight into these changes. Moreover, the AF lifetime of NAD(P)H was used to infer on the cell's metabolism. Pathology-induced changes in the corneal stroma were also evaluated based on the combined analysis of AF and SHG signals. FFT analysis of SHG images was used to assess the collagen fibers' organization. The evaluation of the stroma AF lifetime is an additional source of information that enables further discrimination between pathologies. To the best of my knowledge, this was the first time the corneal epithelium and stroma were investigated simultaneously to characterize these pathologies.

In KC affected samples, morphological changes characteristic of the pathology, such as the elongation and enlargement of corneal epithelial cells and the decrease in epithelial thickness, were detected [213, 214]. These changes can already be observed in clinical practice using, for instance, CM. The introduction of this and other imaging modalities (*e.g.* corneal topography and AS-OCT) have improved KC detection. Nevertheless, the results are not always clear [214]. Additionally, the pathophysiological mechanisms of KC are not fully known [213].

The analysis of AF lifetime of KC corneas revealed that cells with abnormal morphology had longer mean AF lifetime than normal cells. Additionally, significantly higher NAD(P)H $a_1/a_2$ ratios than those of NP samples were observed, indicating a decrease in cell's metabolic activity induced by the pathology [126]. In the corneal stroma, a significant decrease in the mean AF lifetime was noticeable. This might be related to the decrease in the number of crosslinks between collagen molecules [244, 245]. A decrease in the organization of collagen fibers was also observed for this pathology (Figure 7.4.5A). KC

induces stroma thinning and a decrease in the number of collagen lamellae [213, 214]. Therefore, such a decrease was already anticipated. The feasibility of SHG imaging to assess KC-induced changes has been previously reported [174, 186–188]. Using SHG imaging, changes in the distribution patterns of collagen lamellar [186], their level of interweaving [188], and their orientation have been shown [174, 187].

The diagnosis of AK has greatly improved after the introduction of CM, since it provides additional information on the clinical features of AK, *e.g.* the *in vivo* detection of *amoeba* cysts [217]. Nevertheless, misdiagnosis of AK still occurs [215]. Based on TPI, AK detection may be further improved. Using TPI, unexpected AF signals were detected from the epithelial cell's membrane of the AK affected cornea. These were not present for any other condition. This phenomenon is likely related to the presence of *amoeba* within the epithelium. These free-living organisms attach themselves to the epithelium and induce tissue degradation to infiltrate into deeper layers [215, 216]. Several areas where basal cells were absent, together with a decrease in the epithelial thickness, were detected. Additionally, the metabolic activity of epithelial cells appears to be diminished. These findings are coherent with tissue degradation. In the corneal stroma, the degradation of the tissue may be followed by stroma regeneration and restructuring with a lower degree of organization. Thus, justifying the decrease observed in the stroma organization metric (PP). A decrease in the stroma mean AF lifetime was also observed. However, only one cornea with AK was used. Additional diseased corneas are needed to confirm and better understand these changes.

The opacification of the cornea due to SCS is usually detected using low resolution techniques such as SLBM [218]. TPI can detect changes in collagen fibers' arrangement prior to visible opacification. Therefore, it could lead to important advancements in SCS detection. In the cornea diagnosed with SCS, a decrease in corneal epithelial thickness and debris deposition throughout this layer was observed. These alterations might be justified by augmented cell proliferation to fill gaps caused by scarring and to maintain layer smoothness [246]. An increase in the epithelial cells NAD(P)H $a_1/a_2$ ratio, indicating an increase in these cells metabolic activity, was also noticeable [126]. In the stroma of the SCS affected cornea, an increase in the mean AF lifetime and a decrease in the degree of collagen fiber's alignment was observed. Stroma wound healing is mediated by

keratocytes. In case of trauma, these cells are activated and migrate to the injured location where they may differentiate into myofibroblasts. These cells are by themselves opaquer then keratocytes and can produce high quantities of disorganized ECM. Ultimately, this leads to the opacification of the cornea [218]. Therefore, alterations in the organization of collagen fibers in the stroma of SCS corneas were expected. Nevertheless, a higher number of SCS samples is required to draw definite conclusions.

## 8.4 Evaluation of the outcome of corneal collagen crosslinking

Currently, the clinical outcome of CXL/ACXL is evaluated by assessing the patients best corrected and uncorrected visual acuity, the corrected and uncorrected distance visual acuity, and the cornea curvature, several weeks after treatment [193], or by CM evaluation. An increase in the corneal stroma reflectivity, edema, and keratocytes apoptosis are some of the features noticeable by CM. Moreover, CM can be used to monitor nerve regeneration in the cornea [66, 193, 247, 248]. Recently, the feasibility of AS-OCT to evaluate crosslinked corneas has also been demonstrated [65, 249, 250]. In crosslinked corneas a hyperreflective line at the transition between crosslinked and non-crosslinked regions is visible. This demarcation line provides information about the depth until which CXL was effective [65, 249, 250]. Although, these clinical devices can provide valuable information about CXL efficiency, they are usually performed several weeks after the procedure. Therefore, a new imaging modality capable of evaluating CXL effects in the corneal stroma short after the procedure is of interest.

In this study, the feasibility of TPI to assess the outcome of ACXL was demonstrated based on the stroma AF intensity and lifetime. Moreover, a depth-dependence analysis of the stroma AF, demonstrated the feasibility to discriminate between crosslinked and non-crosslinked areas using TPI. The results show that ACXL-induced changes to the stroma AF intensity and lifetime can be detected soon after treatment. Therefore, TPI imaging can

provide a noninvasive, label-free, and fast evaluation of crosslinked corneas sooner than current clinical devices.

The efforts to assess the clinical outcome of CXL soon after treatment are not new. Recently, the feasibility of evaluating of CXL-induced changes to the corneal stroma using Brillouin microscopy has been demonstrated [251–253]. Brillouin microscopy is an imaging modality that can provide the Young's modulus of the tissue. After CXL, an increase in the Brillouin shift, which correlates with an increase in corneal stiffness, was reported [251–254]. However, the major drawback of this imaging modality is the very long acquisition time required for generating a single image. Acquisition times between 30 and 120 $min$ per image have been reported [251–253].

CXL evaluation based on TPI has also been demonstrated. However, most studies relate to the evaluation of changes to collagen fibers' organization by SHG imaging [170, 189–192]. Along with SHG, the AF of the stroma also provides valuable information. Nevertheless, to the best of our knowledge, the characterization and monitoring of the stroma AF of crosslinked human corneas has not yet been performed. As such, in this study, CXL-induced changes to the stroma AF intensity and lifetime were investigated.

In the corneal stroma, collagen and keratocytes' metabolic cofactors are sources of AF. Their emission spectra overlap with that of riboflavin fluorescence. Therefore, to avoid the influence of riboflavin on the analysis of the stroma AF, the removal of this fluorophore from the tissue at the time of the measurements was necessary. The minimum time required for riboflavin to diffuse out of the cornea was monitored based on the tissue AF intensity and lifetime. Following riboflavin application, a significant increase in both the AF intensity and lifetime was observed due to the fluorophore's intrinsic fluorescence. Moreover, data shows that the contribution of stroma AF to the detected signal immediately after applying riboflavin was negligible. Baseline levels of AF intensity and lifetime were reached after 2 $h$. Therefore, we concluded that after 2 $h$ riboflavin has diffused out of the tissue. This was defined as the minimum time to wait after ACXL to perform the evaluation of the corneal stroma AF. *In vivo* measurements of riboflavin diffusion must be performed to determine the first time point for CXL evaluation in patients.

ACXL was performed in human corneas using an in-house adapted setup. Therefore, the feasibility of this setup to efficiently induced new crosslink bounds between collagen molecules and fibrils was experimentally demonstrated (Figure 7.5.7). ACXL with our setup or with a commercial ACXL device yielded similar results.

The stroma AF intensity and lifetime of LED-CXL was significantly higher 2 $h$ after the procedure and in subsequent measurements when compared with baseline (Figure 7.5.4 and Figure 7.5.5). A higher stroma mean AF lifetime was also observed in KC crosslinked corneas when compared with KC samples (Figure 7.5.8). For the control and RFN groups no significant alterations were observed between measurements. An increase in the stroma AF intensity and lifetime has also been found, two weeks after CXL, for rabbit corneas [203]. Riboflavin application also led to alterations in the stroma AF which the authors attributed to room light CXL [203]. To avoid this, in our study, light exposure of riboflavin-infused corneas was minimized.

ACXL-induced changes to the stroma AF are likely related to the number of crosslinks between collagen. It has been previously demonstrated, for *in vitro* collagen gels, that the number of crosslinks between collagen molecules is correlated with the AF lifetime [244, 245]. A decrease in the AF lifetime was observed for collagen gels with reduced number of crosslinks, whereas models of enhanced CXL showed an increase of 9% in the mean AF lifetime [244, 245]. The changes in AF lifetime are correlated with the specific amino acids involved in the crosslinks at the collagen crosslinking sites [245]. Therefore, the increase in the AF lifetime after ACXL is an indicative of a positive outcome.

A depth-resolved analysis of the tissue AF demonstrated the feasibility of TPI to discriminate between crosslinked and non-crosslinked areas. A higher increase in the AF intensity and lifetime was observed in the anterior than in the posterior stroma. This indicates that a higher number of new crosslinks were induced anteriorly. Typically, CXL is most effective in the anterior stroma due the limited penetration of UVA light. Therefore, such results were anticipated. In KC samples, the increase AF lifetime was also more pronounced in the anterior stroma. Moreover, a depletion of keratocytes AF consistent with the cell apoptosis due to ACXL was observed [255]. This indicates a positive ACXL outcome. However, more KC samples must be investigated to draw definite conclusions.

Interestingly, for the same corneal depth, an increase in AF lifetime was observed overtime. Therefore, depth-dependent changes to the tissue AF may also help improve our understanding on the mechanisms by which ACXL induces corneal stiffening.

# 9 CONCLUSIONS AND OUTLOOK

In this study, I demonstrated the potential of TPI to characterize corneal metabolism and stromal structural organization with high spatial and spectral resolutions, in parallel with typical morphological examinations. Using TPI, all anatomic layers of the porcine and human corneas were evaluated. The AF intensity of the tissue revealed morphological aspects of each layer with subcellular resolution. For the cellular layers, the NAD(P)H AF was used to obtain information on the cell's metabolic activity. Although other fluorophores are present in the corneal cellular layers, spectral analysis of the tissue revealed that their influence is negligible. To the best of my knowledge, I described for the first time a comparison between the metabolic activity of epithelial cells, endothelial cells, and keratocytes based on the NAD(P)H $a_1/a_2$ ratio. The depth-resolved evaluation of the epithelial layer showing the metabolic changes induced by cell differentiation was also described. Moreover, a new parameter for retrieving information on the organization of collagen within the stroma based on FFT analysis of backward detected SHG was introduced and demonstrated.

Three possible clinical applications of TPI were evaluated and their advantages over current clinical devices investigated. I showed that TPI can provide the same morphological information already used to assess the viability of human corneal donor buttons *ex vivo*. Moreover, I demonstrated that this imaging modality provides additional information on the tissue that can aid in sample selection prior to transplantation. The tissue information retrieved by TPI could also be used to improve storage methods. I report on a decrease in the metabolic activity of epithelial and endothelial cells, accompanied by an increase of keratocytes metabolism with storage time. To the best of my knowledge, the alterations induced by storage to the metabolism all corneal cell types have not been previously reported. GLCM and FFT analysis of SHG images were used to

evaluate the organization of collagen within the stroma. A significant decrease in the organization of the collagen fibers was observed. Thus, TPI can provide an objective evaluation of corneal cells morphology, metabolism, and tissue transparency.

The feasibility to diagnose corneal pathologies using TPI was also demonstrated through the comparison between NP corneas and corneas diagnosed with either KC, AK, or SCS. I showed that TPI provides information not only on the morphological alterations induced by these pathologies, but also on pathology-induced metabolic and structural changes. These additional levels of information can provide further discrimination between NP and pathological corneas as well as between different pathologies. Therefore, corneal diagnosis may be improved by using TPI. Moreover, TPI could be used to better understand the pathophysiology of different diseases.

The evaluation of the clinical outcome of CXL using TPI was also investigated. I showed that alterations in the corneal stroma AF lifetime can be used to evaluate the success or failure of this medical procedure label-free and with high resolution as soon as 2 $h$ after treatment, *i.e.*, much sooner than the current clinical standard. A significant increase in the mean AF lifetime of the stroma consistent with an increase in the number of collagen crosslinks was observed for ACXL samples.

This work shows that the examination of the human cornea can be significantly improved using TPI. It can enhance the assessment of samples prior to transplantation, corneal diagnosis, and the follow-up after medical procedures. Therefore, a new medical device based on TPI would be of great interest. In the future, we intend to further optimize the TPI systems for corneal imaging and continue the evaluation of human corneas during storage as well as the examination of diseased human corneas immediately after surgery and after CXL to increase total number of samples measured. This will further demonstrate the potential of TPI as a novel ophthalmologic imaging modality. Moreover, our group is currently attempting to receive approval from the ethics committee to perform the first ever *in vivo* TPI measurements of the human cornea. This will open the window for clinical cornea imaging based on TPI and the introduction of a novel clinical instrument.

# LIST OF PUBLICATIONS

## Peer-reviewed publications:

1. **Ana Batista**, Hans Georg Breunig, Aisada König, Andreas Schindele, Tobias Hager, Berthold Seitz, and Karsten König, ***"High-resolution, label-free two-photon imaging of diseased human corneas"*** Journal of Biomedical Optics 23(3), 036002: 1-8, 2018.
   [doi: 10.1117/1.JBO.23.3.036002].

2. **Ana Batista**, Hans Georg Breunig, Aisada König, Andreas Schindele, Tobias Hager, Berthold Seitz, António Miguel Morgado, and Karsten König, ***"Assessment of human corneas prior to transplantation using high-resolution two-photon imaging"*** Investigative Ophthalmology & Visual Science 59(1), 176-184, 2018.
   [doi: 10.1167/iovs.17-22002].

3. **Ana Batista**, Hans Georg Breunig, Aisada König, António Miguel Morgado, and Karsten König, ***"Assessment of the metabolism and morphology of the porcine cornea, lens, and retina by two-photon imaging***" Journal of Biophotonics 11(7), e201700324, 2018
   [doi: 10.1002/jbio.201700324].

4. **Ana Batista**, Hans Georg Breunig, Aisada Uchugonova, António Miguel Morgado, and Karsten König, ***"Two-Photon Spectral Fluorescence Lifetime and Second-Harmonic Generation Imaging of the Porcine Cornea with a 12 Femtosecond Laser Microscope"*** Journal Biomedical Optics 21(3), 036002: 1-11, 2016.
   [doi:10.1117/1.JBO.21.3.036002].

5. Hans Georg Breunig, **Ana Batista**, Aisada Uchugonova, and Karsten König, ***"Cell optoporation with a sub-15 fs and a 250-fs laser***", Journal Biomedical Optics 21(06), 060501: 1-4, 2016
   [doi: 10.1117/1.JBO.21.6.060501].

6. Aisada Uchugonova, Hans Georg Breunig, **Ana Batista**, and Karsten König, ***"Optical reprogramming of human cells in an ultrashort femtosecond laser microfluidic transfection platform"***, Journal of Biophotonics 9(9), 942-947, 2016.
   [doi: 10.1002/jbio.201500240].

7. Aisada Uchugonova, Hans Georg Breunig, **Ana Batista**, and Karsten König, ***"Optical reprogramming of human somatic cells using ultrashort Bessel-shaped near-infrared femtosecond laser pulses"***, Journal Biomedical Optics 20(11), 115008 2015.
   [doi: 10.1117/1.JBO.20.11.115008].

8. Hans Georg Breunig, Aisada Uchugonova, **Ana Batista**, and Karsten König, ***"Software-aided automatic laser optoporation and transfection of cells"***, Scientific Reports 5(1), 11185, 2015.
[doi: 10.1038/srep11185].

9. **Ana Batista**, Susana Figueiredo Silva, João Paulo Domingues, and António Miguel Morgado, ***"Fluorescence Lifetime Based Corneal Metabolic Imaging"***, Procedia Technology 17(1), 281-288, 2014.
[doi: 10.1016/j.protcy.2014.10.238].

10. Hans Georg Breunig, Aisada Uchugonova, **Ana Batista**, and Karsten König, ***"High-throughput continuous flow femtosecond laser-assisted cell optoporation and transfection"***, Microscopy Research and Technique 77(12), 974-979, 2014.
[doi: 10.1002/jemt.22423].

11. João Martins, Miguel Castelo-Branco, **Ana Batista**, Bárbara Oliveiros, Ana Raquel Santiago, Joana Galvão, Eduarda Fernandes, Félix Carvalho, Cláudia Cavadas, and António Francisco Ambrósio, ***"Corneal Metabolic State Assessment by Fluorescence Lifetime Imaging Microscopy"*** PLoS ONE 6(12), e29583, 2011.
[doi: 10.1371/journal.pone.0029583].

## Book Chapters:

1. **Ana Batista**, Hans Georg Breunig, Christoph Donitzky, and Karsten König, ***"Two-photon microscopy and fluorescence lifetime imaging of the cornea"*** in Multiphoton Microscopy and Fluorescence Lifetime Imaging (ed. König, K.) 301–320, De Gruyter, 1st Ed., Berlin, Boston, 2018.
[doi: 10.1515/9783110429985-018].

## Published conference proceedings:

1. **Ana Batista**, Hans Georg Breunig, and Karsten König, ***"Rapid in vivo vertical tissue sectioning by multiphoton tomography"*** Proc. SPIE 10498, 1049814:1-6, 2018.
[doi: 10.1117/12.2286915].

2. Karsten König, Hans Georg Breunig, **Ana Batista**, Benjamin Sauer, and Aisada Uchugonova, ***"Femtosecond-laser setup for cell-membrane poration"*** Proc. SPIE 10497, 104970K:1-5, 2018.
[doi: 10.1117/12.2287384].

3. **Ana Batista**, Aisada Uchugonova, Hans Georg Breunig, and Karsten König, ***"In vivo multiphoton imaging of the eyelid skin"*** Proc. SPIE 10037, 100370E:1-7, 2017. [doi: 10.1117/12.2251949].

4. **Ana Batista**, Hans Georg Breunig, Aisada Uchugonova, and Karsten König, ***"Towards in vivo breast skin characterization using multiphoton microscopy"*** Proc. SPIE 10069, 100691Y:1-6, 2017. [doi: 10.1117/12.2252387].

5. Karsten König**, Ana Batista**, Hans Georg Breunig, Tobias Hager, Berthold Seitz, **"Multiphoton tomography of the human eye"** Proc. SPIE 10069, 1006906:1-8, 2017. [doi: 10.1117/12.2255151].

6. Hans Georg Breunig, Aisada Uchugonova, **Ana Batista**, and Karsten König, ***"Femtosecond-laser assisted cell reprogramming"*** Proc. SPIE 10068, 1006811:1-8, 2017. [doi: 10.1117/12.2252088].

7. Susana Figueiredo Silva, **Ana Batista**, João Paulo Domingues, Maria João Quadrado, and António Miguel Morgado, ***"Time-gated FLIM microscope for corneal metabolic imaging"*** Proc. SPIE 9712, 97122C:1-7, 2016. [doi: 10.1117/12.2214182].

8. **Ana Batista**, Hans Georg Breunig, Aisada Uchugonova, António Miguel Morgado, and Karsten König, ***"Characterization of porcine eyes based on autofluorescence lifetime imaging"*** Proc. SPIE 9329, 93290E:1-8, 2015. [doi: 10.1117/12.2077563].

9. **Ana Batista**, Hans Georg Breunig, Aisada Uchugonova, Berthold Seitz, António Miguel Morgado, and Karsten König, ***"Two-photon autofluorescence lifetime and SHG imaging of healthy and diseased human corneas"*** Proc. SPIE 9307, 93071Q:1-8, 2015. [doi: 10.1117/12.2077569].

10. Hans Georg Breunig, **Ana Batista**, Aisada Uchugonova, and Karsten König, ***"Motionless polarization-resolved second harmonic generation imaging of corneal collagen"*** Proc. SPIE 9329, 93292P:1-6, 2015. [doi: 10.1117/12.2078701].

11. Susana Figueiredo Silva, **Ana Batista**, Olga Ciutad Castejón, Maria João Quadrado, João Paulo Domingues, and António Miguel Morgado, ***"Development of a time-gated fluorescence lifetime microscope for in vivo corneal metabolic imaging"*** Proc. SPIE 9537, 953709:1-9, 2015. [doi: 10.1117/12.2183945].

12. Susana Figueiredo Silva, **Ana Batista**, João Paulo Domingues, Maria João Quadrado, and António Miguel Morgado, ***"Fluorescence lifetime microscope for corneal metabolic imaging"*** IEEE 4th Portuguese Meeting on Bioengineering, 1-5, 2015.
[doi: 10.1109/ENBENG.2015.7088878].

13. Hans Georg Breunig, **Ana Batista**, Aisada Uchugonova, and Karsten König, ***"Software aided automatic cell optoporation system"*** Proc. SPIE 9328, 93280D:1-6, 2015.
[doi: 10.1117/12.2078728].

14. Aisada Uchugonova, Hans Georg Breunig, **Ana Batista**, and Karsten König, ***"Optical cell cleaning with NIR femtosecond laser pulses"*** Proc. SPIE 9328, 932819:1-5, 2015.
[doi: 10.1117/12.2080867].
15. Aisada Uchugonova, Hans Georg Breunig, **Ana Batista**, and Karsten König, ***"Optical reprogramming with ultrashort femtosecond laser pulses"*** Proc. SPIE 9329, 93290U:1-6, 2015.
[doi: 10.1117/12.2080872].

16. **Ana Batista**, António Miguel Morgado, and Karsten König, **"Detection of back-reflected SHG from corneal histological sections"** Proc. SPIE 8948, 89482B:1-7, 2014.
[doi: 10.1117/12.2038251].

17. **Ana Batista**, Hans Georg Breunig, Aisada Uchugonova, Berthold Seitz, António Miguel Morgado, and Karsten König, **"Label-free SHG imaging and spectral FLIM of corneas using a sub-15 fs laser microscope"** Proc. SPIE 8930, 89300V:1-9, 2014.
[doi: 10.1117/12.2037640].

18. Aisada Uchugonova, **Ana Batista**, and Karsten König, ***"Fluorescence lifetime imaging of induced pluripotent stem cells"*** Proc. SPIE 8948, 89481I:1-7, 2014.
[doi: 10.1117/12.2037662].

19. **Ana Batista**, Susana Figueiredo Silva, João Paulo Domingues, and António Miguel Morgado, **"Corneal metabolic imaging by FAD autofluorescence lifetime"** IEEE 3rd Portuguese Meeting in Bioengineering, 1-4, 2013.
[doi: 10.1109/ENBENG.2013.6518396].

20. **Ana Batista**, Custódio Loureiro, João Paulo Domingues, José Silvestre Silva, and António Miguel Morgado, ***"Corneal Metabolic State Assessment by Fluorescence Lifetime Imaging Microscopy"*** Microscopy and Microanalysis 19(4), 7-8, 2013.
[doi: 10.1017/S1431927613000652].

21. **Ana Batista**, Custódio Loureiro, João Paulo Domingues, José Silvestre Silva, and António Miguel Morgado, **"Corneal respiratory function by FAD autofluorescence lifetime"** Acta Ophthalmologica 90, s249, 2012.

[doi: 10.1109/ENBENG.2013.6518396].

22. **Ana Batista**, Custódio Loureiro, João Paulo Domingues, José Silvestre Silva, and António Miguel Morgado, **"Corneal Cells Metabolic Imaging using FAD Fluorescence Lifetime"** OSA Technical Digest (online), LT1A.5, 2012.
[doi: 10.1364/LAOP.2012.LT1A.5].

23. **Ana Batista**, Custódio Loureiro, João Paulo Domingues, José Silvestre Silva, and António Miguel Morgado, **"FLIM as a tool for metabolic imaging of the cornea"** IEEE 2nd Portuguese Meeting in Bioengineering, 1-4, 2012.
[doi: 10.1109/ENBENG.2012.6331350].

24. **Ana Batista**, **"Exploring the impact of ecstasy on retinal physiology: A pioneer study"** IEEE 2nd Portuguese Meeting in Bioengineering, 1-6, 2012.
[doi: 10.1109/ENBENG.2012.6331389].

# REFERENCES


1. Whitcher, J. P., Srinivasan, M., and Upadhyay, M. P. Corneal blindness: a global perspective. *Bull World Heal. Organ* **79 (3)**, 214–221, **2001**.

2. Gain, P., Jullienne, R., He, Z., Aldossary, M., Acquart, S., Cognasse, F., and Thuret, G. Global Survey of Corneal Transplantation and Eye Banking. *JAMA Ophthalmol.* **134 (2)**, 167–173, **2016**. [10.1001/jamaophthalmol.2015.4776]

3. Panda, A., Vanathi, M., Kumar, A., Dash, Y., and Priya, S. Corneal Graft Rejection. *Surv. Ophthalmol.* **52 (4)**, 375–396, **2007**. [10.1016/j.survophthal.2007.04.008]

4. Jones, G. L. A., Dekaris, I., Hjortdal, J., and Pels, E. European Eye Bank Association: Past, Present, and Future. *Int. J. Eye Bank.* **1 (1)**, 1–6, **2012**. [10.7706/ijeb.v1i1.26]

5. Eye Bank Association Of America. *2015 Eye Banking Statistical Report*. **2016**.

6. Yu, A., Schaumberger, M., Kaiser, M., Messmer, E., Kook, D., and Welge-Lussen, U. Perioperative and postoperative risk factors for corneal graft failure. *Clin. Ophthalmol.* **8**, 1641, **2014**. [10.2147/OPTH.S65412]

7. Sellami, D., Abid, S., Bouaouaja, G., Ben Amor, S., Kammoun, B., Masmoudi, M., Dabbeche, K., Boumoud, H., Ben Zina, Z., and Feki, J. Epidemiology and Risk Factors for Corneal Graft Rejection. *Transplant. Proc.* **39 (8)**, 2609–2611, **2007**. [10.1016/j.transproceed.2007.08.020]

8. König, K., Wollina, U., Riemann, I., Peukert, C., Halbhuber, K.-J., Konrad, H., Fischer, P., Fuenfstueck, V., Fischer, T. W., and Elsner, P. Optical tomography of human skin with subcellular spatial and picosecond time resolution using intense near infrared femtosecond laser pulses. in *Proc. SPIE* (eds. Periasamy, A. & So, P. T. C.) **4620**, 191–201, **2002**. [10.1117/12.470692]

9. König, K., Weinigel, M., Breunig, H. G., Gregory, A., Fischer, P., Kellner-Höfer, M., Bückle, R., Schwarz, M., Riemann, I., Stracke, F., Huck, V., Gorzelanny, C., and Schneider, S. W. 5D-intravital tomography as a novel tool for non-invasive in-vivo analysis of human skin. in *Proc. SPIE* (eds. Vo-Dinh, T., Grundfest, W. S. &

Mahadevan-Jansen, A.) **7555**, 75551I:1-6, **2010**. [10.1117/12.841861]

10. Huck, V., Gorzelanny, C., Thomas, K., Niemeyer, V., Luger, T. a., König, K., and Schneider, S. W. Intravital multiphoton tomography as a novel tool for non-invasive in vivo analysis of human skin affected with atopic dermatitis. in *Proc. SPIE* (eds. Kollias, N. et al.) **7548**, 75480B:1-6, **2010**. [10.1117/12.841973]

11. Balu, M., Kelly, K. M., Zachary, C. B., Harris, R. M., Krasieva, T. B., König, K., Durkin, A. J., and Tromberg, B. J. Distinguishing between benign and malignant melanocytic nevi by in vivo multiphoton microscopy. *Cancer Res.* **70 (10)**, 2688–2697, **2014**. [10.1016/j.pestbp.2011.02.012.Investigations]

12. Seidenari, S., Arginelli, F., Dunsby, C., French, P. M. W., König, K., Magnoni, C., Talbot, C., and Ponti, G. Multiphoton Laser Tomography and Fluorescence Lifetime Imaging of Melanoma: Morphologic Features and Quantitative Data for Sensitive and Specific Non-Invasive Diagnostics. *PLoS One* **8 (7)**, e70682:1-9, **2013**. [10.1371/journal.pone.0070682]

13. Seidenari, S., Arginelli, F., Bassoli, S., Cautela, J., Cesinaro, A. M., Guanti, M., Guardoli, D., Magnoni, C., Manfredini, M., Ponti, G., and König, K. Diagnosis of BCC by multiphoton laser tomography. *Ski. Res. Technol.* **19 (1)**, 297–304, **2013**. [10.1111/j.1600-0846.2012.00643.x]

14. Balu, M., Zachary, C. B., Harris, R. M., Krasieva, T. B., König, K., Tromberg, B. J., and Kelly, K. M. In Vivo Multiphoton Microscopy of Basal Cell Carcinoma. *JAMA Dermatology* **151 (10)**, 1068–1075, **2015**. [10.1001/jamadermatol.2015.0453]

15. Klemp, M., Meinke, M. C., Weinigel, M., Röwert-Huber, H. J., König, K., Ulrich, M., Lademann, J., and Darvin, M. E. Comparison of morphologic criteria for actinic keratosis and squamous cell carcinoma using in vivo multiphoton tomography. *Exp. Dermatol.* **25 (3)**, 218–222, **2016**. [10.1111/exd.12912]

16. Schweitzer, D., Kolb, A., Hammer, M., and Anders, R. Time-resolved measurement autofluorescence. A method to detect metabolic changes in the fundus. *Ophthalmologe* **99 (10)**, 774–779, **2002**. [10.1007/s00347-002-0656-3]

17. Schweitzer, D., Quick, S., Schenke, S., Klemm, M., Gehlert, S., Hammer, M., Jentsch,

S., and Fischer, J. Comparison of parameters of time-resolved autofluorescence between healthy subjects and patients suffering from early AMD. *Ophthalmologe* **106 (8)**, 714–722, **2009**. [10.1007/s00347-009-1975-4]

18. Schweitzer, D., Deutsch, L., Klemm, M., Jentsch, S., Hammer, M., Peters, S., Haueisen, J., Müller, U. A., and Dawczynski, J. Fluorescence lifetime imaging ophthalmoscopy in type 2 diabetic patients who have no signs of diabetic retinopathy. *J Biomed Opt* **20 (6)**, 61106:1-13, **2015**. [10.1117/1.JBO.20.6.061106]

19. Sauer, L., Gensure, R. H., Hammer, M., and Bernstein, P. S. Fluorescence Lifetime Imaging Ophthalmoscopy: A Novel Way to Assess Macular Telangiectasia Type 2. *Ophthalmol. Retin.* **2 (6)**, 587–598, **2018**. [10.1016/j.oret.2017.10.008]

20. Remington, L. A. *Clinical anatomy of the visual system*. Elsevier, 2nd Ed., St. Louis, Missouri, USA, **2005**.

21. Lang, G. K., and Amann, J. *Ophthalmology: a short textbook*. Thieme, 1st Ed., Stuttgart, Germany, **2000**.

22. Nishida, T., and Saika, S. Cornea and Sclera: Anatomy and Physiology. in *Cornea - Fundamentals, Diagnosis and Management (Volume 1)* (eds. Krachmer, J. H., Mannis, M. J. & Holland, E. J.) Mosby/Elsevier, 3rd Ed., Maryland Heights, Missouri, USA, **2011**.

23. Bye, L., Modi, N., and Stanford, M. *Basic Sciences for Ophthalmology*. Oxford University Press, 1st Ed., Oxford, United Kingdom, **2013**.

24. Sanchez, I., Martin, R., Ussa, F., and Fernandez-Bueno, I. The parameters of the porcine eyeball. *Graefes Arch Clin Exp Ophthalmol* **249 (4)**, 475–482, **2011**. [10.1007/s00417-011-1617-9]

25. Faber, C., Scherfig, E., Prause, J. U., and Sørensen, K. E. Corneal thickness in pigs measured by ultrasound pachymetry in vivo. *Scand. J. Lab. Anim. Sci.* **35 (1)**, 39–43, **2008**.

26. Jay, L., Brocas, A., Singh, K., Kieffer, J.-C., Brunette, I., and Ozaki, T. Determination of porcine corneal layers with high spatial resolution by simultaneous second and

third harmonic generation microscopy. *Opt. Express* **16 (21)**, 16284–16293, **2008**. [10.1364/OE.16.016284]

27. Hahnel, C., Somodi, S., Weiss, D. G., and Guthoff, R. F. The keratocyte network of human cornea: a three-dimensional study using confocal laser scanning fluorescence microscopy. *Cornea* **19 (2)**, 185–193, **2000**.

28. Benedek, G. B. Theory of Transparency of the Eye. *Appl. Opt.* **10 (3)**, 459–473, **1971**. [10.1364/AO.10.000459]

29. Dua, H. S., Faraj, L. A., Said, D. G., Gray, T., and Lowe, J. Human corneal anatomy redefined: A novel pre-descemet's layer (Dua's Layer). *Ophthalmology* **120 (9)**, 1778–1785, **2013**. [10.1016/j.ophtha.2013.01.018]

30. Jester, J. V., Murphy, C. J., Winkler, M., Bergmanson, J. P. G., Brown, D., Steinert, R. F., and Mannis, M. J. Lessons in corneal structure and mechanics to guide the corneal surgeon. *Ophthalmology* **120 (9)**, 1715–1717, **2013**. [10.1016/j.ophtha.2013.07.004]

31. Nema, H., and Nitin, N. *Textbook of Ophthalmology*. Jaypee Brothers Medical Publishers, 5th Ed., New Delhi, India, **2008**. [10.1007/s13398-014-0173-7.2]

32. Müller, L. J., Marfurt, C. F., Kruse, F., and Tervo, T. M. T. Corneal nerves: Structure, contents and function. *Exp. Eye Res.* **76 (5)**, 521–542, **2003**. [10.1016/S0014-4835(03)00050-2]

33. Mártonyi, C. L. Slit Lamp Examination and Photography. in *Cornea - Fundamentals, Diagnosis and Management (Volume 1)* (eds. Krachmer, J., Mannis, M. & Holland, E.) Mosby/Elsevier, 3rd Ed., Maryland Heights, Missouri, USA, **2011**.

34. Ledford, J. K., and Sanders, V. N. *The Slit Lamp Primer*. SLACK Incorporated, 2nd Ed., Thorofare, New Jersey, USA, **2006**.

35. Gellrich, M.-M. *The Slit Lamp*. Springer Berlin Heidelberg, 1st Ed., Heidelberg, Germany, **2014**. [10.1007/978-3-642-39793-6]

36. Agarwal, S., Agarwal, A., Buratto, L., Apple, D. J., and Alió, J. L. *Textbook of Ophthalmology*. Lippincott Williams & Wilkins, 1st Ed., Michigan, USA, **2002**.

37. Maurice, D. M. Cellular Membrane Activity in the Corneal Endothelium of the Intact Eye. *Experientia* **24**, 1094–1095, **1968**.

38. Laing, R. A., Sandstrom, M. M., and Leibowitz, H. M. Clinical Specular Microscopy. *Arch Ophthalmol* **97**, 1714–1719, **1979**.

39. Benetz, B. A., Yee, R., Bidros, M., and Lass, J. Specular Microscopy. in *Cornea - Fundamentals, Diagnosis and Management (Volume 1)* (eds. Krachmer, J., Mannis, M. & Holland, E.) Mosby/Elsevier, 3rd Ed., Maryland Heights, Missouri, USA, **2011**.

40. Laing, R. A., Sandstrom, M. M., and Leibowitz, H. M. In vivo photomicrography of the corneal endothelium. *Arch. Ophthalmol. (Chicago, Ill. 1960)* **93 (2)**, 143–145, **1975**. [10.1001/archopht.1975.01010020149013]

41. Bourne, W. M., and Kaufman, H. E. Specular microscopy of human corneal endothelium in vivo. *Am. J. Ophthalmol.* **81 (3)**, 319–323, **1976**. [10.1016/0002-9394(76)90247-6]

42. Brown, N. Macrophotography of the anterior segment of the eye. *Br. J. Ophthalmol.* **54 (10)**, 697–701, **1970**. [10.1136/bjo.54.10.697]

43. Olsen, T. Non-contact specular microscopy of human corneal endothelium. *Acta Ophthalmol* **57 (6)**, 986–998, **1979**.

44. Minsky, M. Memoir on inventing the confocal scanning microscope. *Scanning* **10 (4)**, 128–138, **1988**. [10.1002/sca.4950100403]

45. Petroll, W. M., Cavanagh, H. D., and Jester, J. V. Confocal Microscopy. in *Cornea - Fundamentals, Diagnosis and Management (Volume 1)* (eds. Krachmer, J., Mannis, M. & Holland, E.) Mosby/Elsevier, 3rd Ed., Maryland Heights, Missouri, USA, **2011**.

46. Masters, B. R., and Böhnke, M. Confocal microscopy of the human cornea in vivo. in *Laser Scanning: Update 1* (ed. Sampaolesi, J. R.) Springer Netherlands, 2nd Ed., Dordrecht, Netherlands, **2001**. [10.1007/978-94-010-0322-3_3]

47. Guthoff, R. F., Baudouin, C., and Stave, J. *Atlas of Confocal Laser Scanning In-vivo Microscopy in Ophthalmology*. Springer Berlin Heidelberg, 1st Ed., Heidelberg, Germany, **2006**. [10.1007/3-540-32707-X]

48. Petran, M., Hadravsky, M., Egger, M. D., and Galambos, R. Tandem-scanning reflected-light microscope. *J. ot Opt. Soc. Am.* **58 (5)**, 661–664, **1968**. [10.1364/JOSA.58.000661]

49. Cavanagh, H. D., El-Agha, M. S., Petroll, W. M., and Jester, J. V. Specular Microscopy, Confocal Microscopy, and Ultrasound Biomicroscopy. *Cornea* **19 (5)**, 712–722, **2000**. [10.1097/00003226-200009000-00016]

50. Patel, D. V, and McGhee, C. N. Contemporary in vivo confocal microscopy of the living human cornea using white light and laser scanning techniques: a major review. *Clin. Experiment. Ophthalmol.* **35 (1)**, 71–88, **2007**. [10.1111/j.1442-9071.2007.01423.x]

51. Lagali, N., Bourghardt, B., Germundsson, J., Edén, U., Danyali, R., Rinaldo, M., and Fagerholm, P. Laser-Scanning in vivo Confocal Microscopy of the Cornea: Imaging and Analysis Methods for Preclinical and Clinical Applications. in *Confocal Laser Microscopy - Principles and Applications in Medicine, Biology, and the Food Sciences* (ed. Lagali, N.) InTech, 1st Ed., London, United Kingdom, **2013**. [10.5772/50821]

52. Masters, B. R., and Thaer, A. A. Real-time scanning slit confocal microscopy of the in vivo human cornea. *Appl. Opt.* **33 (4)**, 695–701, **1994**. [10.1364/AO.33.000695]

53. Lemp, M. A., Dilly, P. N., and Boyde, A. Tandem-Scanning (Confocal) Microscopy of the Full-Thickness Cornea. *Cornea* **4 (4)**, 205–209, **1986**.

54. Petran, M., Hadravsky, M., Benes, J., and Boyde, A. In vivo microscopy using the tandem scanning microscope. *Ann N Y Acad Sci* **483**, 440–447, **1986**.

55. Cavanagh, H. D., Jester, J. V, Essepian, J., Shields, W., and Lemp, M. A. Confocal microscopy of the living eye. *The CLAO journal:official publication of the Contact Lens Association of Ophthalmologists, Inc* **16 (1)**, 65–73, **1990**.

56. Tavakoli, M., Hossain, P., and Malik, R. A. Clinical applications of corneal confocal microscopy. *Clin Ophthalmol* **2 (2)**, 435–445, **2008**.

57. Radhakrishnan, S. Real-Time Optical Coherence Tomography of the Anterior Segment at 1310 nm. *Arch. Ophthalmol.* **119 (8)**, 1179, **2001**.

[10.1001/archopht.119.8.1179]

58. Huang, D., Swanson, E. a, Lin, C. P., Schuman, J. S., Stinson, W. G., Chang, W., Hee, M. R., Flotire, T., Gregory, K., Puliafito, C. a, and Fujimoto, J. G. Optical Coherence Tomography. *Science.* **254**, 1178–1181, **1991**. [10.1002/ccd.23385]

59. Fujimoto, J. G., and Drexler, W. Introduction to Optical Coherence Tomography. in *Optical Coherence Tomography: Technology and Application* (eds. Drexler, W. & Fujimoto, J. G.) Springer Science & Business Media, 1st Ed., Berlin, **2008**.

60. Heur, M., Li, Y., and Huang, D. Anterior Segment Optical Coherence Tomography. in *Cornea - Fundamentals, Diagnosis and Management (Volume 1)* (eds. Krachmer, J., Mannis, M. & Holland, E.) Mosby/Elsevier, 3rd Ed., Maryland Heights, Missouri, USA, **2011**.

61. Swanson, E. A., Izatt, J. A., Hee, M. R., Huang, D., Lin, C. P., Schuman, J. S., Puliafito, C. A., and Fujimoto, J. G. In vivo retinal imaging by optical coherence tomography. *Opt. Lett.* **18 (21)**, 1864–1866, **1993**. [10.1364/OL.18.001864]

62. Izatt, J. A. Micrometer-Scale Resolution Imaging of the Anterior Eye In Vivo With Optical Coherence Tomography. *Arch. Ophthalmol.* **112 (12)**, 1584–1589, **1994**. [10.1001/archopht.1994.01090240090031]

63. Huang, D., and Izatt, J. A. Physics and Fundamentals of Anterior Segment Optical Coherence Tomography. in *Anterior Segment Optical Coherence Tomography* (eds. Steinert, R. F. & Huang, D.) SLACK Incorporated, 1st Ed., Thorofare, New Jersey, USA, **2008**.

64. Denoyer, A., Labbé, A., and Baudouin, C. Anterior Segment OCT Imaging. in *Optical Coherence Tomography: A Clinical and Technical Update* (eds. Bernardes, R. & Cunha-Vaz, J.) Springer, 1st Ed., New York, USA, **2012**.

65. Yam, J. C. S., Chan, C. W. N., and Cheng, A. C. K. Corneal Collagen Cross-linking Demarcation Line Depth Assessed by Visante OCT After CXL for Keratoconus and Corneal Ectasia. *J. Refract. Surg.* **28 (7)**, 475–481, **2012**. [10.3928/1081597X-20120615-03]

66. Mazzotta, C. Qualitative Investigation of Corneal Changes after Accelerated Corneal Collagen Cross-linking (A-CXL) by In vivo Confocal Microscopy and Corneal OCT. *J. Clin. Exp. Ophthalmol.* **04 (06)**, 1–6, **2013**. [10.4172/2155-9570.1000313]

67. Kymionis, G. D., Tsoulnaras, K. I., Grentzelos, M. A., Plaka, A. D., Mikropoulos, D. G., Liakopoulos, D. A., Tsakalis, N. G., and Pallikaris, I. G. Corneal stroma demarcation line after standard and high-intensity collagen crosslinking determined with anterior segment optical coherence tomography. *J. Cataract Refract. Surg.* **40 (5)**, 736–740, **2014**. [10.1016/j.jcrs.2013.10.029]

68. Shapiro, B. L., Cortés, D. E., Chin, E. K., Li, J. Y., Werner, J. S., Redenbo, E., and Mannis, M. J. High-Resolution Spectral Domain Anterior Segment Optical Coherence Tomography in Type 1 Boston Keratoprosthesis. *Cornea* **32 (7)**, 951–955, **2013**. [10.1097/ICO.0b013e318285c8f4]

69. Li, H., Jhanji, V., Dorairaj, S., Liu, A., Lam, D. S., and Leung, C. K. Anterior Segment Optical Coherence Tomography and its Clinical Applications in Glaucoma. *Curr. J. Glaucoma Pract.* **6**, 68–74, **2012**. [10.5005/jp-journals-10008-1109]

70. Pavlin, C. J., and Foster, F. S. High-Resolution Ultrasound. in *Cornea - Fundamentals, Diagnosis and Management (Volume 1)* (eds. Krachmer, J., Mannis, M. & Holland, E.) Mosby/Elsevier, 3rd Ed., Maryland Heights, Missouri, USA, **2011**.

71. Martinez, C. E., and Klyce, S. D. Keratometry and Topography. in *Cornea - Fundamentals, Diagnosis and Management (Volume 1)* (eds. Krachmer, J., Mannis, M. & Holland, E.) Mosby/Elsevier, 3rd Ed., Maryland Heights, Missouri, USA, **2011**.

72. Faulkner, W. J., and Varley, G. A. Corneal Diagnostic Techniques. in *Cornea - Fundamentals, Diagnosis and Management (Volume 1)* (eds. Krachmer, J., Mannis, M. & Holland, E.) Mosby/Elsevier, 3rd Ed., Maryland Heights, Missouri, USA, **2011**.

73. Wheeldon, C. E., and McGhee, C. N. J. Corneal Tomography and Anterior Chamber Imaging. in *Corneal surgery : theory, technique and tissue* (eds. Brightbill, F. S., McDonnell, P. J., McGhee, C. N. J., Farjo, A. A. & Serdarevic, O.) Mosby Elsevier Health Sciences, 4th Ed., Missouri, USA, **2009**.

74. Anthony, N., Guo, P., and Berland, K. Principles of Fluorescence for Quantitative

Fluorescence Microscopy. in *FLIM Microscopy in Biology and Medicine* (eds. Periasamy, A. & Clegg, R.) CRC Press, 1st Ed., Boca Raton, Florida, USA, **2009**.

75. Göppert-Mayer, M. Uber Elementarakte mit zwei Quantensprüngen. *Ann. Phys.* **401 (3)**, 273–294, **1931**. [10.1002/andp.19314010303]

76. Lakowicz, J. R. *Principles of Fluorescence Spectroscopy*. Springer, 3rd Ed., New York, USA, **2007**.

77. Maiman, T. H. Stimulated Optical Radiation in Ruby. *Nature* **187 (4736)**, 493–494, **1960**. [10.1038/187493a0]

78. Kaiser, W., and Garrett, C. Two-Photon Excitation in CaF2:Eu2+. *Phys. Rev. Lett.* **7 (6)**, 229–231, **1961**. [10.1103/PhysRevLett.7.229]

79. Denk, W., Strickler, J., and Webb, W. Two-photon laser scanning fluorescence microscopy. *Science.* **248 (4951)**, 73–76, **1990**. [10.1126/science.2321027]

80. So, P. T. C. C., Dong, C. Y., Masters, B. R., and Berland, K. M. Two-photon Excitation Fluorescence Microscopy. in *Biomedical Photonics Handbook* (ed. Vo-Dinh, T.) **2 (1)**, 399–429, CRC Press, 1st Ed., Boca Raton, Florida, USA, **2003**. [10.1146/annurev.bioeng.2.1.399]

81. Tkachenko, N. V. *Optical Spectroscopy: Methods and Instrumentations*. Elsevier Science, 1st Ed., London, United Kingdom, **2006**. [10.1887/0750303468/b293c8]

82. Vo-Dinh, T. *Biomedical Photonics Handbook*. CRC Press, 1st Ed., Boca Raton, Florida, USA, **2003**.

83. Huang, S., Heikal, A. A., and Webb, W. W. Two-photon fluorescence spectroscopy and microscopy of NAD(P)H and flavoprotein. *Biophys J* **82 (5)**, 2811–2825, **2002**. [10.1016/s0006-3495(02)75621-x]

84. König, K., and Uchugonova, A. Multiphoton Fluorescence Lifetime Imaging at the Dawn of Clinical Application. in *FLIM microscopy in biology and medicine* (eds. Periasamy, A. & Clegg, R.) CRC Press, 1st Ed., Boca Raton, Florida, USA, **2009**.

85. Diaspro, A., and Sheppard, C. J. R. Two-Photon Microscopy: Basic Principles and Architectures. in *Confocal and two-photon microscopy : foundations, applications,*

*and advances* (ed. Diaspro, A.) 567, Wiley-Liss, 1st Ed., Hoboken, New Jersey, USA, **2001**.

86. Gauderon, R., Lukins, P. B., and Sheppard, C. J. Optimization of second-harmonic generation microscopy. *Micron* **32 (7)**, 691–700, **2001**. [10.1016/S0968-4328(00)00066-4]

87. Theodossiou, T. A., Thrasivoulou, C., Ekwobi, C., and Becker, D. L. Second harmonic generation confocal microscopy of collagen type I from rat tendon cryosections. *Biophys J* **91 (12)**, 4665–4677, **2006**. [10.1529/biophysj.106.093740]

88. Tian, L., Qu, J., Guo, Z., Jin, Y., Meng, Y., and Deng, X. Microscopic second-harmonic generation emission direction in fibrillous collagen type I by quasi-phase-matching theory. *J. Appl. Phys.* **108 (5)**, 54701–54709, **2010**. [10.1063/1.3474667]

89. Campagnola, P. J., and Dong, C. Y. Second harmonic generation microscopy: principles and applications to disease diagnosis. *Laser Photon. Rev.* **5 (1)**, 13–26, **2011**. [10.1002/lpor.200910024]

90. Franken, P. A., Hill, A. E., Peters, C. W., and Weinreich, G. Generation of optical harmonics. *Phys. Rev. Lett.* **7 (4)**, 118–119, **1961**. [10.1103/PhysRevLett.7.118]

91. Fine, S., and Hansen, W. P. Optical second harmonic generation in biological systems. *Appl. Opt.* **10 (10)**, 2350–2353, **1971**. [10.1364/AO.10.002350]

92. Gannaway, J. N., and Sheppard, C. J. R. Second-harmonic imaging in the scanning optical microscope. *Opt. Quantum Electron.* **10 (5)**, 435–439, **1978**. [10.1007/BF00620308]

93. Freund, I., and Deutsch, M. Second-harmonic microscopy of biological tissue. *Opt. Lett.* **11 (2)**, 94–96, **1986**. [10.1364/OL.11.000094]

94. Cox, G., Kable, E., Jones, A., Fraser, I., Manconi, F., and Gorrell, M. D. 3-Dimensional imaging of collagen using second harmonic generation. *J. Struct. Biol.* **141 (1)**, 53–62, **2003**. [10.1016/S1047-8477(02)00576-2]

95. New, G. *Introduction to Nonlinear Optics*. Cambridge University Press, 1st Ed., Cambridge, United Kingdom, **2011**. [10.1017/CBO9780511975851]

96. Boyd, R. *Nonlinear Optics*. Academic Press, 3rd Ed., Massachusetts, USA, **2008**.

97. Sutherland, R. L. *Handbook of Nonlinear Optics*. CRC Press, 2nd Ed., Boca Raton, Florida, USA, **2003**.

98. Campagnola, P. J. Second-Harmonic Generation Imaging Microscopy of Structural Protein Arrays in Tissue. in *Handbook of Biomedical Nonlinear Optical Microscopy* (eds. Masters, B. R. & So, P.) Oxford University Press, 1st Ed., Oxford, United Kingdom, **2008**.

99. Cicchi, R., Sacconi, L., Vanzi, F., and Pavone, F. S. How to build and SHG Apparatus. in *Second Harmonic Generation Imaging: Series in Cellular and Clinical Imaging* (eds. Pavone, F. S. & Campagnola, P. J.) CRC Press, 1st Ed., Boca Raton, Florida, USA, **2008**.

100. Campagnola, P. J., Millard, A. C., Terasaki, M., Hoppe, P. E., Malone, C. J., and Mohler, W. A. Three-Dimensional High-Resolution Second-Harmonic Generation Imaging of Endogenous Structural Proteins in Biological Tissues. *Biophys. J.* **82 (1)**, 493–508, **2002**. [10.1016/S0006-3495(02)75414-3]

101. Kim, B.-M., Eichler, J., and Da Silva, L. B. Frequency doubling of ultrashort laser pulses in biological tissues. *Appl. Opt.* **38 (34)**, 7145, **1999**. [10.1364/AO.38.007145]

102. Krueger, A. Ultrafast lasers in biophotonics. in *Multiphoton Microscopy and Fluorescence Lifetime Imaging* (ed. König, K.) De Gruyter, 1st Ed., Berlin, Germany, **2018**. [10.1515/9783110429985-006]

103. Csele, M. *Fundamentals of Light Sources and Lasers*. John Wiley & Sons, 1st Ed., Hoboken, New Jersey, USA, **2011**.

104. Zdybel, M., Pilawa, B., and Krzeszewska-Zarb, A. Lasers in Ophthalmology. in *Advances in Ophthalmology* (ed. Rumelt, S.) InTech, 1st Ed., London, United Kingdom, **2012**.

105. Zaret, M. M., Breinin, G. M., Schmidt, H., Ripps, H., Siegel, I. M., and Solon, L. R. Ocular lesions produced by an optical maser (laser). *Science.* **134 (3489)**, 1525–1526, **1961**.

106. Koester, J., Snitzer, E., Campbell, C. J., and Rittler, M. C. Program of the 1962 Spring Meeting of the Optical Society of America, Incorporated. *J. Opt. Soc. Am.* **52 (5)**, 588–610, **1962**. [10.1364/JOSA.52.000588]

107. Apolonskiy, A. *Femtosecond Ti:sapphire laser*. LMU München, Praktikum für fortgeschrittene Physikstudenten, **2013**.

108. Girkin, J. Laser Sources for Nonlinear Microscopy. in *Handbook of Biomedical Nonlinear Optical Microscopy* (eds. Masters, B. R. & So, P. T. C.) Oxford University Press, 1st Ed., Oxford, United Kingdom, **2008**.

109. König, K. Femtosecond laser nanoprocessing: Applications in Biology and Medicine. in *Multiphoton Microscopy and Fluorescence Lifetime Imaging* (ed. König, K.) De Gruyter, 1st Ed., Berlin, Germany, **2018**. [10.1515/9783110429985-013]

110. Silfvast, W. T. *Laser Fundamentals*. Cambridge University Press, 1st Ed., Cambridge, United Kingdom, **2004**.

111. Small, E. W. Laser Sources and Microchannel Plate Detectors for Pulse Fluorometry. in *Topics in Fluorescence Spectrosocopy - Volume 1: Techniques* (ed. Lakowickz, J. R.) Kluwer Academic Publishers, 1st Ed., Dordrecht, Netherlands, **2002**.

112. Fermann, M. E., Galvanauskas, A., and Sucha, G. *Ultrafast Lasers: Technology and Applications*. CRC Press, 1st Ed., Boca Raton, Florida, USA, **2002**.

113. Herrmann, J. Theory of Kerr-lens mode locking: role of self-focusing and radially varying gain. *J. Opt. Soc. Am. B* **11 (3)**, 498–512, **1994**. [10.1364/JOSAB.11.000498]

114. Herman, P., Lin, H.-J., and Lakowicz, J. R. Lifetime-Based Imaging. in *Biomedical Photonics Handbook* (ed. Vo-Dinh, T.) CRC Press, 1st Ed., Boca Raton, Florida, USA, Florida, **2003**.

115. Clegg, R. Fluorescence Lifetime-Resolved Imaging — What, Why, How - A Prologue. in *FLIM microscopy in biology and medicine* (eds. Periasamy, A. & Clegg, R.) CRC Press, 1st Ed., Boca Raton, Florida, USA, **2009**.

116. Spring, B. Q., and Clegg, R. Frequency-Domain FLIM. in *FLIM microscopy in biology and medicine* (eds. Periasamy, A. & Clegg, R.) CRC Press, 1st Ed., Boca Raton,

Florida, USA, **2009**.

117. Becker, W. Introduction to Multi-dimensional TCSPC. in *Advanced Time-Correlated Single Photon Counting Applications* (ed. Becker, W.) Springer International Publishing, 1st Ed., New York, USA, **2015**. [10.1007/978-3-319-14929-5]

118. Becker, W., Bergmann, A., Schweitzer, D., and Hammer, M. Time- and Wavelength-Resolved Autofluorescence Detection by Multi-Dimensional TCSPC. in *Diagnostic Optical Spectroscopy in Biomedicine III* (ed. Mycek, A.) ThE2, Proc. SPIE 5862 (OSA), **2005**. [10.1364/ECBO.2005.ThE2]

119. Becker, W., and Bergmann, A. Lifetime-Resolved Imaging in Nonlinear Microscopy. in *Handbook of Biomedical Nonlinear Optical Microscopy* (eds. Masters, B. R. & So, P.) Oxford University Press, 1st Ed., Oxford, United Kingdom, **2008**.

120. Becker, W., Bergmann, A., Hink, M. A., König, K., Benndorf, K., and Biskup, C. Fluorescence lifetime imaging by time-correlated single-photon counting. *Microsc Res Tech* **63 (1)**, 58–66, **2004**. [10.1002/jemt.10421]

121. Schweitzer, D., and Hammer, M. Fluorescence Lifetime Imaging in Ophthalmology. in *Advanced Time-Correlated Single Photon Counting Applications* (ed. Becker, W.) Springer International Publishing, 1st Ed., New York, USA, **2015**. [10.1007/978-3-319-14929-5]

122. Georgakoudi, I., and Quinn, K. P. Optical imaging using endogenous contrast to assess metabolic state. *Annu Rev Biomed Eng* **14**, 351–367, **2012**. [10.1146/annurev-bioeng-071811-150108]

123. Mason, W. T. *Fluorescent and Luminescent Probes for Biological Activity: A Practical Guide to Technology for Quantitative Real-Time Analysis*. Elsevier Science, 2nd Ed., London, United Kingdom, **1999**.

124. Karp, G. Aerobic Respiration and Mitochondrion. in *Cell and Molecular Biology: Concepts and Experiments* (ed. Karp, G.) 173–205, John Wiley & Sons, 6th Ed., Hoboken, New Jersey, USA, **2009**.

125. Skala, M. C., Riching, K. M., Gendron-Fitzpatrick, A., Eickhoff, J., Eliceiri, K. W.,

White, J. G., and Ramanujam, N. In vivo multiphoton microscopy of NADH and FAD redox states, fluorescence lifetimes, and cellular morphology in precancerous epithelia. *Proc Natl Acad Sci U S A* **104 (49)**, 19494–19499, **2007**. [10.1073/pnas.0708425104]

126. König, K., Raphael, A. P., Lin, L., Grice, J. E., Soyer, H. P., Breunig, H. G., Roberts, M. S., and Prow, T. W. Applications of multiphoton tomographs and femtosecond laser nanoprocessing microscopes in drug delivery research. *Adv Drug Deliv Rev* **63 (4–5)**, 388–404, **2011**. [10.1016/j.addr.2011.03.002]

127. Palero, J. A., Bader, A. N., de Bruijn, H. S., der Ploeg van den Heuvel, A., Sterenborg, H. J., and Gerritsen, H. C. In vivo monitoring of protein-bound and free NADH during ischemia by nonlinear spectral imaging microscopy. *Biomed Opt Express* **2 (5)**, 1030–1039, **2011**. [10.1364/boe.2.001030]

128. Lakowicz, J. R., Szmacinski, H., Nowaczyk, K., and Johnson, M. L. Fluorescence lifetime imaging of free and protein-bound NADH. *Proc Natl Acad Sci U S A* **89 (4)**, 1271–1275, **1992**.

129. McCance, K. L., Huether, S. E., Geneser, F., Shoulders, M. D., Raines, R. T., Genovese, F., Manresa, A. a, … Mauer, S. M. Collagen Structure and Stability. *PLoS One* **78 (3)**, 929–958, **2010**. [10.1146/annurev.biochem.77.032207.120833.COLLAGEN]

130. Yeh, A. T., Choi, B., Nelson, J. S., and Tromberg, B. J. Reversible dissociation of collagen in tissues. *J Invest Dermatol* **121 (6)**, 1332–1335, **2003**. [10.1046/j.1523-1747.2003.12634.x]

131. Shi, L., Lu, L., Harvey, G., Harvey, T., Rodríguez-Contreras, A., and Alfano, R. R. Label-Free Fluorescence Spectroscopy for Detecting Key Biomolecules in Brain Tissue from a Mouse Model of Alzheimer's Disease. *Sci. Rep.* **7 (1)**, 1–7, **2017**. [10.1038/s41598-017-02673-5]

132. Sekar, S. K. V., Bargigia, I., Mora, A. D., Taroni, P., Ruggeri, A., Tosi, A., Pifferi, A., and Farina, A. Diffuse optical characterization of collagen absorption from 500 to 1700 nm. *J. Biomed. Opt.* **22 (1)**, 015006:1-6, **2017**. [10.1117/1.JBO.22.1.015006]

133. Zheng, W., Wu, Y., Li, D., and Qu, J. Y. Autofluorescence of epithelial tissue: single-

photon versus two-photon excitation. *J Biomed Opt* **13 (5)**, 54010:1-8, **2008**. [10.1117/1.2975866]

134. Lutz, V., Sattler, M., Gallinat, S., Wenck, H., Poertner, R., and Fischer, F. Characterization of fibrillar collagen types using multi-dimensional multiphoton laser scanning microscopy. *Int. J. Cosmet. Sci.* **34 (2)**, 209–215, **2012**. [10.1111/j.1468-2494.2012.00705.x]

135. König, K. Clinical multiphoton tomography. *J. Biophotonics* **1 (1)**, 13–23, **2008**. [10.1002/jbio.200710022]

136. Shirshin, E. A., Gurfinkel, Y. I., Priezzhev, A. V., Fadeev, V. V., Lademann, J., and Darvin, M. E. Two-photon autofluorescence lifetime imaging of human skin papillary dermis in vivo: Assessment of blood capillaries and structural proteins localization. *Sci. Rep.* **7 (1)**, 1–10, **2017**. [10.1038/s41598-017-01238-w]

137. Bianchini, P., and Diaspro, A. Three-dimensional (3D) backward and forward second harmonic generation (SHG) microscopy of biological tissues. *J. Biophotonics* **1 (6)**, 443–450, **2008**. [10.1002/jbio.200810060]

138. Han, M., Giese, G., and Bille, J. F. Second harmonic generation imaging of collagen fibrils in cornea and sclera. *Opt. Express* **13 (15)**, 5791, **2005**. [10.1364/OPEX.13.005791]

139. Chen, X., Nadiarynkh, O., Plotnikov, S., and Campagnola, P. J. Second harmonic generation microscopy for quantitative analysis of collagen fibrillar structure. *Nat. Protoc.* **7 (4)**, 654–669, **2012**. [10.1038/nprot.2012.009]

140. Williams, R. M., Zipfel, W. R., and Webb, W. W. Interpreting Second-Harmonic Generation Images of Collagen I Fibrils. *Biophys. J.* **88 (2)**, 1377–1386, **2005**. [10.1529/biophysj.104.047308]

141. Chance, B., and Lieberman, M. Intrinsic fluorescence emission from the cornea at low temperatures: evidence of mitochondrial signals and their differing redox states in epithelial and endothelial sides. *Exp. Eye Res.* **26 (1)**, 111–117, **1978**. [10.1016/0014-4835(78)90159-8]

142. Nissen, P., Lieberman, M., Fischbarg, J., and Chance, B. Altered redox states in corneal epithelium and endothelium: NADH fluorescence in rat and rabbit ocular tissue. *Exp Eye Res* **30 (6)**, 691–697, **1980**. [http://dx.doi.org/10.1016/0014-4835(80)90067-6]

143. Laing, R. A., Fischbarg, J., and Chance, B. Noninvasive measurements of pyridine nucleotide fluorescence from the cornea. *Invest Ophthalmol Vis Sci* **19 (1)**, 96–102, **1980**.

144. Masters, B. R. Noninvasive redox fluorometry: how light can be used to monitor alterations of corneal mitochondrial function. *Curr Eye Res* **3 (1)**, 23–26, **1984**.

145. Shimazaki, J., Tsubota, K., Hayashi, K., Kenyon, K. R., and Laing, R. A. Distribution of autofluorescence in the rabbit corneal epithelium. *Ophthalmic Res* **25 (4)**, 220–225, **1993**.

146. Tsubota, K., Laing, R. A., Chiba, K., Hanninen, L. A., and Kenyon, K. R. Noninvasive metabolic analysis of preserved rabbit cornea. *Arch Ophthalmol* **106 (12)**, 1713–1717, **1988**.

147. Tsubota, K., and Laing, R. A. Metabolic changes in the corneal epithelium resulting from hard contact lens wear. *Cornea* **11 (2)**, 121–126, **1992**.

148. Stolwijk, T. R., van Best, J. A., Boot, J. P., and Oosterhuis, J. A. Corneal autofluorescence in diabetic and penetrating keratoplasty patients as measured by fluorophotometry. *Exp Eye Res* **51 (4)**, 403–409, **1990**.

149. Van Schaik, H. J., Coppens, J., Van den Berg, T. J., and Van Best, J. A. Autofluorescence distribution along the corneal axis in diabetic and healthy humans. *Exp Eye Res* **69 (5)**, 505–510, **1999**. [10.1006/exer.1999.0733]

150. Masters, B. R., Kriete, A., and Kukulies, J. Ultraviolet confocal fluorescence microscopy of the in vitro cornea: redox metabolic imaging. *Appl Opt* **32 (4)**, 592–596, **1993**. [10.1364/AO.32.000592]

151. Piston, D. W., Masters, B. R., and Webb, W. W. Three-dimensionally resolved NAD(P)H cellular metabolic redox imaging of the in situ cornea with two-photon

excitation laser scanning microscopy. *J. Microsc.* **178 (1)**, 20–27, **1995**. [10.1111/j.1365-2818.1995.tb03576.x]

152. Hochheimer, B. F. Second harmonic light generation in the rabbit cornea. *Appl. Opt.* **21 (8)**, 1516–1518, **1982**.

153. König, K., Krauss, O., and Riemann, I. Intratissue surgery with 80 MHz nanojoule femtosecond laser pulses in the near infrared. *Opt. Express* **10 (3)**, 171–176, **2002**. [10.1364/OE.10.000171]

154. Yeh, A. T., Nassif, N., Zoumi, A., and Tromberg, B. J. Selective corneal imaging using combined second-harmonic generation and two-photon excited fluorescence. *Opt. Lett.* **27 (23)**, 2082–2084, **2002**. [10.1364/OL.27.002082]

155. König, K. High-resolution multiphoton imaging and nanosurgery of the cornea using femtosecond laser pulses. in *Lasers in Ophthalmology: Basic, Diagnostic, and Surgical Aspects : a Review* (eds. Fankhauser, F. & Kwasniewska, S.) Kugler Publications, 1st Ed., Amsterdam, **2003**.

156. Teng, S. W., Tan, H. Y., Peng, J. L., Lin, H. H., Kim, K. H., Lo, W., Sun, Y., Lin, W. C., Lin, S. J., Jee, S. H., So, P. T., and Dong, C. Y. Multiphoton autofluorescence and second-harmonic generation imaging of the ex vivo porcine eye. *Invest Ophthalmol Vis Sci* **47 (3)**, 1216–1224, **2006**. [10.1167/iovs.04-1520]

157. Vohnsen, B., and Artal, P. Second-harmonic microscopy of ex vivo porcine corneas. *J Microsc* **232 (1)**, 158–163, **2008**. [10.1111/j.1365-2818.2008.02086.x]

158. Masihzadeh, O., Lei, T. C., Ammar, D. A., Kahook, M. Y., and Gibson, E. A. A multiphoton microscope platform for imaging the mouse eye. *Mol. Vis.* **18**, 1840–1848, **2012**.

159. Aptel, F., Olivier, N., Deniset-Besseau, A., Legeais, J. M., Plamann, K., Schanne-Klein, M. C., and Beaurepaire, E. Multimodal nonlinear imaging of the human cornea. *Invest Ophthalmol Vis Sci* **51 (5)**, 2459–2465, **2010**. [10.1167/iovs.09-4586]

160. König, K., Batista, A., Breunig, H. G., and Seitz, B. Multiphotonen-Tomographie der humanen Kornea. *Ophthalmologische Nachrichten Special Bilddiagnostik* **09-2014**,

14–15, **2014**.

161. König, K., Wang, B., Krauss, O., Riemann, I., Schubert, H., Kirste, S., and Fischer, P. First in vivo animal studies on intraocular nanosurgery and multiphoton tomography with low-energy 80-MHz near-infrared femtosecond laser pulses. in *Proc. SPIE* (eds. Manns, F., Soderberg, P. G. & Ho, A.) **5314**, 262–269, **2004**. [10.1117/12.528287]

162. Wang, B., Halbhuber, K.-J., Riemann, I., and König, K. In-vivo corneal nonlinear optical tomography based on second harmonic and multiphoton autofluorescence imaging induced by near-infrared femtosecond lasers with rabbits. in *Proc. SPIE* (eds. Chatard, J.-P. & Dennis, P. N. J.) **5964**, 59640O:1-11, **2005**. [10.1117/12.622204]

163. Wang, B. G., and Halbhuber, K. J. Corneal multiphoton microscopy and intratissue optical nanosurgery by nanojoule femtosecond near-infrared pulsed lasers. *Ann Anat* **188 (5)**, 395–409, **2006**. [10.1016/j.aanat.2006.02.006]

164. Robertson, D. M., Rogers, N. A., Petroll, W. M., and Zhu, M. Second harmonic generation imaging of corneal stroma after infection by Pseudomonas aeruginosa. *Sci. Rep.* **7**, 46116:1-10, **2017**. [10.1038/srep46116]

165. Steven, P., Bock, F., Hüttmann, G., and Cursiefen, C. Intravital two-photon microscopy of immune cell dynamics in corneal lymphatic vessels. *PLoS One* **6 (10)**, e26253:1-9, **2011**. [10.1371/journal.pone.0026253]

166. Latour, G., Gusachenko, I., Kowalczuk, L., Lamarre, I., and Schanne-Klein, M.-C. In vivo structural imaging of the cornea by polarization-resolved second harmonic microscopy. *Biomed. Opt. Express* **3 (1)**, 1–15, **2012**. [10.1364/BOE.3.000001]

167. Mega, Y., Robitaille, M., Zareian, R., McLean, J., Ruberti, J., and DiMarzio, C. Quantification of lamellar orientation in corneal collagen using second harmonic generation images. *Opt Lett* **37 (16)**, 3312–3314, **2012**. [10.1364/ol.37.003312]

168. Lo, W., Chen, W. L., Hsueh, C. M., Ghazaryan, A. A., Chen, S. J., Hui-Kang Ma, D., Dong, C. Y., and Tan, H. Y. Fast fourier transform-based analysis of second-harmonic generation image in keratoconic cornea. *Investig. Ophthalmol. Vis. Sci.* **53 (7)**,

3501–3507, **2012**. [10.1167/iovs.10-6697]

169. Mega, Y., McLean, J., Zareian, R., Karasek, S., Lai, Z., and DiMarzio, C. The arrangement of fibrous collagen in cornea using second harmonic generation (SHG) microscopy. in *Proc. SPIE* (eds. Periasamy, A., König, K. & So, P. T. C.) **8588**, 85881N:1-6, **2013**. [10.1117/12.2001551]

170. Tan, H. Y., Chang, Y. L., Lo, W., Hsueh, C. M., Chen, W. L., Ghazaryan, A. A., Hu, P. S., Young, T. H., Chen, S. J., and Dong, C. Y. Characterizing the morphologic changes in collagen crosslinked-treated corneas by Fourier transform-second harmonic generation imaging. *J Cataract Refract Surg* **39 (5)**, 779–788, **2013**. [10.1016/j.jcrs.2012.11.036]

171. Lee, S.-L., Chen, Y.-F., and Dong, C.-Y. Probing superstructure of chicken corneal stroma by Fourier transform second harmonic generation microscopy. in *Proc. SPIE* (eds. Manns, F., Söderberg, P. G. & Ho, A.) **10045 (1)**, 100451U:1-4, **2017**. [10.1117/12.2254942]

172. Zhuo, S., Chen, J., Wu, G., Xie, S., Zheng, L., Jiang, X., and Zhu, X. Quantitatively linking collagen alteration and epithelial tumor progression by second harmonic generation microscopy. *Appl. Phys. Lett.* **96 (21)**, 94–97, **2010**. [10.1063/1.3441337]

173. Cicchi, R., Kapsokalyvas, D., De Giorgi, V., Maio, V., Van Wiechen, A., Massi, D., Lotti, T., and Pavone, F. S. Scoring of collagen organization in healthy and diseased human dermis by multiphoton microscopy. *J. Biophotonics* **3 (1–2)**, 34–43, **2010**. [10.1002/jbio.200910062]

174. Mercatelli, R., Ratto, F., Rossi, F., Tatini, F., Menabuoni, L., Malandrini, A., Nicoletti, R., Pini, R., Pavone, F. S., and Cicchi, R. Three-dimensional mapping of the orientation of collagen corneal lamellae in healthy and keratoconic human corneas using SHG microscopy. *J. Biophotonics* **83 (1)**, 75–83, **2016**. [10.1002/jbio.201600122]

175. Breunig, H. G., Batista, A., Uchugonova, A., and König, K. Motionless polarization-resolved second harmonic generation imaging of corneal collagen. in *Proc. SPIE* (eds. Periasamy, A., So, P. T. C. & König, K.) **9329**, 93292P:1-6, **2015**.

[10.1117/12.2078701]

176. Ávila, F. J., del Barco, O., and Bueno, J. M. Polarization response of second-harmonic images for different collagen spatial distributions. *J. Biomed. Opt.* **21 (6)**, 066015, **2016**. [10.1117/1.JBO.21.6.066015]

177. Yakovlev, D. D., Shvachkina, M. E., Sherman, M. M., Spivak, A. V., Pravdin, A. B., and Yakovlev, D. A. Quantitative mapping of collagen fiber alignment in thick tissue samples using transmission polarized-light microscopy. *J. Biomed. Opt.* **21 (7)**, 071111, **2016**. [10.1117/1.JBO.21.7.071111]

178. Kamma-Lorger, C. S., Boote, C., Hayes, S., Moger, J., Burghammer, M., Knupp, C., Quantock, A. J., Sorensen, T., Di Cola, E., White, N., Young, R. D., and Meek, K. M. Collagen and mature elastic fibre organisation as a function of depth in the human cornea and limbus. *J. Struct. Biol.* **169 (3)**, 424–430, **2010**. [10.1016/j.jsb.2009.11.004]

179. Park, C. Y., Lee, J. K., and Chuck, R. S. Second harmonic generation imaging analysis of collagen arrangement in human cornea. *Investig. Ophthalmol. Vis. Sci.* **56 (9)**, 5622–5629, **2015**. [10.1167/iovs.15-17129]

180. Park, C. Y., Lee, J. K., Zhang, C., and Chuck, R. S. New details of the human corneal limbus revealed with second harmonic generation imaging. *Investig. Ophthalmol. Vis. Sci.* **56 (10)**, 6058–6066, **2015**. [10.1167/iovs.15-16783]

181. Marando, C. M., Park, C. Y., Liao, J. A., Lee, J. K., and Chuck, R. S. Revisiting the Cornea and Trabecular Meshwork Junction With 2-Photon Excitation Fluorescence Microscopy. *Cornea* **36 (6)**, 704–711, **2017**. [10.1097/ICO.0000000000001178]

182. Lombardo, M., Parekh, M., Serrao, S., Ruzza, A., Ferrari, S., and Lombardo, G. Two-photon optical microscopy imaging of endothelial keratoplasty grafts. *Graefe's Arch. Clin. Exp. Ophthalmol.* **255 (3)**, 575–582, **2017**. [10.1007/s00417-016-3543-3]

183. Tan, H.-Y., Sun, Y., Lo, W., Teng, S.-W., Wu, R.-J., Jee, S.-H., Lin, W.-C., Hsiao, C.-H., Lin, H.-C., Chen, Y.-F., Ma, D. H.-K., Huang, S. C.-M., Lin, S.-J., and Dong, C.-Y. Multiphoton fluorescence and second harmonic generation microscopy for imaging infectious keratitis. *J. Biomed. Opt.* **12 (2)**, 024013:1-8, **2007**. [10.1117/1.2717133]

184. Hsueh, C. M., Lo, W., Chen, W. L., Hovhannisyan, V. A., Liu, G. Y., Wang, S. S., Tan, H. Y., and Dong, C. Y. Structural characterization of edematous corneas by forward and backward second harmonic generation imaging. *Biophys J* **97 (4)**, 1198–1205, **2009**. [10.1016/j.bpj.2009.05.040]

185. Latour, G., Kowalczuk, L., Savoldelli, M., Bourges, J. L., Plamann, K., Behar-Cohen, F., and Schanne-Klein, M. C. Hyperglycemia-induced abnormalities in rat and human corneas: the potential of second harmonic generation microscopy. *PLoS One* **7 (11)**, e48388:1-11, **2012**. [10.1371/journal.pone.0048388]

186. Tan, H. Y., Sun, Y., Lo, W., Lin, S. J., Hsiao, C. H., Chen, Y. F., Huang, S. C. M., Lin, W. C., Jee, S. H., Yu, H. S., and Dong, C. Y. Multiphoton fluorescence and second harmonic generation imaging of the structural alterations in keratoconus ex vivo. *Investig. Ophthalmol. Vis. Sci.* **47 (12)**, 5251–5259, **2006**. [10.1167/iovs.06-0386]

187. Morishige, N., Shin-Gyou-Uchi, R., Azumi, H., Ohta, H., Morita, Y., Yamada, N., Kimura, K., Takahara, A., and Sonoda, K. H. Quantitative analysis of collagen lamellae in the normal and keratoconic human cornea by second harmonic generation imaging microscopy. *Investig. Ophthalmol. Vis. Sci.* **55 (12)**, 8377–8385, **2014**. [10.1167/iovs.14-15348]

188. Morishige, N., Wahlert, A. J., Kenney, M. C., Brown, D. J., Kawamoto, K., Chikama, T., Nishida, T., and Jester, J. V. Second-harmonic imaging microscopy of normal human and keratoconus cornea. *Invest Ophthalmol Vis Sci* **48 (3)**, 1087–1094, **2007**. [10.1167/iovs.06-1177]

189. Bueno, J. M., Gualda, E. J., Giakoumaki, A., Perez-Merino, P., Marcos, S., and Artal, P. Multiphoton microscopy of ex vivo corneas after collagen cross-linking. *Invest Ophthalmol Vis Sci* **52 (8)**, 5325–5331, **2011**. [10.1167/iovs.11-7184]

190. McQuaid, R., Li, J., Cummings, A., Mrochen, M., and Vohnsen, B. Second-harmonic reflection imaging of normal and accelerated corneal crosslinking using porcine corneas and the role of intraocular pressure. *Cornea* **33 (2)**, 125–130, **2014**. [10.1097/ico.0000000000000015]

191. Mercatelli, R., Ratto, F., Tatini, F., Rossi, F., Menabuoni, L., Nicoletti, R., Pini, R.,

Pavone, F. S., and Cicchi, R. Characterization of the lamellar rearrangement induced by cross-linking treatment in keratoconic corneal samples imaged by SHG microscopy. in *Proc. SPIE* (eds. Manns, F., Söderberg, P. G. & Ho, A.) **10045**, 100450L:1-6, **2017**. [10.1117/12.2252127]

192. Zyablitskaya, M., Takaoka, A., Munteanu, E. L., Nagasaki, T., Trokel, S. L., and Paik, D. C. Evaluation of Therapeutic Tissue Crosslinking (TXL) for Myopia Using Second Harmonic Generation Signal Microscopy in Rabbit Sclera. *Investig. Opthalmology Vis. Sci.* **58 (1)**, 21–29, **2017**. [10.1167/iovs.16-20241]

193. Hovakimyan, M., Guthoff, R. F., and Stachs, O. Collagen Cross-Linking: Current Status and Future Directions. *J. Ophthalmol.* **2012**, 406850:1-12, **2012**. [10.1155/2012/406850]

194. Zhang, X., Tao, X., Zhang, J., Li, Z., Xu, Y., Wang, Y., Zhang, C., and Mu, G. A Review of Collagen Cross-Linking in Cornea and Sclera. *J. Ophthalmol.* **2015**, 289467:1-12, **2015**. [10.1155/2015/289467]

195. Cui, L., Huxlin, K. R., Xu, L., MacRae, S., and Knox, W. H. High-resolution, noninvasive, two-photon fluorescence measurement of molecular concentrations in corneal tissue. *Investig. Ophthalmol. Vis. Sci.* **52 (5)**, 2556–2564, **2011**. [10.1167/iovs.10-6620]

196. Gore, D. M., Margineanu, A., French, P., O'Brart, D., Dunsby, C., and Allan, B. D. Two-photon fluorescence microscopy of corneal riboflavin absorption. *Invest Ophthalmol Vis Sci* **55 (4)**, 2476–2481, **2014**. [10.1167/iovs.14-13975]

197. Seiler, T. G., Ehmke, T., Fischinger, I., Zapp, D., Stachs, O., Seiler, T., and Heisterkamp, A. Two-photon fluorescence microscopy for determination of the riboflavin concentration in the anterior corneal stroma when using the dresden protocol. *Investig. Ophthalmol. Vis. Sci.* **56 (11)**, 6740–6746, **2015**. [10.1167/iovs.15-17656]

198. Lombardo, G., Micali, N. L., Villari, V., Serrao, S., and Lombardo, M. All-optical method to assess stromal concentration of riboflavin in conventional and accelerated UV-A irradiation of the human cornea. *Investig. Ophthalmol. Vis. Sci.*

**57 (2)**, 476–483, **2016**. [10.1167/iovs.15-18651]

199. Wang, T. J., Lo, W., Hsueh, C. M., Hsieh, M. S., Dong, C. Y., and Hu, F. R. Ex vivo multiphoton analysis of rabbit corneal wound healing following conductive keratoplasty. *J Biomed Opt* **13 (3)**, 34019:1-9, **2008**. [10.1117/1.2943156]

200. Teng, S. W., Tan, H. Y., Sun, Y., Lin, S. J., Lo, W., Hsueh, C. M., Hsiao, C. H., Lin, W. C., Huang, S. C., and Dong, C. Y. Multiphoton fluorescence and second-harmonic-generation microscopy for imaging structural alterations in corneal scar tissue in penetrating full-thickness wound. *Arch Ophthalmol* **125 (7)**, 977–978, **2007**. [10.1001/archopht.125.7.977]

201. Farid, M., Morishige, N., Lam, L., Wahlert, A., Steinert, R. F., and Jester, J. V. Detection of Corneal Fibrosis by Imaging Second Harmonic–Generated Signals in Rabbit Corneas Treated with Mitomycin C after Excimer Laser Surface Ablation. *Investig. Opthalmology Vis. Sci.* **49 (10)**, 4377–4383, **2008**. [10.1167/iovs.08-1983]

202. Batista, A., Silva, S. F., Domingues, J. P., and Morgado, A. M. Fluorescence Lifetime based Corneal Metabolic Imaging. *Procedia Technol.* **17**, 281–288, **2014**. [10.1016/j.protcy.2014.10.238]

203. Steven, P., Hovakimyan, M., Guthoff, R. F., Hüttmann, G., and Stachs, O. Imaging corneal crosslinking by autofluorescence 2-photon microscopy, second harmonic generation, and fluorescence lifetime measurements. *J Cataract Refract Surg* **36 (12)**, 2150–2159, **2010**. [10.1016/j.jcrs.2010.06.068]

204. Gehlsen, U., Oetke, A., Szaszak, M., Koop, N., Paulsen, F., Gebert, A., Huettmann, G., and Steven, P. Two-photon fluorescence lifetime imaging monitors metabolic changes during wound healing of corneal epithelial cells in vitro. *Graefes Arch Clin Exp Ophthalmol* **250 (9)**, 1293–1302, **2012**. [10.1007/s00417-012-2051-3]

205. König, K., Uchugonova, A., Straub, M., Zhang, H., Licht, M., Afshar, M., Feili, D., and Seidel, H. Sub-100 nm material processing and imaging with a sub-15 femtosecond laser scanning microscope. *J. Laser Appl.* **24 (4)**, 042009:1-9, **2012**. [10.2351/1.4718858]

206. Adur, J. Quantitative changes in human epithelial cancers and osteogenesis

imperfecta disease detected using nonlinear multicontrast microscopy. *J. Biomed. Opt.* **17 (8)**, 081407:1-10, **2012**. [10.1117/1.JBO.17.8.081407]

207. Birngruber, E., Donner, R., and Langs, G. MatVTK - 3D Visualization for Matlab. in *Proceedings of the MICCAI 2009 Workshop on systems and architectures for CAI* 1–8, **2009**.

208. Elisabeth, P., Hilde, B., and Ilse, C. Eye bank issues: II. Preservation techniques: warm versus cold storage. *Int. Ophthalmol.* **28 (3)**, 155–163, **2008**. [10.1007/s10792-007-9086-1]

209. Yıldırım, Y., Olcucu, O., Gunaydin, Z. K., Ağca, A., Ozgurhan, E. B., Alagoz, C., Mutaf, C., and Demirok, A. Comparison of Accelerated Corneal Collagen Cross-linking Types for Treating Keratoconus. *Curr. Eye Res.* **42 (7)**, 971–975, **2017**. [10.1080/02713683.2017.1284241]

210. Batista, A., Breunig, H. G., Uchugonova, A., Morgado, A. M., and König, K. Two-Photon Spectral Fluorescence Lifetime and Second-Harmonic Generation Imaging of the Porcine Cornea with a 12 Femtosecond Laser Microscope. *J. Biomed. Opt.* **21 (3)**, 036002:1-11, **2016**. [10.1117/1.JBO.21.3.036002]

211. Batista, A., Breunig, H. G., König, A., Morgado, A. M., and König, K. Assessment of the metabolism and morphology of the porcine cornea, lens and retina by 2-photon imaging. *J. Biophotonics* **11 (7)**, e201700324:1-8, **2018**. [10.1002/jbio.201700324]

212. Batista, A., Breunig, H. G., König, A., Schindele, A., Hager, T., Seitz, B., Morgado, A. M., and König, K. Assessment of Human Corneas Prior to Transplantation Using High-Resolution Two-Photon Imaging. *Investig. Opthalmology Vis. Sci.* **59 (1)**, 176–184, **2018**. [10.1167/iovs.17-22002]

213. Khaled, M. L., Helwa, I., Drewry, M., Seremwe, M., Estes, A., and Liu, Y. Molecular and Histopathological Changes Associated with Keratoconus. *Biomed Res. Int.* **2017**, 7803029:1-16, **2017**. [10.1155/2017/7803029]

214. Feder, R. S., and Gan, T. J. Noninflammatory Ectatic Disorders. in *Cornea - Fundamentals, Diagnosis and Management (Volume 1)* (eds. Krachmer, J. H., Mannis, M. J. & Holland, E. J.) Mosby/Elsevier, 3rd Ed., Maryland Heights, Missouri,

USA, **2011**.

215. Tu, E. Y. Acanthamoeba and Other Parasitic Corneal Infections. in *Cornea - Fundamentals, Diagnosis and Management (Volume 1)* (eds. Krachmer, J. H., Mannis, M. J. & Holland, E. J.) Mosby/Elsevier, 3rd Ed., Maryland Heights, Missouri, USA, **2011**.

216. Clarke, D. W., and Niederkorn, J. Y. The pathophysiology of Acanthamoeba keratitis. *Trends Parasitol* **22 (4)**, 175–180, **2006**. [10.1016/j.pt.2006.02.004]

217. Clarke, B., Sinha, A., Parmar, D. N., and Sykakis, E. Advances in the Diagnosis and Treatment of Acanthamoeba Keratitis. *J. Ophthalmol.* **2012**, 484892:1-6, **2012**. [10.1155/2012/484892]

218. Torricelli, A. A. M., Santhanam, A., Wu, J., Singh, V., and Wilson, S. E. The corneal fibrosis response to epithelial–stromal injury. *Exp. Eye Res.* **142 (6)**, 110–118, **2016**. [10.1016/j.exer.2014.09.012]

219. Batista, A., Breunig, H. G., König, A., Schindele, A., Hager, T., Seitz, B., and König, K. High-resolution, label-free two-photon imaging of diseased human corneas. *J. Biomed. Opt.* **23 (03)**, 036002:1-8, **2018**. [10.1117/1.JBO.23.3.036002]

220. Khan, Y. A., Kashiwabuchi, R. T., Martins, S. A., Castro-Combs, J. M., Kalyani, S., Stanley, P., Flikier, D., and Behrens, A. Riboflavin and ultraviolet light a therapy as an adjuvant treatment for medically refractive Acanthamoeba keratitis: report of 3 cases. *Ophthalmology* **118 (2)**, 324–31, **2011**. [10.1016/j.ophtha.2010.06.041]

221. Spoerl, E., Huhle, M., and Seiler, T. Induction of cross-links in corneal tissue. *Exp Eye Res* **66 (1)**, 97–103, **1998**. [10.1006/exer.1997.0410]

222. Wollensak, G., Spoerl, E., and Seiler, T. Riboflavin/ultraviolet-a–induced collagen crosslinking for the treatment of keratoconus. *Am J Ophthalmol* **135 (5)**, 620–627, **2003**. [10.1016/s0002-9394(02)02220-1]

223. Schumacher, S., Oeftiger, L., and Mrochen, M. Equivalence of biomechanical changes induced by rapid and standard corneal cross-linking, using riboflavin and ultraviolet radiation. *Investig. Ophthalmol. Vis. Sci.* **52 (12)**, 9048–9052, **2011**.

[10.1167/iovs.11-7818]

224. Chow, V. W. S., Chan, T. C. Y., Yu, M., Wong, V. W. Y., and Jhanji, V. One-year outcomes of conventional and accelerated collagen crosslinking in progressive keratoconus. *Sci. Rep.* **5**, 14425:1-7, **2015**. [10.1038/srep14425]

225. Waszczykowska, A., and Jurowski, P. Two-Year Accelerated Corneal Cross-Linking Outcome in Patients with Progressive Keratoconus. *Biomed Res. Int.* **2015**, 325157:1-9, **2015**. [10.1155/2015/325157]

226. Raiskup-Wolf, F., Hoyer, A., Spoerl, E., and Pillunat, L. E. Collagen crosslinking with riboflavin and ultraviolet-A light in keratoconus: long-term results. *J Cataract Refract Surg* **34 (5)**, 796–801, **2008**. [10.1016/j.jcrs.2007.12.039]

227. Jankov Ii, M. R., Jovanovic, V., Delevic, S., and Coskunseven, E. Corneal collagen cross-linking outcomes: review. *Open Ophthalmol. J.* **5**, 19–20, **2011**. [10.2174/1874364101105010019]

228. Caporossi, A., Mazzotta, C., Baiocchi, S., Caporossi, T., Denaro, R., and Balestrazzi, A. Riboflavin-UVA-Induced Corneal Collagen Cross-linking in Pediatric Patients. *Cornea* **31 (3)**, 227–231, **2012**. [10.1097/ICO.0b013e31822159f6]

229. Koller, T., Mrochen, M., and Seiler, T. Complication and failure rates after corneal crosslinking. *J. Cataract Refract. Surg.* **35 (8)**, 1358–1362, **2009**. [10.1016/j.jcrs.2009.03.035]

230. Baenninger, P. B., Bachmann, L. M., Wienecke, L., Kaufmann, C., and Thiel, M. A. Effects and adverse events after CXL for keratoconus are independent of age: a 1-year follow-up study. *Eye* **28 (6)**, 691–695, **2014**. [10.1038/eye.2014.56]

231. Antoun, J., Slim, E., el Hachem, R., Chelala, E., Jabbour, E., Cherfan, G., and Jarade, E. F. Rate of Corneal Collagen Crosslinking Redo in Private Practice: Risk Factors and Safety. *J. Ophthalmol.* **2015**, 690961:1-8, **2015**. [10.1155/2015/690961]

232. Batey, D. W., and Eckhert, C. D. Analysis of flavins in ocular tissues of the rabbit. *Invest Ophthalmol Vis Sci* **32 (7)**, 1981–1985, **1991**.

233. Masters, B. R., Ghosh, A. K., Wilson, J., and Matschinsky, F. M. Pyridine nucleotides

and phosphorylation potential of rabbit corneal epithelium and endothelium. *Invest Ophthalmol Vis Sci* **30 (5)**, 861–868, **1989**.

234. Lee, S. E., Mehra, R., Fujita, M., Roh, D. S., Long, C., Lee, W., Funderburgh, J. L., Ayares, D. L., Cooper, D. K. C., and Hara, H. Characterization of Porcine Corneal Endothelium for Xenotransplantation. *Semin. Ophthalmol.* **29 (3)**, 127–135, **2014**. [10.3109/08820538.2013.787104]

235. Walsh, A. J., Cook, R. S., Sanders, M. E., Aurisicchio, L., Ciliberto, G., Arteaga, C. L., and Skala, M. C. Quantitative Optical Imaging of Primary Tumor Organoid Metabolism Predicts Drug Response in Breast Cancer. *Cancer Res.* **74 (18)**, 5184–5194, **2014**. [10.1158/0008-5472.CAN-14-0663]

236. Walsh, A. J., and Skala, M. C. Optical metabolic imaging quantifies heterogeneous cell populations. *Biomed. Opt. Express* **6 (2)**, 559–573, **2015**. [10.1364/BOE.6.000559]

237. Alam, S. R., Wallrabe, H., Svindrych, Z., Chaudhary, A. K., Christopher, K. G., Chandra, D., and Periasamy, A. Investigation of Mitochondrial Metabolic Response to Doxorubicin in Prostate Cancer Cells: An NADH, FAD and Tryptophan FLIM Assay. *Sci. Rep.* **7 (1)**, 10451, **2017**. [10.1038/s41598-017-10856-3]

238. König, K., Uchugonova, A., and Gorjup, E. Multiphoton fluorescence lifetime imaging of 3D-stem cell spheroids during differentiation. *Microsc. Res. Tech.* **74 (1)**, 9–17, **2011**. [10.1002/jemt.20866]

239. Stringari, C., Edwards, R. A., Pate, K. T., Waterman, M. L., Donovan, P. J., and Gratton, E. Metabolic trajectory of cellular differentiation in small intestine by Phasor Fluorescence Lifetime Microscopy of NADH. *Sci. Rep.* **2 (568)**, 1–9, **2012**. [10.1038/srep00568]

240. McGhee, C., Crawford, A., and Patel, D. A brief history of corneal transplantation: From ancient to modern. *Oman J. Ophthalmol.* **6 (4)**, 12, **2013**. [10.4103/0974-620X.122289]

241. Hori, J. Mechanisms of immune privilege in the anterior segment of the eye: what we learn from corneal transplantation. *J. Ocul. Biol. Dis. Infor.* **1 (2–4)**, 94–100,

**2008**. [10.1007/s12177-008-9010-6]

242. Niederkorn, J. Y. Corneal Transplantation and Immune Privilege. *Int. Rev. Immunol.* **32 (1)**, 57–67, **2013**. [10.3109/08830185.2012.737877]

243. Parekh, M., Ferrari, S., Ruzza, A., Pugliese, M., Ponzin, D., and Salvalaio, G. A portable device for measuring donor corneal transparency in eye banks. *Cell Tissue Bank.* **15 (1)**, 7–13, **2014**. [10.1007/s10561-013-9372-2]

244. Manickavasagam, A., Hirvonen, L. M., Melita, L. N., Chong, E. Z., Cook, R. J., Bozec, L., and Festy, F. Multimodal optical characterisation of collagen photodegradation by femtosecond infrared laser ablation. *Analyst* **139 (23)**, 6135–6143, **2014**. [10.1039/C4AN01523A]

245. Lutz, V., Sattler, M., Gallinat, S., Wenck, H., Poertner, R., and Fischer, F. Impact of collagen crosslinking on the second harmonic generation signal and the fluorescence lifetime of collagen autofluorescence. *Ski. Res. Technol.* **18 (2)**, 168–179, **2012**. [10.1111/j.1600-0846.2011.00549.x]

246. Lu, L., Reinach, P. S., and Kao, W. W. Corneal epithelial wound healing. *Exp. Biol. Med. (Maywood).* **226 (7)**, 653–664, **2001**.

247. Mazzotta, C., Traversi, C., Caragiuli, S., and Rechichi, M. Pulsed vs continuous light accelerated corneal collagen crosslinking: in vivo qualitative investigation by confocal microscopy and corneal OCT. *Eye* **28 (10)**, 1179–1183, **2014**. [10.1038/eye.2014.163]

248. Zare, M., Mazloumi, M., Farajipour, H., Hoseini, B., Fallah, M., Mahrjerdi, H., Abtahi, M.-A., and Abtahi, S. Effects of corneal collagen crosslinking on confocal microscopic findings and tear indices in patients with progressive keratoconus. *Int. J. Prev. Med.* **7 (1)**, 132–142, **2016**. [10.4103/2008-7802.196527]

249. Ozgurhan, E. B., Sezgin Akcay, B. I., Yildirim, Y., Karatas, G., Kurt, T., and Demirok, A. Evaluation of Corneal Stromal Demarcation Line after Two Different Protocols of Accelerated Corneal Collagen Cross-Linking Procedures Using Anterior Segment Optical Coherence Tomography and Confocal Microscopy. *J. Ophthalmol.* **2014**, 981893:1-5, **2014**. [10.1155/2014/981893]

250. Malta, J. B. N., Renesto, A. C., Moscovici, B. K., Soong, H. K., and Campos, M. Stromal Demarcation Line Induced by Corneal Cross-linking in Eyes With Keratoconus and Nonkeratoconic Asymmetric Topography. *Cornea* **34 (2)**, 199–203, **2015**. [10.1097/ICO.0000000000000305]

251. Scarcelli, G., Pineda, R., and Yun, S. H. Brillouin optical microscopy for corneal biomechanics. *Investig. Ophthalmol. Vis. Sci.* **53 (1)**, 185–190, **2012**. [10.1167/iovs.11-8281]

252. Scarcelli, G., Kling, S., Quijano, E., Pineda, R., Marcos, S., and Yun, S. H. Brillouin microscopy of collagen crosslinking: Noncontact depth-dependent analysis of corneal elastic modulus. *Investig. Ophthalmol. Vis. Sci.* **54 (2)**, 1418–1425, **2013**. [10.1167/iovs.12-11387]

253. Kwok, S. J. J., Kuznetsov, I. A., Kim, M., Choi, M., Scarcelli, G., and Yun, S. H. Selective two-photon collagen crosslinking in situ measured by Brillouin microscopy. *Optica* **3 (5)**, 469–472, **2016**. [10.1364/OPTICA.3.000469]

254. Webb, J. N., Su, J. P., and Scarcelli, G. Mechanical outcome of accelerated corneal crosslinking evaluated by Brillouin microscopy. *J. Cataract Refract. Surg.* **43 (11)**, 1458–1463, **2017**. [10.1016/j.jcrs.2017.07.037]

255. Aminifard, M.-N., Khallaghi, H., Mohammadi, M., and Jafarzadeh, R. Comparison of corneal keratocytes before and after corneal collagen cross-linking in keratoconus patients. *Int. Ophthalmol.* **35 (6)**, 785–792, **2015**. [10.1007/s10792-015-0041-2]